学位論文

A study on radiative transfer effects in 3D cloudy atmospheres using Monte Carlo numerical simulation

（モンテカルロ数値シミュレーションを用いた 3 次元雲場の放射伝達効果に関する研究）

平成 28 年 12 月博士（理学）申請

東京大学大学院理学系研究科

地球惑星科学専攻

大方　めぐみ

Abstract

This study evaluates 3D cloud effects on the radiation budget with a combined use of active sensor CPR/CLOUDSAT and imager MODIS/AQUA data on the A-train. An algorithm is devised for constructing 3D cloud fields based on satellite-observed cloud information. The 3D cloud fields thus constructed are used to calculate the broadband solar and thermal radiative fluxes with a 3D Radiative Transfer (RT) code developed by the author. I develop a 3D Monte-Carlo RT code, called *MCstar*, as a Monte-Carlo version of the *STAR* series (*System for Transfer of Atmospheric Radiation*) developed by OpenCLASTR (Nakajima and Tanaka. 1986, 1988; Sekiguchi and Nakajima 2008). The *MCstar* code has a capability of calculating spectral and broadband radiances and radiative fluxes in SW and LW spectral bands with forward and backward ray tracing systems and the optical properties of atmospheric constituents consistent with those of other Star codes. The aim of this study is to investigate the effects of "observed" real cloud morphology on solar radiative transfer in cloudy atmosphere. For this purpose, 3D cloud fields are constructed with the new satellite-based method, to which full 3D-RT simulations are applied.

The simulated 3D radiation fields are then used to examine and quantify errors of existing typical plane parallel approximations, i.e. Plane-Parallel Approximation (PPA), Independent Pixel Approximation (IPA) and Tilted Independent Pixel Approximation (TIPA). Such 3D-RT simulations also serve to address another objective of this study, i.e. to devise an accurate approximation and to characterize the "observed" specific 3D-RT effects by the cloud morphology based on knowledge of idealized 3D-RT effects. I introduce a modified approach based on an optimum value of diffusivity factor to better approximate the radiative fluxes for arbitrary Solar Zenith Angle (SZA) determined from the results of 3D radiative transfer simulations to redeem the overcorrections of these existing approximations for large SZAs. This new approach, called Slant Independent Pixel Approximation (SIPA), is found to be better than other approximations when SZA is large for some cloud cases.

Based on the SZA dependence of the errors of these approximations relative to 3D-RT computations, "satellite-observed" real cloud cases are found to fall into one of three types of different simple morphologies, i.e. isolated cloud type, upper

cloud-roughened type and lower cloud-roughened type. The characterization for these typical 3D-CRE of "observed" cloud fields can be proved by characteristics of the effective cloud fraction (CFe) profile in altitude and RGB composite map derived from MODIS 3 channels of these cloud fields. I define an effective cloud fraction (CFe) derived from the regional average cloud optical thickness and the standard deviation. CFe is large for homogeneous cloud filed, whereas vice versa for inhomogeneous. The RGB map described by 0.6, 2.1 and 11μm of MODIS imager reflects cloud top morphology information. It is confirmed that the CFe profiles in altitude and RGB composite maps are consistency of classification of above three types of cloud morphology with full 3D-simulations. Such a classification offers a novel approach of cloud characterization based on quantitative indices related with and without the 3D cloud radiative effects.

Acknowledgments

Foremost I would like to express my sincere gratitude to my advisor Prof. Teruyuki Nakajima for the continuous support of my Ph.D. study and related research, for his patience, motivation, and immense knowledge. I appreciate all his contributions of time, ideas, and funding to make my PhD. Experience productive and stimulating. His guidance helped me in all the time of research and writing of this thesis. I could not have imagined having a better adviser and mentor for my Ph.D. study. I am profoundly grateful for providing me many opportunities to join Radiation group and related projects. I am also thankful for the excellent example he has provided as a successful man atmospheric physicist and professor.

I would like to express my gratitude to Prof. Kentaroh Suzuki to take over as an advisor for support of my PhD. study. I am grateful for his contributions of funding to make my PhD.

Besides my advisors, I would like to appreciate the rest of my thesis committee: Prof. Makoto Koike, Prof. Yukari Takayabu, Prof. Ryoichi Imasu, Prof. Akira Oka at University of Tokyo, and Prof. Hironobu Iwabuchi at Tohoku University, for their insightful comments and encouragement, but also for the hard question which incented me to widen my research from various perspectives.

My sincere also appreciate to Dr. Toshiro Inoue at University of Tokyo, Prof. Takashi Nakajima at Tokai University, and Hajime Okamoto at Kyusyu University for providing data, these acknowledges and professional advises.

The members of Terry's laboratory and Radiation group regardless of whether it is in or out of the country have contributed immensely to my personal and professional time. Without they precious support it would not be possible to conduct this research. I thank my fellow labmates of Center of Climate System of Research (CCSR) at Atmosphere and Ocean Research Institute (AORI), University of Tokyo in for the stimulating discussions. I appreciate to my friends in the following institution. They have encouraged to make me confident when I had a hard time in my research. They mentally have supported me warmly.

Last but not the least, I would like to thank my family: my parents and to my brother and my grandmother for supporting me spiritually throughout writing this thesis and my life in general.

Megumi Okata, February 2017

Contents

Chapter 1

Introduction

The solar and thermal infrared radiative transfer (RT) exerts a significant effect on the cloud formation and hence on the earth's climate system. Fig 1.1. shows global mean energy budget under the present-day climate condition. Numbers state magnitudes of the individual energy fluxes in Wm^{-2}, adjusted within their uncertainty ranges to close the energy budget (Wild et al., 2015). Radiative heating and cooling of each part of the atmosphere-surface system controls the energy redistribution of the cloud-laden atmospheric system that affects convective process and cloud formation itself. Conversely, the radiation process depends in a complex way on the amount, shapes and microphysical properties of the cloud field. (McKee and Cox, 1974; Aida, 1977; Davies, 1978; Kobayashi, 1989). This strong interaction between cloud and radiation makes it difficult to simulate the cloud system and its climatic effects in climate models. The IPCC AR-5 assessment report concludes that the simulation of the liquid water content and cloud radiative forcing (CRF) in the climate model still shows a large model dependence. Thus, cloud radiative effects (CRE) are considered as one of the main causes of the inter-model spread of the climate sensitivity.

One of these uncertainties includes the CRE caused by three-dimensional (3D) structures of clouds, which are difficult to represent in current climate models particularly for highly inhomogeneous cloud fields. Over the past three decades there has been a series of diagnostic studies aimed at demonstration of errors associated with neglect of 3D-RT within cloud in weather and climate models. (e.g. Marshak and Davis, 2005).

Generally, these studies used cloud field based on idealize models, passive (2D) satellite data, and air craft data. The simplest plane parallel approximation (PPA) includes errors reaching typically 20% in the thermal radiative flux, and 100% or more in the shortwave flux. These 3D-CRE also depend on the wavelength (e.g. Marshak and Davis, 2005). Motivated by these difficulties, a lot of studies have been devoted to

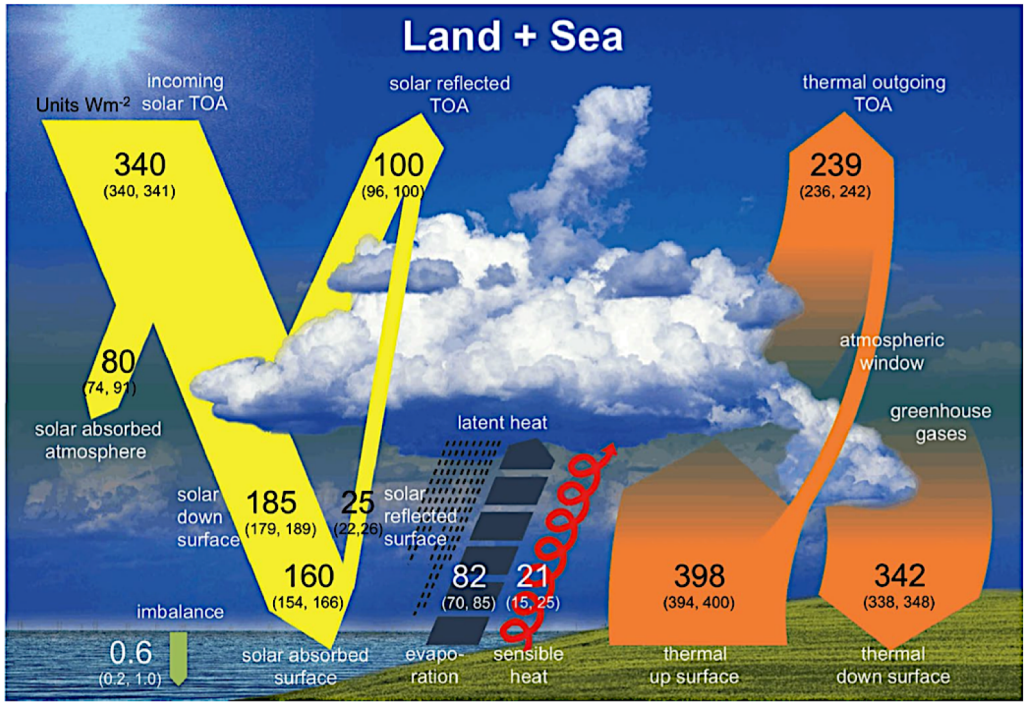

Figure 1.1. Global mean energy budget under the present-day climate condition. Numbers state magnitudes of the individual energy fluxes in Wm^{-2}, adjusted within their uncertainty ranges to close the energy budget. Numbers in parentheses attached to the energy fluxes cover the range of values in line of observational constraints. (IPCC-AR5, Wild et al., 2015)

quantification of the 3D-CRE of the cloud system. This includes development of various numerical RT computation methods for 3D cloudy atmospheres, such as Monte-Carlo method (e.g., Marshak and Davis, 2005), harmonic function expansion method (Stephens et al, 1991), discrete ordinate method (e.g., Stamnes et al, 1988), Spherical Harmonic Discrete Ordinate Method (SHDOM) (Evans, 1998), wavelet decomposition method (Ishida, 2014) and others.

To improve climate predictions and weather forecasts I need to understand the delicate linkage between clouds and radiation. A trust tool to further our understanding in atmospheric science is the class of models known as large-eddy simulations (LESs). These models have capability of resolving the most energetic eddies and were successfully used to study boundary layer structure as well as shallow and deep convective systems. Radiative heating and cooling drives convective motion and influence cloud droplet growth and microphysics (Marquis and Harrington, 2005). One-dimensional radiative transfer, i.e. Plane Parallel Approximation (PPA), by definition to ignore effects such as cloud side illumination, displaced cloud shadows, and horizontal energy transport in general. Jacob and Mayer. (2016) reported the performance and applicability of fast RT scheme, i.e. the Ten-Stream RT solver, in large-eddy simulations. There is obvious evidence that the neglect of theses 3D-RT effects led to big errors in heating rate by their reports. Thus, it is significant to simulate for these cloud growth and microphysical process in keeping with 3D-RT simulation. It is necessary to derive a fast scheme, i.e. above Ten-Stream RT solver, to solve 3D-RT in LES domain because 3D-RT full stimulations are very expensive simultaneously.

Large computational demands, required by these rigorous solutions to the 3D-RT equation (RTE), have also motivated researchers to devise several approximations to the 3D-CRE. Among those are the Independent Pixel/Column Approximation (IPA/ICA) (Stephens et al., 1991; Cahalan et al., 1994), Tilted Independent Pixel Approximation (TIPA) (Varnai and Davies,1999), parameterized Nonlocal Independent Column Approximation (paNICA) (Wissmeier et al., 2013) and Neighboring Column Approximation (NCA) (Klinger and Mayer, 2016) based on Plane Parallel Approximation (PPA). The performance of these approximations against the full 3D-RT computation has been found to depend on horizontal and vertical structures of the cloud system as reported by many previous studies (Wielicki and Welch, 1985; Barker and Davies, 1992; Cahalan et al., 1994; Varnai and Marshak, 2002; Marshak et al., 2006;

L'Ecuyer et al., 2008; Barker et al., 2011; 2012; Ham et al., 2014). Many of previous studies, however, are limited to investigations for solar radiation effects based on theoretical clouds constructed by ideal or numerical cloud models due to the lack of observation data for the 3D cloud field on the global scale. It is, therefore, critical to have observational information of 3D cloud structure as inputs to RT simulations to quantify the 3D-CRE and to seek improved approximations.

Notable in this regard is the emergence of the first space-borne cloud profiling radar (CPR) at 94GHz frequency on board the NASA CloudSat satellite launched in 2006 (Fig 1.2). This sensor provides us with unprecedented information of cloud inner structure in the form of the radar echo profile as a function of height at the footprint of the satellite track. There is also a plan of the ESA-JAXA EarthCARE satellite mission that will simultaneously carry a Doppler CPR and a high spectral resolution ultra-violet lidar (ATLID HSRL) (Illingworth et al., 2015), which will continue and enhance the measurement capability of vertical cloud structure provided by CloudSat. The emergence and upcoming continuation of this new capability of cloud measurement is our underlying motivation for this study that intends to investigate and quantify the CRE of 3D cloudy atmosphere based on observation data.

The vertical profile information from CloudSat, although limited to nadir, can be employed to construct 3D cloud fields by its extension to off-nadir regions based on passive-sensor-derived information collocated with the radar profile. Barker et al. (2011, 2012) developed such a method for constructing 3D cloud fields with a combined use of CloudSat/CPR, Aqua/MODIS imager and CALIPSO/CALIOP and employed the cloud fields for their Monte-Carlo RT simulations for SW radiative flux. This approach enables them to calculate the 3D-CRE based on “observed” 3D information of cloud fields. Although their approach is a first attempt to exploit the A-Train information for 3D-RT simulations, their method is based on MODIS-measured radiances, not cloud physical properties, to extrapolate the radar profile into off-nadir. It is however important to attempt more straightforward method to use physical properties of clouds retrieved from radiances, rather than radiances themselves, to extrapolate the cloud profile outside the satellite track. The present study adopts this strategy for constructing 3D cloud field and devises a new 3D cloud field construction method. There is, moreover, no assessment for LW 3D-CRE in “observed” cloud fields.

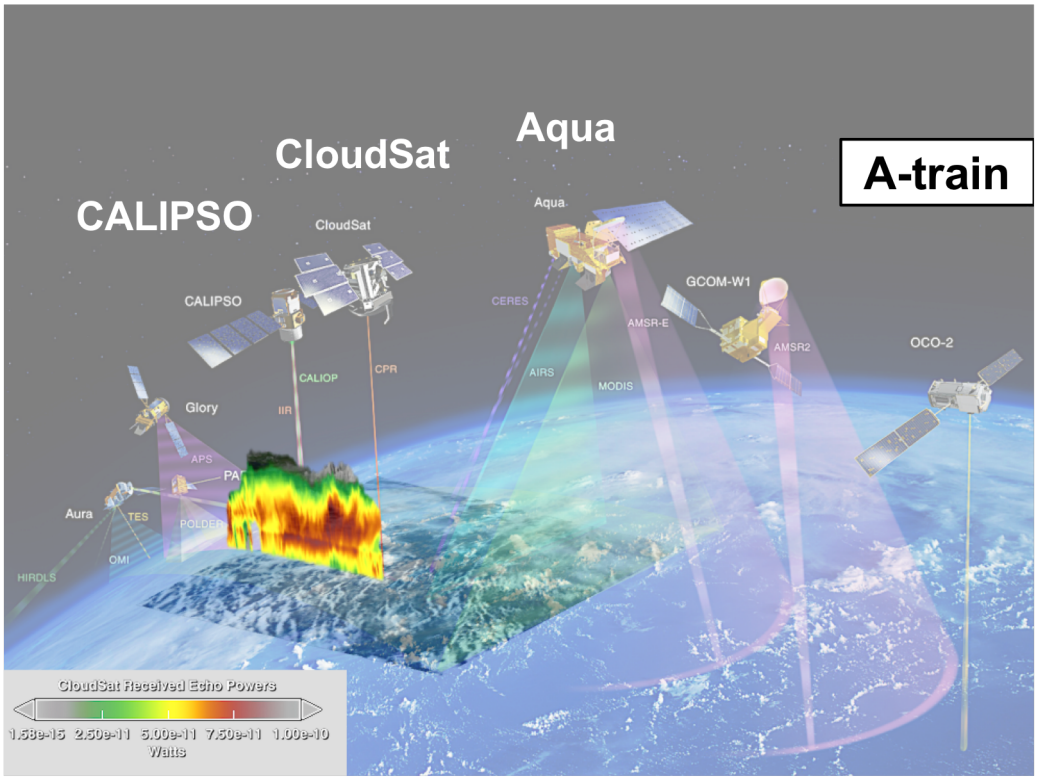

Figure 1.2. CloudSat detected attributes of clouds on slices through the atmosphere. Here both are shown over an image of MODIS reflectance which is mapped onto the terrain. (NASA: https://svs.gsfc.nasa.gov/cgi-bin/details.cgi?aid=3436)

The aim of this study is to investigate the effect of cloud morphology on solar and thermal infrared radiative transfer in cloudy atmosphere through assessment of the error characteristics of plane-parallel approximations relative to full 3D-RT simulations. The study intends to offer a satellite observation-based insight into the cloud morphology effect based on satellite-retrieved cloud fields built by the new 3D cloud field construction method. Another purpose of this study is to introduce an accurate approximation to 3D radiative fluxes based on the knowledge obtained from the analysis mentioned above.

The new 3D cloud field construction method using cloud microphysical data are described in Section 3. The 3D cloudy atmosphere fields thus constructed are then employed as inputs to 3D radiative transfer simulations with a newly developed Monte-Carlo type 3D-RT code as described in Section 2. Before analyzing the real observed data CRE, Section 4 details the assessment of 3D cloud radiative effects obtained from Monte-Carlo simulations and compares the results with those obtained by plane parallel approximations for some characteristic idealized cloud cases. I also describe a new approximation, called Slant-path Independent Pixel Approximation (SIPA), that assumes an "effective" slant path by introducing a concept of Virtual Solar Zenith Angle (VSZA) in Section 4. I then discuss how the optimum VSZA determined by 3D Monte-Carlo simulations tends to vary from case to case depending on spatial structure of real clouds. In this study, the analysis is applied to 15 cases of water cloud field obtained by CloudSat and MODIS over the area off California. Section 5 details the analyses of 3D cloud radiative effects obtained from Monte-Carlo simulations and some of the existing plane parallel approximations. It is then discussed how the key errors could be mitigated by a new approximation proposed in this study. In addition, I provide a classification of cloud morphology that is effective to solar radiative transfer based on 3D-RT simulations and existing approximations in Section 5. The conclusion is given in Section 6.

Chapter 2

Development of a 3D Monte-Carlo Radiative Transfer Code

In this section, for three-dimensional (3D) radiative transfer solution, I describe a 3D Radiative Transfer (RT) code developed using a Monte Carlo method, which is a popular calculation method for 3D atmospheres and has been employed to simulate for 3D-RT in various applications. This method is statistical and flexible enough to be applied to a wide range of problems with scattering volumes of various shapes and can cover one-dimensional (1D) to 3D applications (Marshak and Davis, 2005). It treats a large number of photons traced from the incident radiation source to receivers which are located at given altitudes and aimed in specific viewing direction. The required number of photons is determined by the statistical radiative significance of photons arriving at the receivers. For optically thick atmospheres, the number of incident photons may be quite large in order to warrant a statistically significant number of photons arriving at the receivers. As photons propagate through the atmosphere, each single interaction event is calculated between photons and atmospheric constituents, i.e., air molecules, aerosol particles, cloud droplets, ice crystals, or precipitation particles, by using their phase function and optical cross sections for scattering and absorption. The backward Monte Carlo method is a method to trace photons propagating in the reverse direction from receiver to source.

I develop a 3D Monte-Carlo RT code, called *MCstar*, as a Monte-Carlo version of the *STAR* series (*System for Transfer of Atmospheric Radiation*) developed by OpenCLASTR (Nakajima and Tanaka. 1986, 1988; Sekiguchi and Nakajima 2008). OpenCLASTR contains *Rstar, Pstar*, and *MSTRN* for RT computations for scalar 1D, polarization 1D, and rapid code for dynamic computation, respectively. Light absorption of atmospheric gases is calculated by non-linear *k*-distribution parameters of Sekiguchi and Nakajima (2008). The *MCstar* code has a capability of calculating narrowband and broadband radiances and radiative fluxes in SW and LW spectral bands

with forward and backward ray tracing systems and the optical properties of atmospheric constituents consistent with those of other Star codes. The code also adopts the *DM*-method for efficient calculation of radiative flux and the *TMS*-method for accurate and efficient radiance calculation (Nakajima and Tanaka. 1988).

2. 1 Radiative Transfer Theory

In this section, I present the photon transport theory and RT calculation by the Monte Carlo method, and describe the basic structure of the *MCstar* system.

The 3D Radiative Transfer Equation (RTE) for radiance (L) in the steady state can be described as follow,

$$\Omega \cdot \nabla L(\mathbf{r},\Omega) = -e(\mathbf{r})L(\mathbf{r},\Omega) + s(\mathbf{r})\int_{4\pi} P(\mathbf{r},\Omega,\Omega')L(\mathbf{r},\Omega')d\Omega' + a(\mathbf{r})B(\mathbf{r}), \qquad (2.1a)$$

$$e = a + e. \qquad (2.1b)$$

The first term of the right hand side (rhs) of Eq. (2.1a) represents the amount of extinction of radiance along the target photon path; the second term represents the amount of radiance scattered from direction Ω' to direction Ω as expressed by normal direction vectors; the third term represents thermal emission at the point **r** as expressed by the Planck function B. Variables e, s and a are extinction, scattering, and absorption coefficients per unit volume at the point **r**, respectively; P is the scattering phase function as defined by the ratio of the amount of the incident radiation from direction Ω scattered into direction Ω'. I hereafter call the first term the extinction term, the second term the scattering source term, and the third term the thermal emission source term. The second and third terms are referred to as the radiation source terms. For the RTE Eq. (2.1a) there is a formal solution as follows,

$$L(\mathbf{r},\Omega) = L(\mathbf{r}_0,\Omega)\exp(-\tau(\mathbf{r},\mathbf{r}_0)) + \int_{\mathbf{r}_0}^{\mathbf{r}} J(\mathbf{r}',\Omega)\exp(-\tau(\mathbf{r}',\mathbf{r}_0))dr', \qquad (2.2)$$

where J is the radiative source function defined as follows,

$$J(\mathbf{r},\Omega) = s(\mathbf{r})\int_{4\pi} P(\mathbf{r},\Omega,\Omega')L(\mathbf{r},\Omega')d\Omega' + a(\mathbf{r})B(\mathbf{r}), \tag{2.3}$$

$$\tau(\mathbf{r},\mathbf{r}_0) = \exp\left(-\int_{\mathbf{r}_0}^{\mathbf{r}} e(\mathbf{r}')dr'\right), \tag{2.4}$$

The variable τ is the optical path length or the optical thickness along the photon path from $\mathbf{r}_0$ to $\mathbf{r}$ in Eq. (2.4). I show the image of RT system in cloudy atmospheres in Fig 2.1.

The rhs of Eq. (2.3) contains a set of radiances $\{L(\mathbf{r},\Omega'), \Omega' \in 4\pi\}$ from various directions, so that the equation system becomes a differential-integral equation for which various solution methods have been proposed. For example, there are harmonic function expansion method (Stephens et al, 1991), discrete ordinate method (e.g., Stamnes et al, 1988), Spherical Harmonic Discrete Ordinate Method (SHDOM) (Evans, 1998), wavelet decomposition method (Ishida, 2014) and others.

On the other, the Monte Carlo method, of which basic algorithm is general and flexible yet simple, can be applied to the scattering volume of various shapes. I thus adopt the Monte Carlo method in our study. Equation (2.2) can be rewritten in an integral form by the collision density *K* as follows (Marshak et al., 1980),

$$f(x) = \int_x K(x,x')f(x')dx' + \psi(x), \tag{2.5}$$

where $x = (\mathbf{r}, \Omega)$. $K(x, x')$ is called the transport kernel as expressed from Eq. (2.2) as follows to define the state transition event from x' state to x,

$$K(x,x') = \{-e(x)\delta(\Omega-\Omega') + s(x)P(x,\Omega,\Omega')\}\exp[-\tau(x,x')]. \tag{2.6}$$

This formula can be reduced to a Neumann series or successive scattering order series as in the following form by substituting sequentially the $f(x)$ into the rhs of Eq. (2.5),

$$\begin{aligned} f(x) &= \sum_{n=0}^{\infty}\int^{x} K(x,x')f_n(x')dx' + \Psi(x) \\ f_{n+1}(x) &= \int^{x} K(x,x')f_n(x')dx' \\ f_0(x) &= f_{0S}(x) + \Psi(x) \end{aligned}, \tag{2.7}$$

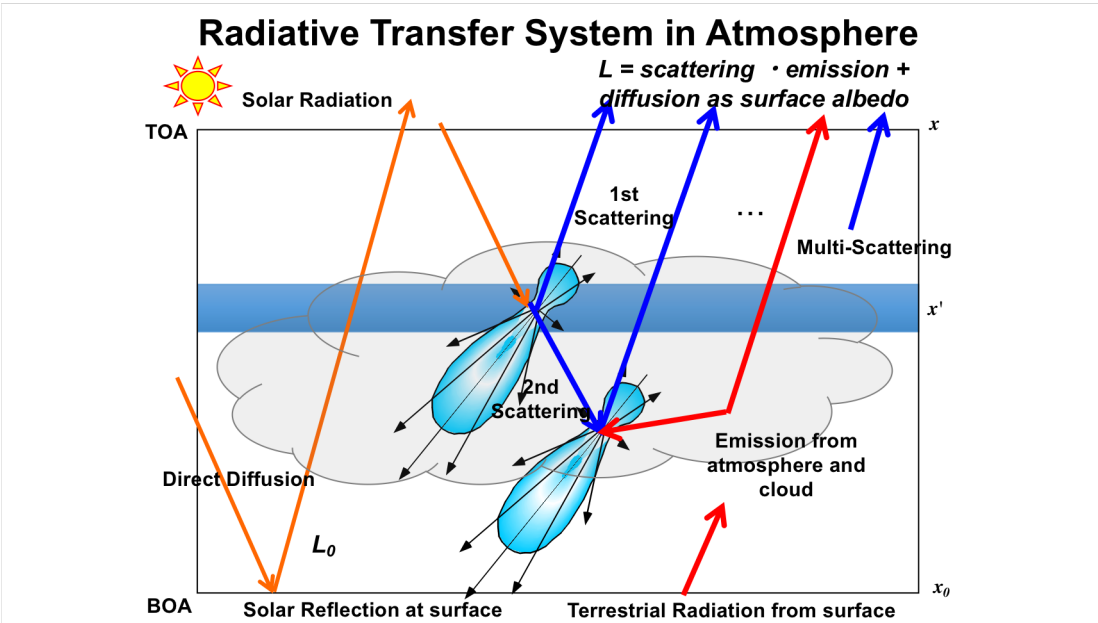

Figure 2.1. Illustration of upward radiance at TOA passing through the atmosphere of the Earth for both radiation originating from the sun i.e., shortwave-radiation (SW) and radiation originating from the Earth i.e., longwave radiation (LW). The red arrows represent radiances from the source, while the blue arrows represent scattered radiances.

where f_n is the solution for the n-th scattering order and f_{0S} is the direct solar radiation solution. The recursive formula of Eq. (2.7) for the n-th order scattering component of the radiance can be reduced to the following multi-dimensional integration formula,

$$f_{n+1}(x) = \int^{x} dx_n \int^{x_n} dx_{n-1} \ldots \int^{x_1} dx_0 K(x, x_n) K(x_n, x_{n-1}) \ldots K(x_1, x_0) f_0(x_0) . \qquad (2.8)$$

This integral can be evaluated by the Monte Carlo integration, which is known to be efficient than other numerical integration schemes when the number of dimension (n+1) becomes large. So, I obtain an accurate estimate of (2.8) using a large number of photons that are scattered at randomly selected locations at $\{x_{0,i}, x_{1,i}, \ldots, x_{n,i} | i = 1, N\}$ as,

$$< f(x) > = \frac{1}{N} \sum_{i=1}^{N} \sum_{n=0}^{\infty} K(x, x_{n,i}) K(x_{n,i}, x_{n-1,i}) \ldots K(x_{1,i}, x_{0,i}) f_0(x_{0,i}) . \qquad (2.9)$$

According to the central limit theorem, the sum of N uniform random numbers of a standard deviation σ follows a normal probability distribution with a standard deviation of $\sigma / \sqrt{N}$. In this way, therefore, the RT calculation can be realized by the Monte Carlo integration. This method is called the Monte Carlo method of RTE solution. Here note that the one model photon is a quantity defined as the sampling unit when performing the Monte Carlo integration, and does not coincide with one photon as a quantum unit in the quantum theory of light.

2.2 Model description of *MCstar*

In this study, I develop both the forward and the backward Monte Carlo radiative transfer codes to calculate radiance, radiative flux, and heating rate to investigate the 3D-CRE in the cloud-laden atmosphere. The response of SW radiation on the real 3D cloud structure is very complex according to the sensitive interaction between light and cloud particles, therefore it requires large validation effort of global climate model evaluations which mostly adopt a plane parallel approximation. For LW radiation, the RT process is affected by the spatial distribution of water vapor including inside clouds,

and emission sources that exist in all parts of the atmosphere and earth's surface with complex absorption spectra. The atmospheric window spectral region, i.e. 8-12μm, is especially important to estimate the CRE on the 3D broken cloudy atmosphere because scattering and absorption/emission effects of clouds are both significant and cannot be ignored. For calculation, I distribute 3D broken clouds in the model domain as the Earth' atmosphere and surface system. Parameters to model the optical properties of the atmospheric air mass are volume extinction coefficient and scattering coefficient and its angular cross section of atmospheric constituents, i.e. molecules, cloud droplet, ice crystal, and aerosol particles. I also consider the surface albedo as the parameter for surface reflection and absorption/emission. Model photons are input to the model domain and their tracks are traced. In the Earth's atmosphere, radiation sources are the sun and atmospheric constituents (molecules, cloud droplet, ice crystal, aerosol particles) to emit the thermal infrared radiation. The incident solar radiation is given by the extraterrestrial irradiance of the sun, while the thermal emission is defined by emissivity and temperature of the air mass. The photon track is ended when the model photon could be absorbed by an atmospheric constituent or by the surface, or reached the top of atmosphere (TOA) or detectors.

2.2.1 Monte Carlo radiative transfer algorithm for solar radiative flux and radiance

In the present model, I fill the model domain by the volume extinction coefficient e (m^{-1}), scattering coefficient s (m^{-1}), and normalized angular cross section, called phase function $P(\Theta)$ as function of the scattering angle Θ, for each atmospheric constituent. The single scattering albedo (SSA) ω is defined as,

$$\omega = \frac{s}{e}, \tag{2.2.1}$$

to quantify the co-absorptivity of the constituent. These optical parameters for aerosols and clouds are calculated by giving mode radius and standard deviation of the particle

size distribution, which is assumed as a log-normal distribution, complex refractive index and wavelength. Optical cross sections for molecules are calculated from one of the atmospheric models for vertical profiles of temperature, humidity and other trace gas concentration built in the *Rstar*, though any arbitrary profiles can be given by data files of *Rstar* (as explained later Section 2.3.2).

(1) Incidence of the model photon

I input a model photon from a given radiation source, and start ray tracing in the model domain. Solar insolation is defined by the horizontal position to be determined by uniform random numbers, i.e. R_1 and R_2, as

$$\begin{aligned} x = (x_N - x_0)R_1, \quad & y=(y_N - y_0)R_2 \\ R_1 \in [0,1), \quad & R_2 \in [0,1) \end{aligned} . \tag{2.2.2}$$

where (x_0, y_0) and (x_N, y_N) are corner coordinates of the model domain as depicted in the left panel of Fig 2.2. I discretize the model domain into NxN boxes at x- and y-coordinates, $(x_0, x_1, ..., x_N)$ and $(y_0, y_1, ..., y_N)$. Each box is approximated by a homogeneous atmosphere. The right panel of Fig 2.2 shows the incident photon distribution at TOA as sunlight illuminating an area (100km × 100km) approximated by the number of photons (NP) as 5×10^5.

(2) Decision of the interaction event

I assume a photon has an interaction event, i.e., scattering or absorption, after traveling a certain length from the present position. The probability that the model photon encounters an interaction event of extinction (scattering or absorption), for example, is given by the Lambert-Beer's law as,

$$T = \exp(-\tau), \tag{2.2.3}$$

where τ is called the extinction optical thickness or the optical path length, and given by a path integral of the volume extinction coefficient along photon track from the present point $\mathbf{r}_1$ to the destination point $\mathbf{r}_2$,

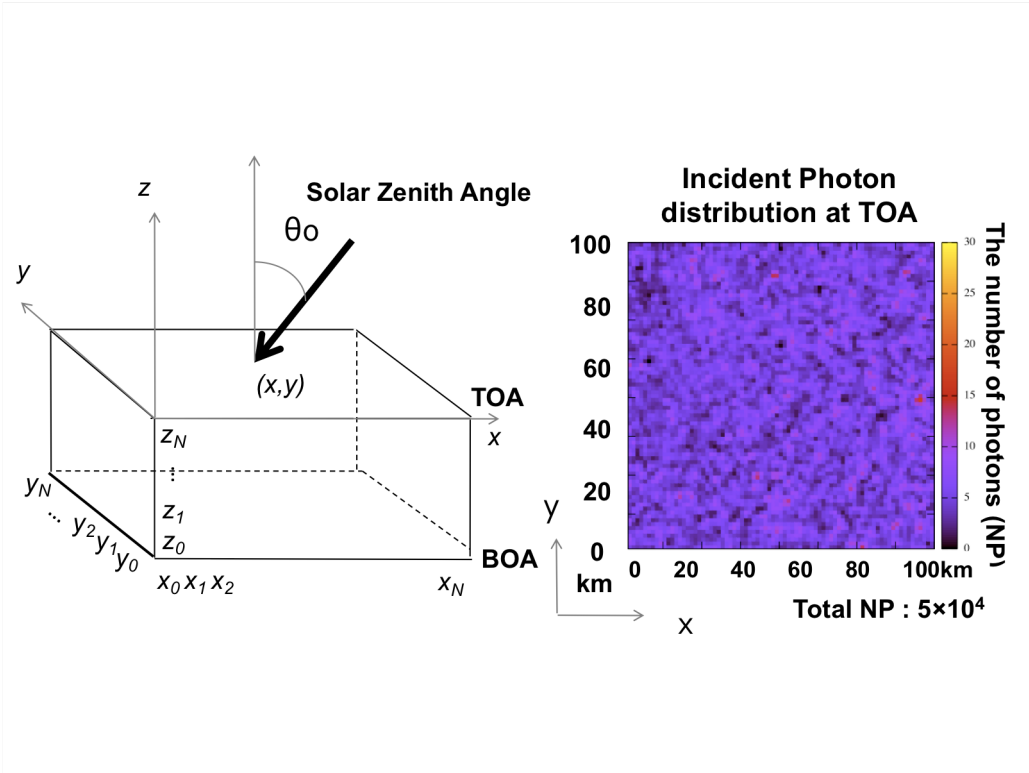

Figure 2.2. Right panel describes the model domain input model photon from a given radiation source and start ray tracing. θ_0 means solar zenith angle. The left panel shows the incident photon distribution at TOA in the model domain (100km × 100km) as sunlight approximated by number of photons (NP) as 5×10^5.

$$\tau = \int_{\mathbf{r}_1}^{\mathbf{r}_2} e(\mathbf{r})\, dr \approx \sum_{i=1}^{\text{boxes}} r_i \cdot e_i \,, \tag{2.2.4}$$

where r_i defines the geometrical distance between two adjacent points among points of starting, crossing box boundary, or destination for extinction,

$$r_i = \sqrt{\Delta x_i^{\,2} + \Delta y_i^{\,2} + \Delta z_i^{\,2}} \,, \tag{2.2.5}$$

$$\triangle x_i^2 = (x_n - x_{n-1})^2, \quad \triangle y_i^2 = (y_n - y_{n-1})^2, \quad \triangle z_i^2 = (z_n - z_{n-1})^2, \quad n = 1,2,3,... \tag{2.2.6}$$

It is, therefore, the distance of the model photon to survive is given as follows,

$$\tau = \int_{\mathbf{r}_1}^{\mathbf{r}_2} e(\mathbf{r})\, dr = -\ln(R_3), \quad R_3 \in [0,1] \;\; , \tag{2.2.7}$$

where R_3 is a uniform random number to simulate the transmissivity T in Eq. (2.2.3). The next extinction point is thus determined by tracking the photon along an optical path in the model domain until the traveling distance matches the distance corresponding to the optical path length τ given by (2.2.7). In this event, the light intensity L_{n-1} is attenuated in the following manner by light absorption received at the point of extinction,

$$L_n = \omega \cdot L_{n-1} \,. \tag{2.2.8}$$

This method of determining the extinction event becomes inefficient for evaluation of scattered radiation, when SSA becomes small in the case of strong light absorption. The *MCstar* is also implemented with another type of decision making method for the scattering event. Instead of using the transmissivity for extinction (2.2.3), I can take the transmissivity for scattering as

$$T_{\mathbf{s}} = \exp(-\tau_{\mathbf{s}}) \tag{2.2.9}$$

$$\tau_s = \int_{r_1}^{r_2} s(\mathbf{r})\, dr \approx \sum_{i=1}^{cells} r_i \cdot s_i \tag{2.2.10}$$

where s_i is the volume scattering coefficient for the i-th box along the photon track.

It is, therefore, the distance of the model photon to survive is given as follows like (2.2.7),

$$\tau_s = \int_{\mathbf{r}_1}^{\mathbf{r}_2} s(\mathbf{r})\,dr = -\ln(R_3'), \quad R_3' \in [0,1] \quad , \tag{2.2.11}$$

where R_3' is a uniform random number to simulate the transmissivity T_s in Eq. (2.2.9).

In this case, I need a weighting by the transmissivity for absorption T_a,

$$L_n = T_a \cdot L_{n-1}\,. \tag{2.2.12}$$

$$T_a = \exp(-\tau_a)\,, \tag{2.2.13}$$

$$\tau_a = \int_{r_1}^{r_2} a(\mathbf{r})\,dr \approx \sum_{i=1}^{cells} r_i \cdot a_i\,, \tag{2.2.14}$$

where a is the volume absorption coefficient for the i-th box.

Either the extinction event point method or the scattering event method have to be selected depending on each application. I apply the extinction event method to SW region calculation, on the other hand, I adapt the scattering event method to LW region calculation.

(3) Decision of the scattering angle

When the interaction point is determined by step (2) and if the SSA is larger than 0, the next scattering angle for L_n to travel for next extinction event is determined by the cumulative scattering phase function as defined as

$$Q_{ijk}(\Theta) = \frac{2\pi \int_0^{\Theta} P_{ijk}(\cos\Theta')\,d\cos\Theta'}{2\pi \int_0^{\pi} P_{ijk}(\cos\Theta')\,d\cos\Theta'}\,, \tag{2.2.15}$$

where $P(\Theta)$ and $Q(\Theta)$ phase function and accumulated phase function as a function of the scattering angle Θ, respectively. Subscripts (i, j, k) mean coordinates of atmospheric boxes. The scattering angle and zenith angle are decided by uniform random numbers as, R_4 and R_5 as,

$$Q(\Theta) = R_4, \quad \Phi = 2\pi R_5, \quad R_4, R_5 \in [0,1]. \tag{2.2.16}$$

Note that Q is a monotonic function on the range [0, 1] by its definition. In order to retrieve Θ from the above equation, I need the inverse function of Q, i.e. $\Theta = Q^{-1}(R_4)$. For this purpose, I can make a look-up table (LUT) of (Θ_i, Q_i),

$$\{\Theta_i, Q_i = g(i), i = 0, N_\Theta\}, \tag{2.2.17}$$

where g is a mapping function that should be simple for efficient calculation. The simplest function is a linear function,

$$g(i) = \frac{i}{N_\Theta}. \tag{2.2.18}$$

If the phase function is prescribed for the experiment, this is the most efficient method. It is, however, difficult to use this method for the complex mixture of atmospheric constituents, because the phase function is composed of the linear combination of those of multiple constituents as given by

$$P(\Theta) = \frac{1}{s}\sum_{m=1}^{M} s_m P_m(\Theta), Q(\Theta) = \frac{1}{s}\sum_{m=1}^{M} s_m Q_m(\Theta), \tag{2.2.19a}$$

$$s = \sum_{m=1}^{M} s_m, \tag{2.2.19b}$$

where the subscript m is the number of constituents. As this formula indicates, there is no simple inverse function of $P(\Theta)$. In this situation, I tested several methods of obtaining the inversion Q^{-1}. First, I tested a method to determine the scattering composition depending on the ratio, s_m/s, using a uniform random number, then the corresponding cumulative phase function $Q_m(\Theta)$ is inverted using a similar method to (2.2.17). But it is found that this method resulted in a slow convergence of the radiance.

Another method is a non-linear numerical solution of a monotonic function as described as,

$$\begin{aligned}&\Theta_1 = 0, \Theta_2 = \pi \rightarrow \text{*estimate } \Theta \text{ from } (Q(R_4),\ Q(\Theta_1), Q(\Theta_2)) \\ &\rightarrow \text{if } Q(\Theta) \geq Q(R_4) \text{ then } \Theta_2 = \Theta \text{ else } \Theta_1 = \Theta \rightarrow *\end{aligned} \tag{2.2.20}$$

In this method, the calculation can converge at about 10 times for the scattering angle decision, i.e. CPU time become not very long compared to that of the liner method in Eq. (2.2.17).

Ray tracing is represented by a series of rotating operations based on the coordinate system shown in Fig. 2.3 The conversion between two basis vectors $\{\mathbf{e}'_i\}$ and $\{\mathbf{e}_i\}$ is generated by rotation **R** of Cartesian coordinates as follows,

$$\mathbf{R}\mathbf{e}'_i = \mathbf{e}_i, \quad \mathbf{e}'_i = \mathbf{R}^{-1}\mathbf{e}_i \tag{2.2.21}$$

$\mathbf{R}^{-1}$ is the inverse matrix of **R** (equal to the transport matrix $\mathbf{R}^t$ between the Cartesian coordinate systems). Coordinates of the location vector **r** are represented by two coordinate systems,

$$\mathbf{r} = x_i\mathbf{e}_i = x'_i\mathbf{e}'_i, \tag{2.2.22a}$$

or

$$x'_i = x_j\mathbf{e}'_i \cdot \mathbf{e}_j = (\mathbf{R}^{-1})_{ji}x_j = R_{ij}x_j, \quad x_i = R^t_{ij}x'_j, \tag{2.2.22b}$$

where summation of dimension subscript-i is assumed using the Einstein convention. Rotation matrices around the coordinate axes ($\mathbf{e}_3$, $\mathbf{e}_1$, $\mathbf{e}_2$) for a roatation angle ϕ can be represented by the Cartesian coordinates of ($\mathbf{e}_1$, $\mathbf{e}_2$, $\mathbf{e}_3$) as,

$$\mathbf{R}^{xy}(\phi) = \begin{pmatrix} \cos\phi & -\sin\phi & 0 \\ \sin\phi & \cos\phi & 0 \\ 0 & 0 & 1 \end{pmatrix}, \mathbf{R}^{yz}(\phi) = \begin{pmatrix} 1 & 0 & 0 \\ 0 & \cos\phi & -\sin\phi \\ 0 & \sin\phi & \cos\phi \end{pmatrix}, \mathbf{R}^{zx}(\phi) = \begin{pmatrix} \cos\phi & 0 & \sin\phi \\ 0 & 1 & 0 \\ -\sin\phi & 0 & \cos\phi \end{pmatrix} \tag{2.2.23}$$

I treat the problem of a unit vector **r** incident on a point **P** and scattered in a direction $\mathbf{r}_s$. Four coordinate systems, i.e. $\{\mathbf{e}_i\}$, $\{\mathbf{e}'_i\}$, $\{\mathbf{e}''_i\}$, $\{\mathbf{e}^s_i\}$ as shown in Fig. 2.3, can be defined. The first coordinate system is a fixed coordinate system to the earth system. The second coordinate system is a coordinate that is taken $\mathbf{e}_1$-axis in the meridional plane to align **r**

with $\mathbf{e}_3$. The third coordinate is a coordinate system taking the incident vector $\mathbf{r}$ to be $\mathbf{e}'_3$ obtained by rotating the $\mathbf{e}_3$ in the meridional plane. The last one is a coordinate system that conforms to the scattering surface. The rotation angle Φ around the scattering angle Θ and $\mathbf{r}$ is expressed in the following manner,

$$\angle rzr_s = \Theta, \quad \angle r_s rz = \pi - \Phi \,. \tag{2.2.24}$$

The $\mathbf{r}_s$ can be represented on the Earth coordinate system by successive rotations as,

$$\{\mathbf{e}_i^s\} - \mathbf{R}^{x^s y^s}(-\Phi) \rightarrow \{\mathbf{e}_i''\} - \mathbf{R}^{z''x''}(-\theta) \rightarrow \{\mathbf{e}_i'\} - \mathbf{R}^{x'y'}(-\phi) \rightarrow \{\mathbf{e}_i\} \,, \tag{2.2.25}$$

$$\mathbf{R} = \mathbf{R}^{x'y'}(-\phi)\mathbf{R}^{z''x''}(-\theta)\mathbf{R}^{x^s y^s}(-\Phi) = \begin{pmatrix} \cos\theta\cos\phi\cos\Phi - \sin\phi\sin\Phi & \cos\theta\cos\phi\sin\Phi + \sin\phi\cos\Phi & -\sin\theta\cos\phi \\ -\cos\theta\sin\phi\cos\Phi - \cos\phi\sin\Phi & -\cos\theta\sin\phi\sin\Phi + \cos\phi\cos\Phi & \sin\theta\sin\phi \\ \sin\theta\cos\Phi & \sin\theta\sin\Phi & \cos\theta \end{pmatrix} \tag{2.2.26}$$

Therefore, in case of incidence to $\mathbf{e}^s_3$-axis in scattering plane,

$$\mathbf{r}^{x_s y_s z_s} = \begin{pmatrix} 0 \\ 0 \\ 1 \end{pmatrix} \,. \tag{2.2.27}$$

The relationship between the polar coordinates (θ,ϕ) and a global coordinates are given as,

$$\mathbf{r}^{xyz} = \mathbf{R}^t \mathbf{r}^{x_s y_s z_s} = \begin{pmatrix} \sin\theta\cos\phi \\ \sin\theta\sin\phi \\ \cos\theta \end{pmatrix}, \tag{2.2.28}$$

$$\mathbf{r}_s^{x_s y_s z_s} = \begin{pmatrix} \sin\Theta \\ 0 \\ \cos\Theta \end{pmatrix}, \tag{2.2.29}$$

$$\mathbf{r}_s^{x''y''z''} = \mathbf{R}^t \mathbf{r}_s^{x_s y_s z_s} = \begin{pmatrix} \cos\theta\cos\phi\cos\Phi - \sin\phi\sin\Phi & -\cos\theta\cos\phi\sin\Phi - \sin\phi\cos\Phi & \sin\theta\cos\phi \\ \cos\theta\sin\phi\cos\Phi + \cos\phi\sin\Phi & -\cos\theta\sin\phi\sin\Phi + \cos\phi\cos\Phi & \sin\theta\sin\phi \\ -\sin\theta\cos\Phi & \sin\theta\sin\Phi & \cos\theta \end{pmatrix} \begin{pmatrix} \sin\Theta \\ 0 \\ \cos\Theta \end{pmatrix}$$

$$= \begin{pmatrix} (\cos\theta\cos\phi\cos\Phi - \sin\phi\sin\Phi)\sin\Theta + \sin\theta\cos\phi\cos\Theta \\ (\cos\theta\sin\phi\cos\Phi + \cos\phi\sin\Phi)\sin\Theta + \sin\theta\sin\phi\cos\Theta \\ -\sin\theta\cos\Phi\sin\Theta + \cos\theta\cos\Theta \end{pmatrix} \tag{2.2.30}$$

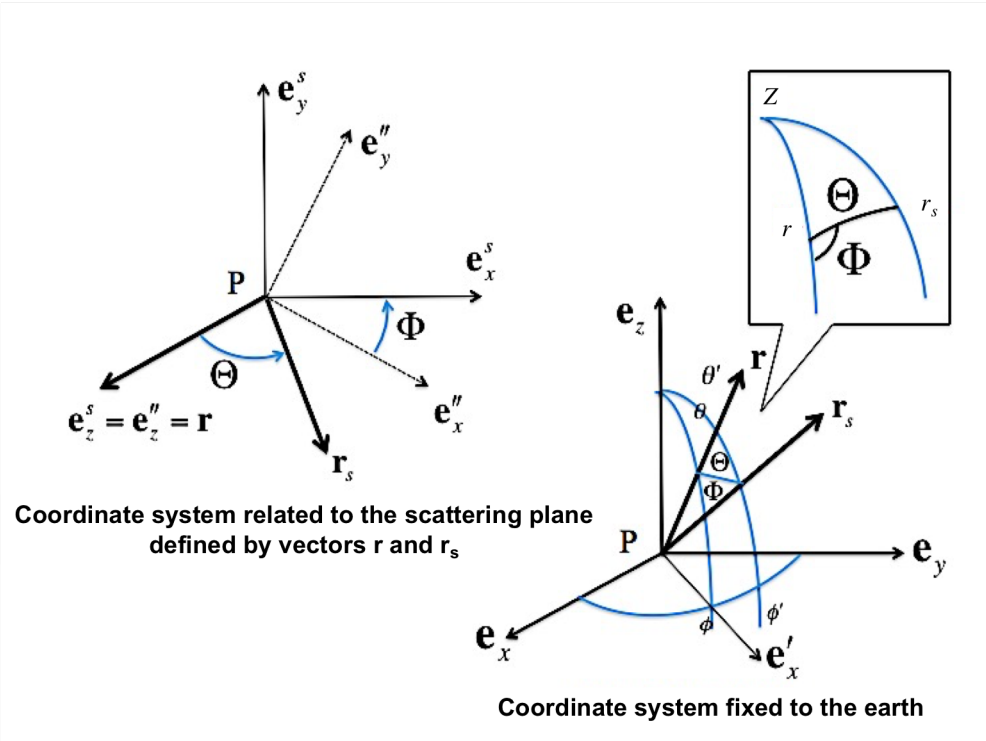

Figure 2.3. Coordinate systems used for ray tracing.

(4) Cyclic boundary condition and surface condition

The *MCstar* has a function of posing the cyclic boundary condition to the model domain for RT calculation. *MCstar* also has a function of surface reflection with a bidirectional distribution function (BRDF) or a simple Lambertian reflection when the model photon reaches to the surface during tracing in the domain.

I define the bidirectional reflection function of the surface or Bidirectional Reflection Distribution Function (BRDF) $\tilde{R}$ as

$$L_{out}(-\mu_r,\phi_r)=\frac{1}{\pi}\int_0^1 d\mu'\int_0^{2\pi} d\phi'\tilde{R}(-\mu_r,\mu';\phi_r,\phi')\mu' L_{in}(\mu',\phi'), \tag{2.2.31}$$

where ($-\mu_r$, ϕ_r) are the cosine of the zenith angle θ and the azimuthal angle of the model photon direction. $-\mu$ means upward direction for the surface reflection. If a plane parallel insolation is applied to the surface, I have

$$L_{in}(\mu,\phi)=F_0\delta(\mu-\mu_0)\delta(\phi-\phi_0), \tag{2.2.32}$$

$$L_{out}(-\mu_r,\phi_r)=\frac{1}{\pi}\tilde{R}(-\mu_r,\mu_0;\phi_r,\phi_0)\mu_0 F_0. \tag{2.2.33}$$

$\tilde{R}$ is, therefore, also referred to as the apparent reflectivity in the satellite remote sensing studies.

If I assume the reflected radiance does not depend on the emerging angles ($-\mu_r$, ϕ_r), i.e. a Lambertian surface, the reflected flux is given as follows,

$$F_{out}=\int_0^1 d\mu\int_0^{2\pi} d\phi\mu L_{out}=\pi L_{out}=\tilde{R}(\bullet,\mu_0;\bullet,\phi_0)\mu_0 F_0. \tag{2.2.34}$$

and the surface flux reflectance (ground albedo) A_g,

$$A_g=\frac{F_{out}}{\mu_0 F_0}=\tilde{R}_L. \tag{2.2.35}$$

The zenith angle θ_r and azimuth angle ϕ_r of the reflected photon track is determined by uniform random numbers R_6 and R_7 to simulate the angular integration of Eq. (2.2.31) as,

$$\cos\theta_r = \sqrt{R_6}, \qquad \phi_r = 2\pi R_7 . \tag{2.2.36}$$

The model photon is weighted with the probability based on surface albedo A_g from Eqs. (2.2.31) and (2.2.35),

$$L_n = A_{g\ ij} \cdot L_{n-1} . \tag{2.2.37}$$

For the domain averaged solar radiative flux calculation, ray tracing is repeated the step (1) through (4), and the number of model photon which reach TOA is counted as reflected radiative flux and the number of model photon which reach to BOA is counted as transmitted radiative flux. Equation (2.9) can be re-described for flux calculation as follows,

$$F_j = \mu_0 F_0 \frac{1}{N} \sum_{i=1}^{N_j} w_i \cdot L_i, \qquad (j = 1, 2), \tag{2.2.38}$$

where w means the weight function, i.e. ω or T_a and A_g and j= 1 for the reflected radiative flux at TOA and j= 2 for the transmitted radiative flux at BOA, respectively; N_j are the total numbers of photons which reach TOA (j=1) and BOA (j=2) and inputted in the sampling area, respectively; N is the total number of inputted photons.

(5) Backward tracing and truncation of the phase function

For radiance calculation, I adopt the backward Monte Carlo method, in which the model photon is traced from the receiver to sun direction (solar zenith angle). The steps (1) through (4) are repeated as same as in the forward Monte Carlo method. First, the path length of the model photon, between current point and next interaction point, is decided by extinction or scattering transmissivity, depending on the method of interaction by Eqs. (2.2.7) or (2.2.11). Second, I decide the scattering direction of the model photon using accumulated phase function by Eq. (2.2.16) and (2.2.19a,b). The scattering angle and zenith angle are decided by random numbers in Eq. (2.2.16) and (2.2.20). If the model photon reaches the ground surface during tracing in the regional space, I also decide the reflected zenith angle θ_r and azimuth angle ϕ_r by uniformed random numbers depending on the surface albedo given Eq. (2.2.36). One difference from the forward method is to count the contribution of the attenuated solar radiation

reaching the scattering point by the transmittivity *T(g)* given in Eq. (2.2.3) with the optical path length calculated by Eq. (2.2.4) along the slant path to the sun.

Because the phase function for particulate matter has a strongly peaked forward scattering formed by light diffraction, a very fine angular resolution is required for accurate solution of RTE. An important process in the backward Monte-Carlo method is also how to save the computing time for accurate calculation of the radiance which is more angle dependent than the radiative flux calculation. For this purpose, I separate the single and multiply scattered solar radiances: The first order scattering radiance is given as,

$$L_1(\mathbf{r},\mu,\phi) = F_0\omega(\mathbf{r})P(\mathbf{r},\mu,\mu_0;\phi,\phi_0)\exp(-\left\{\int_{\mathbf{r}}^{exit} e(\mathbf{r}')dr' + \int_{incident}^{\mathbf{r}} e(\mathbf{r}')dr'\right\}), \quad (2.2.39)$$

where the first and second terms in the exponent is respectively the photon path from the solar insolation point at TOA, i.e. **r**=0, to the scattering event point $\mathbf{r}'$, and from $\mathbf{r}'$ to the exit point at TOA, i.e. **r**. In the Single to Multiple scattering (MS) method, I calculate the radiance as

$$L = L' - L_1' + L_1, \quad (2.2.40)$$

where L' and L'_1 are the radiance and its single scattering component calculated by the Monte-Carlo, and L_1 is the exact solution of the single scattering radiance calculated by Eq. (2.2.39). It is, however, known that this solution includes undesired Gibbs-phenomenon type fluctuation in the angular distribution of radiance (Nakajima and Tanaka, 1988), when the forward peak of the phase function is truncated by the delta-M method (Wiscombe, 1977),

$$P(x) \approx \frac{f}{2\pi}\delta(x-1) + (1-f)P^*(x), \quad (2.2.41a)$$

$$x = \cos\Theta, \quad (2.2.41b)$$

$$s^* = fs, e^* = (1-f\omega)e, \quad \omega^* = \frac{1-f}{1-f\omega}\omega \quad , \quad (2.2.41c)$$

where f is the truncation factor and the phase function is expanded by Legendre polynomials,

$$P(\cos\Theta, g, M) = \frac{1}{4\pi}\sum_{n=0}^{M}(2n+1)g_n P_n(\cos\Theta), \tag{2.2.42}$$

and truncate it at an order M^* to obtain the truncated phase function P^* uniquely given by the moments as,

$$g_n^* = (g_n - f)/(1-f), \quad f = g_{M^*+1}, \tag{2.2.43}$$

$$P(\cos\Theta, g, M^*+1) = fP(\cos\Theta, 1, M^*+1) + (1-f)P(\cos\Theta, g^*, M^*), \tag{2.2.44}$$

$$P^*(\cos\Theta) = P(\cos\Theta, g^*, M^*). \tag{2.2.45}$$

I use discrete quadrature of order $2N_{qd}$ for a phase function with $M \leqq 2N_{qd}$. In order to suppress the angular fluctuation, I introduce the TMS method of Nakajima and Tanaka (1988) for the radiance calculation. In this method, Monte-Carlo method is applied to the truncated space with τ^*, ω^* and P^* to calculate truncated radiance L_{MC}^* and truncated single scattering radiance $L_{1,MC}^*$ for the following correction,

$$L \approx L_{MC}^* - L_{1,MC}^* + \tilde{L}_1^*, \tag{2.2.46}$$

where $\tilde{L}_1^*$ is the scaled single scattering radiance defined by Eq. (2.2.39) but with the truncated extinction coefficient e^* and scaled phase function $\omega P/(1-f\omega)$ instead of ωP as follows,

$$\tilde{L}_1^*(\mathbf{r}, \mu, \phi) = F_0 \int_0^{\mathbf{r}} \frac{\omega(\mathbf{r}', ich)}{1 - f(\mathbf{r}')\omega(\mathbf{r}', ich)} P(\mathbf{r}', \mu, \mu_0; \phi, \phi_0) \exp\left\{ -\int_{\mathbf{r}' \, to \, \mathbf{r}} e^*(\mathbf{r}'', ich) dr'' - \int_{start \, to \, \mathbf{r}'} e^*(\mathbf{r}'', ich) dr'' \right\} dr', \tag{2.2.47}$$

where I denote the optical parameters depending on the atmospheric box (i,j,k) and k-distribution term ich.

The TMS approximation is known to be accurate for reflected radiances. For the downward sky radiance calculation, I need the IMS method with secondary scattering correction (Nakajima and Tanaka, 1988).

2.2.2 Monte Carlo radiative transfer algorithm for thermal infrared radiative flux and radiance

In the Monte Carlo calculation of the LW radiation transfer, I have to evaluate the effects of thermal emission from all parts of the model domain.
The general RTE (2.1a) can be written as,

$$\frac{dL(\mathbf{r},\mu,\phi)}{dr} = -e(\mathbf{r})L(\mathbf{r},\mu,\phi) + s(\mathbf{r})\int_0^{2\pi}\int_{-1}^{1} P(\mathbf{r},\mu,\mu';\phi,\phi')L(\mathbf{r},\mu',\phi')d\mu' d\phi' + a(\mathbf{r})B(\mathbf{r}) . \tag{2.2.48}$$

Because $a>>s$ in most of the LW spectral region, a dominant component is a non-scatting intensity L_a as defined by the following RTE,

$$\frac{dL_a(\mathbf{r},\mu,\phi)}{dr} \equiv -e(\mathbf{r})L_a(\mathbf{r},\mu,\phi) + a(\mathbf{r})B(\mathbf{r}) . \tag{2.2.49}$$

Note that this equation keeps the extinction coefficient e in the first term of the rhs equation, that is different from the non-scattering approximation assuming ω= 0, i.e. e= a. The total intensity is then formulated with L_a and a correction L' as,

$$L = L_a + L' , \tag{2.2.50}$$

where L' satisfies the following equation:

$$\frac{dL'(\mathbf{r},\mu,\phi)}{d\mathbf{r}} = -e(\mathbf{r})L'(\mathbf{r},\mu,\phi) + s(\mathbf{r})\int_0^{2\pi}\int_{-1}^{1} P(\mathbf{r},\mu,\mu';\phi,\phi')L'(\mathbf{r},\mu',\phi')d\mu' d\phi' + J(\mathbf{r},\mu,\phi) , \tag{2.2.51}$$

$$J(\mathbf{r},\mu,\phi) \equiv s(\mathbf{r})\int_0^{2\pi}\int_{-1}^{1} P(\mathbf{r},\mu,\mu';\phi,\phi')L_a(\mathbf{r},\mu',\phi')d\mu' d\phi' . \tag{2.2.52}$$

I solve Eq. (2.2.49) in the present study as follows. First, the non-scattering solution L_a is integrated along the photon path as,

$$L_a(\mathbf{r}) = \int_0^{\mathbf{r}} a(\mathbf{r}')B(\mathbf{r}')exp[-\int_{\mathbf{r}'}^{\mathbf{r}} e(\mathbf{r}'')d\mathbf{r}'']d\mathbf{r}' + B_0 \exp[-\int_0^{\mathbf{r}} e(\mathbf{r}')d\mathbf{r}'], \qquad (2.2.53)$$

where B_0 is the emission at the boundary at the coordinate origin. I define the optical path length along the photon path and the transmittance,

$$u(\mathbf{r},\mathbf{r}') \equiv \int_{\mathbf{r}'}^{\mathbf{r}} e(\mathbf{r}'')d\mathbf{r}'', \qquad (2.2.54)$$

$$T(\mathbf{r},\mathbf{r}') \equiv \exp[-u(\mathbf{r},\mathbf{r}')]. \qquad (2.2.55)$$

Assuming that $(1-\omega)B$ is a slow function of u in a Monte Carlo box for a range of (u_1, u_2), I expand it as,

$$[1-\omega(\mathbf{r}')]B(\mathbf{r}') \approx c_0 + c_1 u, \qquad u \in [u_1, u_2]. \qquad (2.2.56)$$

Then L_a can be analytically calculated along the photon path. This treatment is especially important to calculate a small heating rate in the LW region. I set the receiver for the solution of Eq. (2.2.53) as follows. In case of satellite-received upward radiance calculation, I locate a receiver at TOA and enter the photons into the model domain from the direction of the satellite viewing angle. In case of upward flux calculation, I locate a receiver at TOA and enter the photons form randomized direction, i.e. $0 \le \mu \le 1$, $0 \le \phi \le 2\pi$. I perform the solid angle integrations of Eq. (2.2.53). The algorithm solves the problem that the emitted photons from entire domain do not reach receivers due to large light absorption. Although the present algorithm is applicable by the forward method, the computation efficiency is low.

However, I solve Eq. (2.2.51) by the backward Monte Carlo method. I set the receiver for this solutions as same as the solution of Eq.(2.2.53). First, I decide the source point as Eq. (2.2.52) by the backward Monte Carlo ray tracing method. Second, I analytically calculate L_a in rhs of Eq.(2.2.52) from randomize directions (μ', ϕ') by Eq. (2.2.53) to get the source function J given by Eq. (2.2.52). The randomize direction is determined by using the accumulated phase function and random number in Eq. (2.2.16) and (2.2.20). I exam about 10 more photons for accurate evaluation of the source term because the phase function is not completely isotropic. It turns out that approximately

10 more photons are enough to converge the error. Finally, I solve Eq. (2.2.51) to get L' by a backward Monte Carlo ray tracing method similar to the case of solar radiation.

2.2.3 Optical models of cloud and atmosphere

2.2.3.1 Atmosphere model

In the radiative transfer of the Earth's atmosphere problem, I need to deal with scattering and absorption by molecules, aerosols, and clouds in the atmosphere. These phenomena are quantified by the scattering cross section and absorption cross section. For example, the volume scattering, absorption and extinction coefficients of a mono-disperse particle system are represented by respective cross sections and the number density N, as follows,

$$s = C_{sca}N, \quad a = C_{abs}N, \tag{2.2.57a}$$

$$e = s + a, \tag{2.2.57b}$$

In addition, the scattered light depending on the scattering angle Θ is described by the differential scattering cross section or scattering phase function as,

$$dL = sP(\cos\Theta)dx, \tag{2.2.58}$$

The volume optical coefficients of the entire air mass is then expressed by the sum of contributions of air molecules and particles as,

$$a = a_m + a_c, \quad s = s_m + s_c, \quad e = e_m + e_c, \tag{2.2.59}$$

$$sP(\cos\Theta) = s_m P_m(\cos\Theta) + s_c P_c(\cos\Theta), \tag{2.2.60}$$

The subscripts of m and c mean air molecule and particle, respectively.
Single scattering albedos are represented as follow,

$$\omega = \frac{s}{a}, \quad \omega_m = \frac{s_m}{e_m}, \quad \omega_c = \frac{s_c}{e_c}. \tag{2.2.61}$$

In our study the number size distribution is assumed to follow a log-normal distribution,

$$n(x) = \frac{N}{\sqrt{2\pi}\sigma} \exp[\frac{1}{2}\left(\frac{x - x_m}{\sigma}\right)^2] , \tag{2.2.62a}$$

$$x = \ln(r), x_m = \ln(r_m) . \tag{2.2.62b}$$

where r_m is the mode radius and σ the standard deviation. The cross sections and scattering phase functions are calculated by Rayleigh scattering theory, Mie scattering theory (van de Hulst, 1957), and various non-spherical scattering theories. I show examples of the photon tracing in the atmosphere in Fig 2.4.

Fig 2.4 includes the information of the asymmetry parameter *g,*

$$g \equiv \int_{4\pi} P(\cos\Theta)\cos\Theta \, d\Omega . \tag{2.2.63}$$

The asymmetry parameter is interpreted as the asymmetricity of the phase function taking a range of

$$-1 \le g \le 1 . \tag{2.2.64}$$

If $g = 0$, photons are isotropically scattered to undergo more multiple scatterings than in case of $g = 0.85$ as shown in the figure. It is, therefore, found that the asymmetry of the scattering phase function is an important factor to control the photon path distribution in the Monte-Carlo method.

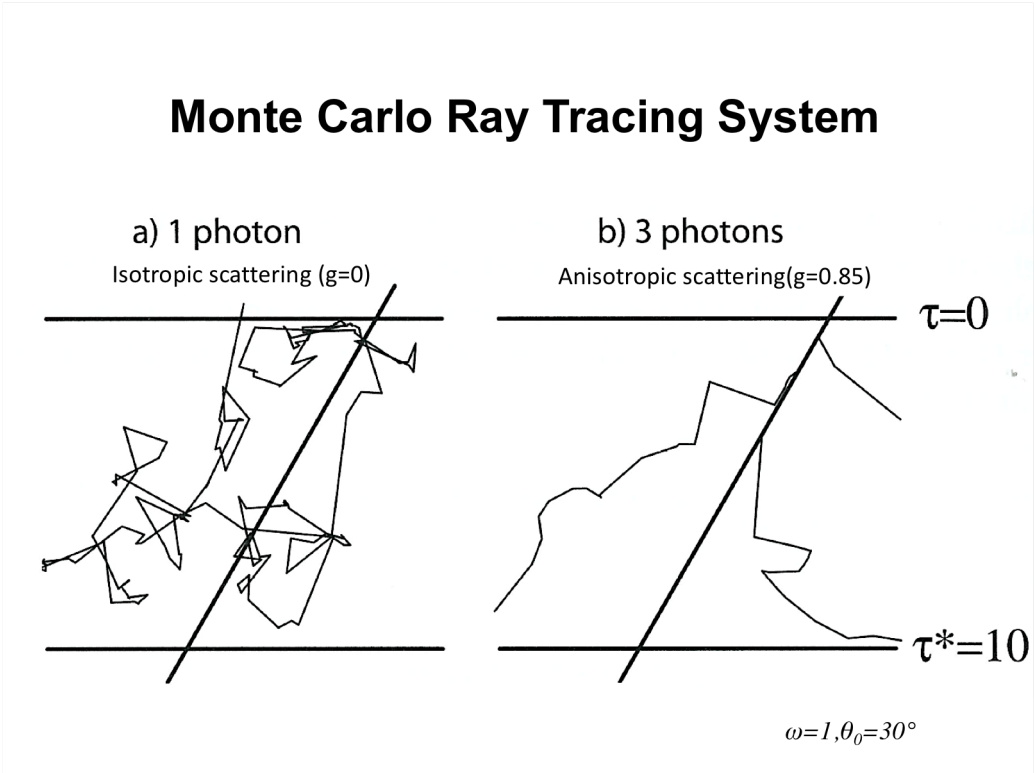

Figure 2.4. Example of random paths of photons in a plane-parallel scattering layer with an optical thickness $\tau^*=10$. Photons are incident from $\theta_0=30^\circ$. Heavy diagonal lines indicate the path of an un-scattered photon would take. (a) The trajectory of a single photon when scattering is isotropic, and (b) trajectories of three photons when an asymmetry parameter is g=0.85 which is typical for clouds in the SW band. (Petty 2004).

2.2.3.2 Light absorption of atmospheric gases

Conventionally, the photon path distribution method has been used to treat the light absorption by gaseous constituents in the atmosphere (Marshak and Davis, 2005). In this method, I perform ray tracing to determine the photon path distribution function f by computing the optical length x assuming no absorption condition. I obtain a light absorption amount A of the atmosphere by making the integral of the transmittance of the absorption and f,

$$A = \int f(x)\exp(-ax)\,dx \ , \tag{2.2.65}$$

where a is an absorption coefficient for the path distribution.

This method is efficient when I have a relatively simple structure of particle and gas distributions in the atmosphere. However, if optical parameters (cross-sections and the phase function) of air molecules and particles are significantly different throughout the scattering medium, I cannot find a representative single value a for the absorption coefficient to perform Eq. (2.2.65). Also the value of optical properties are different from each wavelength, therefore I have to obtain the path radiance for each wavelengths.

The correlated k-distribution method theory (Lacis and Oinas, 1991), on the other hand, is a more flexible method that can treat the multiple scattering problem in a spectral band based on an approximation for the wavelength integral of radiance using the probability density of the absorption coefficient, called k-distribution, $g(a)$ as

$$\overline{L} = \int_{\lambda_1}^{\lambda_2} L_\lambda \, d\lambda \approx \int_0^\infty L(a) g(a) da \approx \sum_{n=1}^{Nch} L(a_n) w_n \ , \tag{2.2.66}$$

where $\{a_n,\ w_n\}$ are the quadrature points and weights for k-distribution that is approximated by Nch equivalent wavelengths, called sub-channels. If I divide the target spectral region into Nb bands, I have the following formula for the total wavelength integration,

$$\overline{L} = \sum_{j=1}^{Nb} \int_{\lambda_j}^{\lambda_{j+1}} L_\lambda \, d\lambda \approx \sum_{j=1}^{Nb} \sum_{i=1}^{Nch(j)} L(a_{ij}) w_{ij} \, . \tag{2.2.67}$$

In this study, I implement a nonlinear *k*-distribution method of Sekiguchi and Nakajima (2008) which is also used in the *Rstar*. They proposed a non-linear optimization method to obtain optimized *k*-distribution parameters including those of overlapping bands, not relying on the correlation assumption of gaseous absorption coefficients in different atmospheric layers. The number of sub-channels *Nch* is set at 2, which is a standard set of *Rstar* code for narrow band calculation in a range of 0.2- 1000μm. For the broadband calculation, they set spectral bands of *Nb*= 29 including 111 sub-channels in a range of 0.2-200μm. I use the HITRAN gas parameter database (Rothman et al,. 2005).

2.2.3.3 Cloud structure and cloud physical and optical parameters

I assume that the scattering and absorption coefficients of gases depend only on the vertical direction simply, i.e. z-direction $\{z_k\}$, whereas those of cloud particles are inhomogeneously distributed depending on each box of the model domain $\{x_i, y_j, z_k\}$ as summarized in Table 1.

Optical parameters of the entire air mass are calculated as follows,

$$e_{c,ijk} = a_{c,ijk} + s_{c,ijk}, \quad e_{m,k,ich} = a_{m,k,ich} + s_{m,k,ich}, \tag{2.2.68}$$

$$e_{ijk,ich} = e_{c,ijk} + e_{m,k,ich}, \quad \omega_{ijk,ich} = \frac{s_{m,k} + s_{c,ijk}}{e_{ijk,ich}}, \tag{2.2.69}$$

$$P_{ijk}(\cos\Theta) = (1 - c_{ijk}) P_{m,k}(\cos\Theta) + c_{ijk} P_{c,ijk}(\cos\Theta), \tag{2.2.70}$$

$$c_{ijk} = \frac{s_{c,ijk}}{s_{c,ijk} + s_{m,k}}, \tag{2.2.71}$$

$$P_m(\cos\Theta) = \frac{3}{16\pi}(1+\cos^2\Theta) \quad . \tag{2.2.72}$$

The subscripts of *m* and *c* mean air molecule and particle, respectively.

Constituent	*absorption coefficient*	*scattering coefficients*	*Phase function*	*Effective radius*
Cloud	$a_{c,\,ijk}$	$s_{c,ijk}$	$P_{c,ijk}(\Theta)$	$r_{e,ijk}$
Gases	$a_{m,k,ich,}$ $ich=1,Nch$	$s_{m,k}$	$P_{m,k}(\Theta)$	-

Table 1. Optical parameters of the atmosphere.

The phase function does not depend on the *k*-distribution sub-channel, i.e. *ich*.

Cloud particles are assumed as water droplets. The optical parameters are calculated by Mie theory and the size distribution given Eq. (2.2.62a, b) with a standard deviation of *ln*(1.5), i.e. 0.41, and an effective radius given by satellite-retrieved values as discussed later.

The cumulative phase function Eq. (2.2.19a, b) for the whole air mass is expressed as,

$$Q_{ijk}(\cos\Theta) = (1-c_{ijk})Q_{m,\,k}(\cos\Theta) + c_{ijk}Q_{c,\,ijk}(\cos\Theta) \,. \tag{2.2.73}$$

2.3 Verification of *MCstar*

2.3.1 Selection of the random number generator

According to the central limit theorem, the sum of N random numbers is same probability distribution which has a mean, i.e. μ, and a root mean square deviation (RMSD) σ is related with Gaussian probability distribution which has a mean $\mu_N = \mu$ and a RMSD σ_N as follows,

$$\sigma_N = \frac{\sigma}{\sqrt{N}} . \tag{2.3.1}$$

In case of the uniform random number defined on [0, 1], I need N~2000 to attain $\sigma_N / \mu \sim 0.01$. This value is a necessary measurement of the number of random numbers for the Monte Carlo method. In the visible spectral region, it is seen that a very large number of multiple scatterings occur until the photon to escape from TOA because SSA of cloud particles such close to ω=1 as in Fig. 2.4. Therefore, the performance and speed of the random number generator is very important to obtain accurate results by the Monte Carlo method. In this study, I examine three kinds of uniform random number generators. Two kinds are based on the linear congruential method:

Random Number generator 1 (RN1):

$$X[n] = (X[n-1]+\pi)^5 - INT\left\{(X[n-1]+\pi)^5\right\}, \quad \pi = 3.141592653590 . \tag{2.3.2}$$

Random Number generator 2 (RN2):

$$X[n] = \left\{A \times X[n-1] + C(\text{mod } m)\right\} / (m+1), \quad A = 7^5, m = 2^{31} - 1 = 2147483647 . \tag{2.3.3}$$

And the Random Number generator 3 (RN3) is based on the Mersenne Twister method (Matsumoto and Nishimura, 1998). Mersenne Twister is known to be one of the pseudo random number sequence generators without many of drawbacks in the existing pseudo-random number generation methods. Figure 2.5 shows the behavior of random

number accuracy depending on the number of photons for the three types of uniform random generators defined range to [0,1]. Left and right panels indicate results of two cases with μ= 1/2 and σ= 1/3, respectively. The random number-1 (RN1) has a significant offset because this is generated by the constant π but with a limited number of digits in the digital computer to have a limited sequence period. On the other hand, the random number 2 (RN2) and Mersenne Twister can converge to zero within relative error of 0.01% after the number of random numbers 10^5. The RN 2 is known as a general random generator which is based on linear congruential method with its cycle of about 2^{62}. Excellent point of this random generator is that the execution time is short, so that it is beneficial for applications of speed priority. However, it is necessary to contrive to use the short cycle period. To solve this problem, I divide the total sequence into several sub-sequences with different seed numbers and using a random sequence after discarding 1000 initial part of whole random number. I examined two patterns of seed number selection. First, the number of random numbers set to 1×10^4 and perform 10 times random generations with different seed numbers, and second, the number of random numbers set to 5×10^4 and tried 2 times. The total number of the two patterns is same, then the two patterns should be comparably accurate similarly to Mersenne Twister. In conclusion, I decided to use RN 2 and Mersenne Twister in this study.

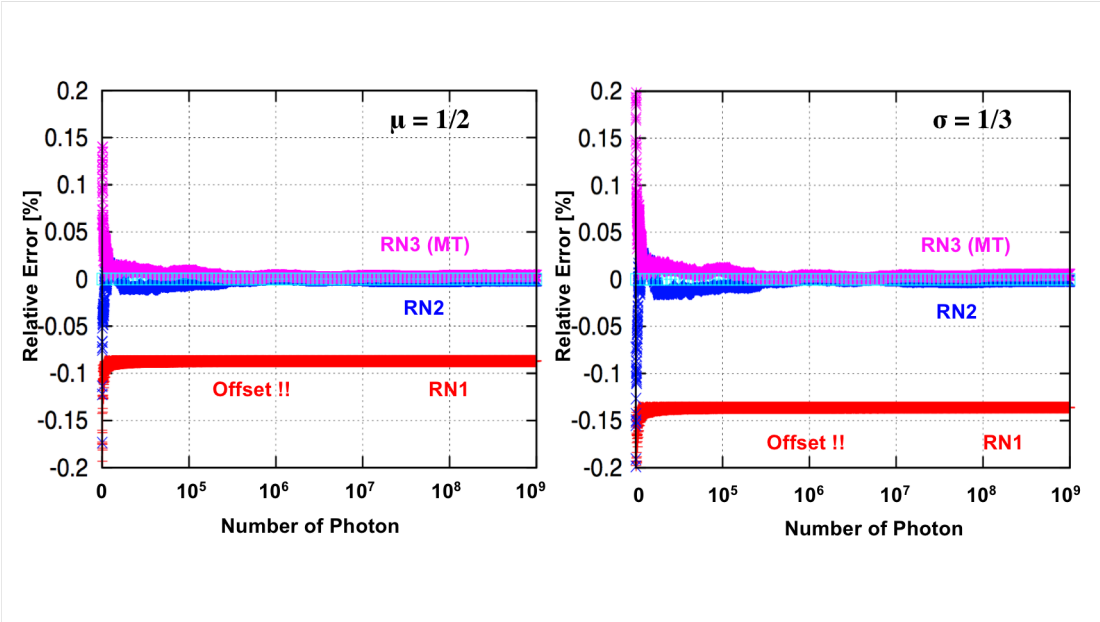

Figure 2.5. Behavior of random number errors depending on the number of photons for the three types of uniform random generators, RN1, RN2, and RN3 defined on [0,1]. Left and right panels indicate results of two cases with μ= 1/2 and σ= 1/3, respectively.

2.3.2 Verification for plane parallel conditions

This section gives a verification of *MCstar* compared with 1D-RT code. The *Rstar* code is a 1D-RT code, which is implemented with DOM-Adding method, truncation method of the phase function, and atmosphere and ocean interaction. It adopts a nonlinear *k*-distribution parameterization of gas absorption (Nakajima et al., 2000; Sekigushi and Nakajima., 2008). The number of the gaseous constituents is 28. These light absorption coefficients are based on HITRAN2004 absorption line table database. The built-in particle system includes 11 aerosol and cloud particle models. These parameters can be modified by users through overwriting data file to produce other types of internal and external polydispersions. The *Rstar* has 6 types of atmospheric models to define vertical profiles of pressure and trace gas concentrations. The *MCstar* have been built to use of these functions of *Rstar*.

In this section, I study 1) the performance of TMS-method solution in the *MCstar* comparing with the 1D original solution, and 2) accuracies of narrow and broadband SW and LW fluxes at TOA and BOA with the DM-method. I assume the liquid cloud model and the US standard atmosphere. The *MCstar* is applied to a 1D cloud layer with a log-normal size distribution assumption of r_m= 10μm (r_e=13μm) and σ = 0.35 in Eq. (2.2.62a, b). I also assume the zero ground surface albedo (A_g) to calculate fluxes over ocean for solar zenith angles (SZAs) up to 60° for which the ocean surface does not have a large reflectivity.

Figure 2.6 shows the relative error of the upward radiance at TOA calculated by the backward *MCstar* using TMS-method (in Section 2.2.1) as a function of viewing zenith angles θ= 0°~ 80° and for a solar zenith angle θ_0= 0°. The cloud optical thickness (COT) is set to τ_c= 0.8. The sampling area is set to 100 × 100 × 20 pixels in domain size of 100km × 100km × 5km and the total number of photons set to N_{ph}= 10^7. I confirm that it is enough to attain an accuracy with relative error less than 0.1% when the quadrature order for angular integration N_{qd} is more than 20. This is consistent with the report by Nakajima and Tanaka (1988) for their cloud case. Figure 2.7 shows the relative errors of upward radiances with TMS-method and untruncaed version depending on the input photon number N_{ph}, respectively. The solid line shows errors of TOA radiance

calculated by the backward *MCstar* using TMS-method solution (N_{qd} = 20) for θ= 60° and the dashed line for results without a truncation method. Other model conditions are same as in Fig. 2.6. The solution by the TMS-method makes radiance calculation more accurate than that without a truncation method for N_{ph} exceeding 4×10^5 especially. I also examined in Fig. 2.8 TOA radiances with different COTs and effective particle radii (REs) at visible (0.75μm) and near infrared (2.16μm) wavelengths to reproduce the Nakajima-King diagram (Nakajima and King, 1990) by the backward *MCstar* with N_{ph}= 10^7. I assume the angular condition and cloud particle size distribution same as theirs. The figure indicates the *MCstar* can produce a comparable accuracy of radiance calculation for satellite retrieval of the cloud optical properties using the solar reflection method.

For narrow and broad band flux verification, I give a 10^6 photons with each monochrome calculation, for a total of 10^9 photons for solar and infrared broadband radiative flux calculation to $100\times100\times20$ pixels in domain size of 100km$\times$100km$\times$5km that compose a model domain to secure the relative error less than 0.1% and 0.5% for area-averaged SW and LW broadband radiative fluxes, respectively. This sequence is repeated by the total number of band and sub-band channels, *Nb* x *Nch* in Eq. (2.2.67), i.e., 111 times for wavelength integration from 0.2μm to 200μm. As for the narrowband calculation I repeat the sequence *Nch*= 2 times for each band. A Gaussian quadrature order of N_{qd}= 10 is assumed for the DM-method. Figure 2.9 shows relative errors of the *MCstar* calculation with forward Monte Carlo method for SW flux calculation and with new backward Monte Carlo method for LW flux calculation in the upward and downward broadband fluxes at TOA and BOA for SW (0.2-4μm) and LW (4-200μm) spectral bands. I include the cloud and molecular radiative effects, but ignore the aerosol radiative effect in our calculations. I also examined the effect of the total number of photon to the accuracy of band calculation. It is found that the maximum number photon is ~10^6 at $\lambda=0.5\mu m$ and the minimum is less than ~10^4 in LW region.

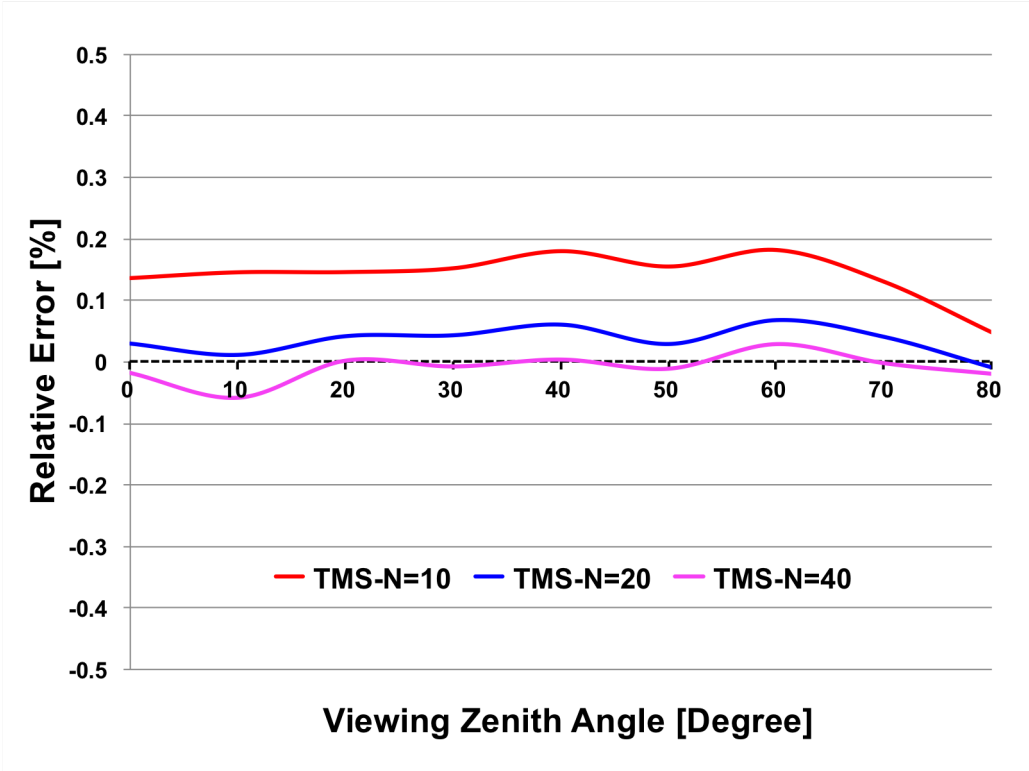

Figure 2.6. Relative errors in the upward radiance at TOA calculated by the backward *MCstar* using TMS-method as a function of viewing angles θ= 0°~ 80°. Three lines represent results with quadrature orders, N_{qd}= 10, 20, and 40. SZA is set to θ_0= 0°. The model domain consists of 100 ×100×20 pixels in domain size of 100km x 100km x 5km with cyclic boundary condition to simulate a 1D water cloud layer with τ_c= 0.8 and a log-normal particle size distribution of r_m= 10μm and σ = 0.35 with no ground albedo A_g=0. Relative humidity and temperature profiles are of the US standard atmosphere. Total photon number is N_{ph}= 10^7.

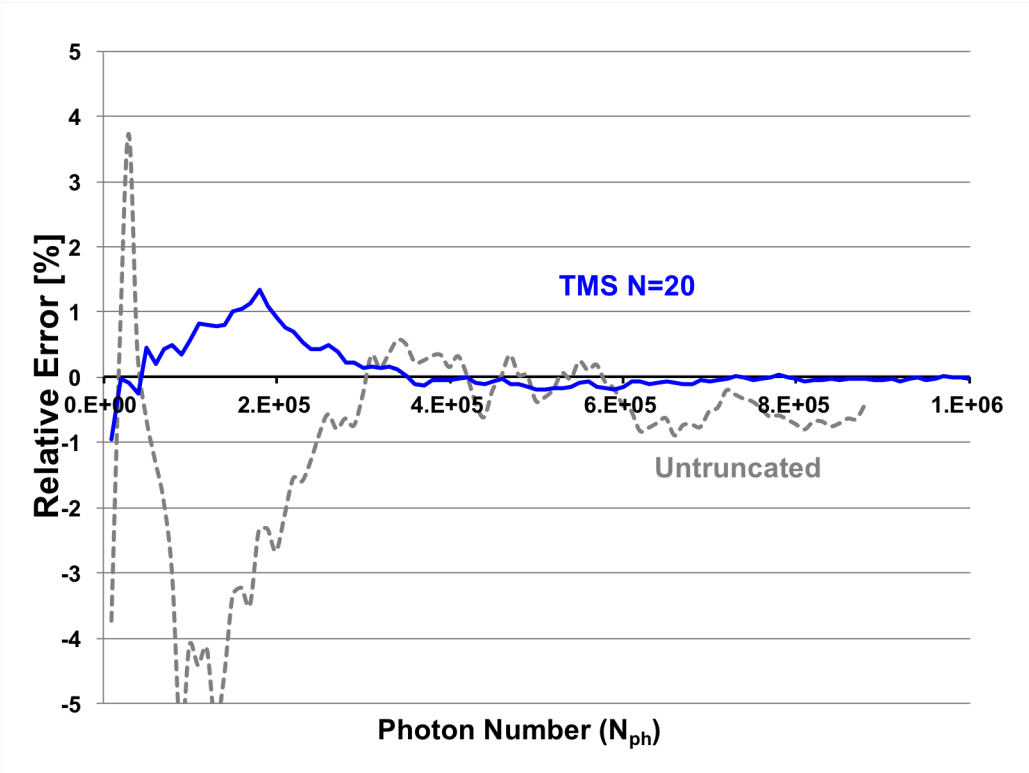

Figure 2.7. Relative errors in the radiance, as a function of photon number N_{ph}, calculated by the backward *MCstar* with TMS-method (N_{qd} = 20) and θ= 60° as shown by solid line and that of a solution without a truncation method by dashed line. Other model conditions are same as in Fig. 2.6.

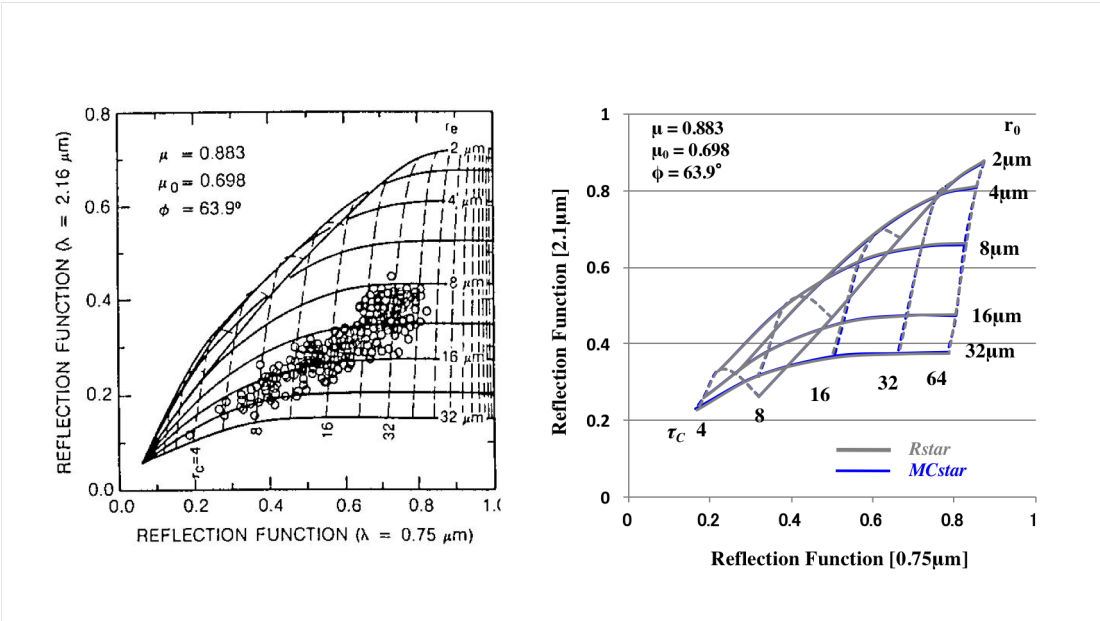

Figure 2.8. Simulation of the solar reflection method for retrieving the cloud optical properties. The left panel is a reproduction of Fig. 2 of Nakajima and King (1991) and the right panel is the results from the backward *MCstar* and *Rstar* for upward radiances at visible ($\lambda=0.75\mu m$) and near infrared wavelength ($\lambda=2.16\mu m$). Solid lines mean radiance values for different r_es with constant COTs and broken lines for different COTs with constant r_es. I assume the angular condition of $\cos\theta = 0.883$, $\cos\theta_0 = 0.698$, and $\phi = 63.9°$, a log-normal cloud particle size distribution with σ=0.35, and total photon number of $N_{ph}=10^7$.

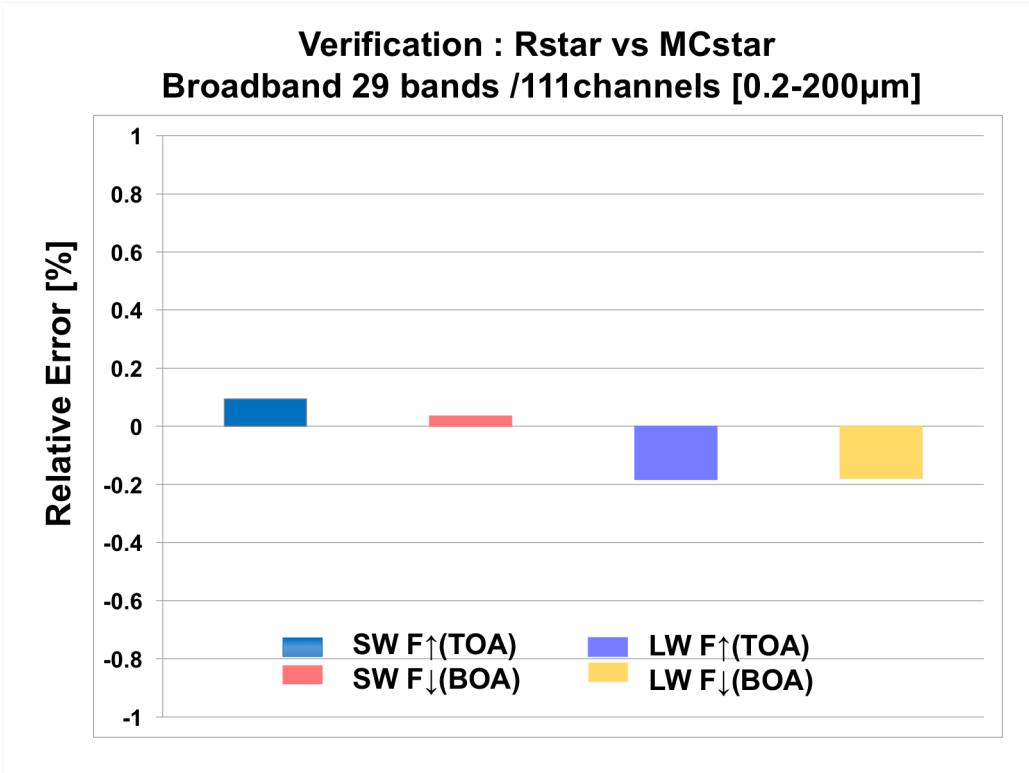

Figure 2.9. Relative errors of broad band radiative fluxes (SW : 0.2~4 μm , LW : 4~50 μm) computed by the 3D Monte-Carlo RT code *(MCstar)* with a 10^9 photons for the atmosphere consisting of 100 × 100 × 20 pixels with a box size of 100km × 100km × 5km relative to values obtained from a 1D RT code *(Rstar)*. The sampling atmosphere is assumed to include a water cloud characterized by r_m= 10 μm, σ= 0.35, τ= 10, and A_g=0. Relative humidity and temperature profiles are of the US standard atmosphere. N_{ph}=10^9 is assumed.

2.3.3 Verification for 3D cloudy atmosphere (Intercomparison of 3D Radiation Code: I3RC)

This section gives a verification of *MCstar* compared with the I3RC experiment result which has already been reported by Cahalan et al. (2005) for 3D cloudy atmospheres. I use the I3RC Cumulus LES of Phase II in Fig 2.10 left panel, Experiment 7. The model domain is 6.67km×6.67km×1.44km and spatial grid scales are Δx, y= 66.7m, and Δz=40m. The TOA is defined at 30km altitude. I assume molecular and aerosol optical parameters as vertically varying and 3D cloud extinction coefficient. Rayleigh phase function and Mie phase function with $r_e=10\mu m$ throughout the cloud field are assumed. Aerosol and cloud SSAs are 0.85 and 0.99, respectively for monochromatic calculation at λ= 0.67μm. A Lambertian surface is assumed with A_g= 0.2. Output is the apparent reflectance at TOA for θ= 0°, θ_0= 60°and ϕ= 0°. The right panel in Fig 2.10 compares the apparent reflectivity results of the I3RC models and the *MCstar*. The figure indicates the *MCstar* result agrees with other results within the model uncertainty of ±0.02.

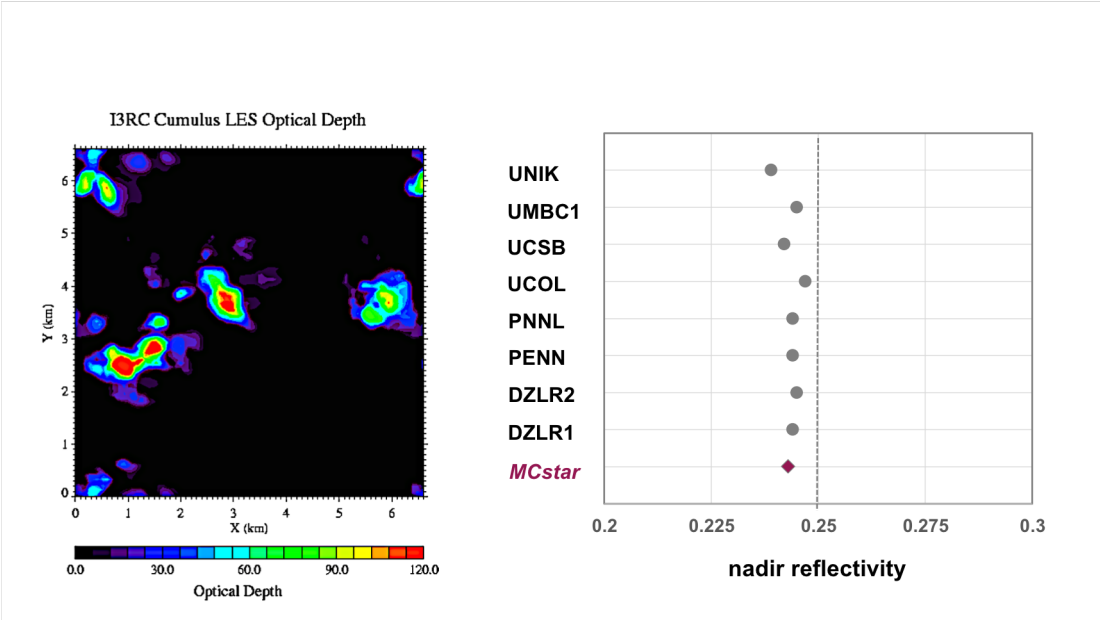

Figure 2.10. The comparison of the *MCstar* apparent reflectivity with those values from I3RC Phase 2 Experiment 7 (Cahalan et al., 2005) at λ= 0.67μm. The sampling area is 6.67km×6.67km×1.44km; Δx,y= 66.7m, Δz=40m with TOA at 30km altitude and Lambertian underlying surface with A_g=0.2. I assume optical parameters of gases and aerosols as vertically varying and 3D cloud extinction coefficient with r_e=*10 μm*. Aerosol and cloud single scattering albedos are 0.85 and 0.99, respectively. Angular conditions of θ=0°, ϕ=0°, and θ_0= 60° are assumed.

Chapter 3.

Satellite-based construction of 3D cloudy atmospheres

In this chapter, I devise a new 3D cloud-construction algorithm called Minimum cloud Information Deviation Method (MIDPM) based on a pixel cloning technique in Section 3.1. Cloud microphysical properties are analyzed using data from CPR/CloudSat and MODIS/Aqua in Section 3.2. I focus only water cloud over the area off south California to construct 3D-cloud filed by MIDPM in this study.

3.1 A 3D cloud field construction algorithm from satellite data: MIDPM

I devise a new method for constructing 3D cloud fields based on available active and passive satellite observations. The method extrapolates the cloud profiles at nadir of CloudSat Field Of View (FOV) into off-nadir regions within the Aqua/MODIS swath based on collocated measurement information of CPR and MODIS both flying as a part of the NASA/A-Train satellite constellation. In other words, a CPR-measured cloud profile is "cloned" to an off-nadir pixel when the two pixels have similar microphysical conditions characterized by MODIS-derived cloud properties. This is based an assumption that vertical cloud profiles would be similar to a pair of imager pixels when key microphysical parameters of the pixels obtained from imager are similar to the microphysical parameters from the orbit each other. The procedure of this method, called Minimum cloud Information Deviation Profiling Method (MIDPM), consists of two steps, i.e. (i) to create a library of collocated CloudSat and MODIS satellite

products and (ii) to fill an off-nadir pixel of MODIS with a radar profile in the library that has MODIS cloud properties best matched to those at the off-nadir pixel.

CPR is a vertically downward oriented radar. The attenuation-corrected equivalent radar reflectivity factor Z is defined as follows,

$$Z = \frac{\lambda^4}{\pi^5 |K|^2} \sigma_b, \tag{3.1}$$

where λ is the measurement wavelength, i.e. 3mm or 95 GHz of the CPR/CloudSat instrument, $|K|^2$ is the refractive index factor for water by the definition of the equivalent radar reflectivity, i.e. $|K|^2$=0.93. σ_b is the backward scattering cross section,

$$\sigma_b = C_{sca} P(\pi), \tag{3.2}$$

where C_{sca} is the scattering cross section and $P(\pi)$ is the backscattering phase function of the scattering air mass. In this definition, the radar reflectivity is corrected by the beam attenuation as given by

$$\exp(-2\tau), \tag{3.3}$$

where τ is the optical thickness of the atmosphere above the scattering air mass at a wavelength of 3mm, which is determined by scattering and absorption of water vapor, clouds and precipitation particles.

It allows the Rayleigh approximation in case of the mono-disperse system of spherical cloud particles because the cloud particle size is smaller than the wavelength. The backscatter cross section is described as follows,

$$\sigma_b \equiv 4\pi\sigma_b' \approx 2^6 \pi^5 \lambda^{-4} r^6 |K|^2 N, \tag{3.4}$$

$$K = \frac{m^2 - 1}{m^2 + 2}. \tag{3.5}$$

where r is the radius and m is the complex refractive index of cloud particles; N is the number of particles in a unit volume. The radar reflectivity factor is conventionally expressed in a unit of [$dBZe$]. It is converted to the value as a unit [mm^6/m^3] as follow.

$$Z[dBZe] = 10\log_{10}\left(Z[mm^6/m^3]\right). \tag{3.6}$$

The vertical resolution of CPR is 250m.

MODIS is a 36-channel general purpose imager that has been developed in the NASA EOS program, which is currently equipped in the Terra satellite and the Aqua satellite. The spatial resolution of the main channels is 1km. In this study, the cloud optical thickness (τ), effective particle radius (r_e) and cloud top temperature (Tc), which are obtained from MODIS sensor.

The CloudSat measurement occurs within 3 minutes after the Aqua satellite overpasses along the same orbital track of A-train at about 13:30 local time. The upper panel in Fig. 3.1 illustrates how the MIDPM algorithm constructs a 3D cloud field by extrapolating a 1D cloud vertical profile to off-nadir locations in a 2D horizontal MODIS imagery. An MODIS RGB image over 2000km×2000km region used to make a library for MIDPM and to construct 3D cloud filed image are also shown in Fig 3.1 bottom panels. This geometry of the two-sensor observations allows us to create a library of collocated satellite products,

$$L\{\{H_{L,k}\}, \{V_{L,k}\} \mid \text{sampled at } k\text{-}th \text{ location along the CloudSat track}\}, \tag{3.7}$$

where L means the library parameter of collocated satellite products, and $\{H_L\}$ and $\{V_L\}$ are MODIS-products and CPR-products, respectively. Barker et al. (2011) adopts MODIS-received radiances at 4 wavelengths at maximum for the H-data and effective radar reflectivity factor $dBZ(z)$ profile for the V-data. Contrary to their approach, I employ MODIS-derived cloud microphysical parameters, i.e. cloud optical thickness (τ), effective particle radius (r_e), cloud top temperature (Tc), for the H-data, instead of radiances. The effective radar reflectivity factor $dBZ(z)$ profiles are prepared from 2B-GEOPROF (Marchand et al., 2008). These cloud parameters (τ, r_e and Tc) used for this purpose have been from 0.65 μm, 2.1 μm, and 11 μm channels of the MODIS

sensor (Nakajima and King, 1990; Nakajima and Nakajima, 1995; Kawamoto et al. 2000). This method is physically straightforward to make 3D-cloud sense to use cloud microphysical parameters. This method is an alternative for selection of the *H*-data. Our choice of using the cloud microphysical parameters, instead of radiances, circumvents the uncertainties arising from effect of different angular geometries and surface conditions on radiances measured, so that I can select a target area for 3D construction wider than the radiance-based method. On the other hand, it should be addressed to include the issue of 1D retrieval error and lack of information contents. The cloud optical thickness (τ), is affected by heterogeneity under the thin optical thickness (Zhang and Platnick, 2011).

I then define a target area within the MODIS image where 3D cloud field is constructed. At every pixel in the target area, the MODIS cloud properties (τ, r_e and Tc) are compared to those in the library to find $\{H\}$ that best matches to those at the pixel. The corresponding cloud profile $\{V\}$ is then assigned to the off-nadir pixel. In this study, I make following selections regarding the size of sampling areas: First, I construct the library using a CloudSat orbital track of l_1= 2000km as shown in Fig. 3.1 bottom left panel; second, sampling areas of l_2 x l_2=100km×100km are selected within l_3= 500km distance from the library track. Spatial resolutions are 1km in a horizontal direction and 250m in the vertical direction as determined by footprint sizes of MODIS and CloudSat. The maximum layer top is set at 5km to restrict the analysis primarily to water clouds. The water cloud is classed by temperature of cloud top > 273K in this study. I select water cloud areas around the CloudSat orbit under the geometrical conditions of l_1 (red line), l_2 (yellow circle) and l_3 (green line) defined in Fig. 3.1 to examine the 3D cloud radiative effects. I selected the values as l_1=2000km, l_2=500km and l_3=100km to find enough many areas from our limited data sets in this study. I selected 500 and 600 samplings as *H* data in Eq. (3.7) for library between 4N and 24N on July 2, 2007 and between 4S and 16N on July 1, 2009, respectively, within l_1=2000km excluding missing values. The "best-matched" cloud conditions according to MODIS parameters $\{H\}$ are defined as those that minimize the deviation described by the following cost function *f*.

$$f(\ell) = \sum_m \frac{<(H_{i,j,m} - H_{L,\ell,m})^2>_{i,j}}{\sigma_m^2}, \quad \sigma_m^2 = <(H_{i,j,m} - <H_{i',j'}>_{i',j'})^2>_{i,j}, \qquad (3.8)$$

where the operation $<H_{i,j,m}>_{i,j}$ means an arithmetic average of *m-th H*-data for all the pixels (*i,j*) included in the sampling area. Similarly $H_{L,l,m}$ stands for the *l-th* library member of *m-th* data. The *H*-data for *m*=1, 2, and 3 respectively correspond to τ, r_e and *Tc*. I select the library member *l* that minimizes the cost function, and adopt $V_{L,l}$ to fill that of the sampling pixel as the most plausible profile. I take the effective radar reflectivity factor profile *dBZ(z)*) for V_L.

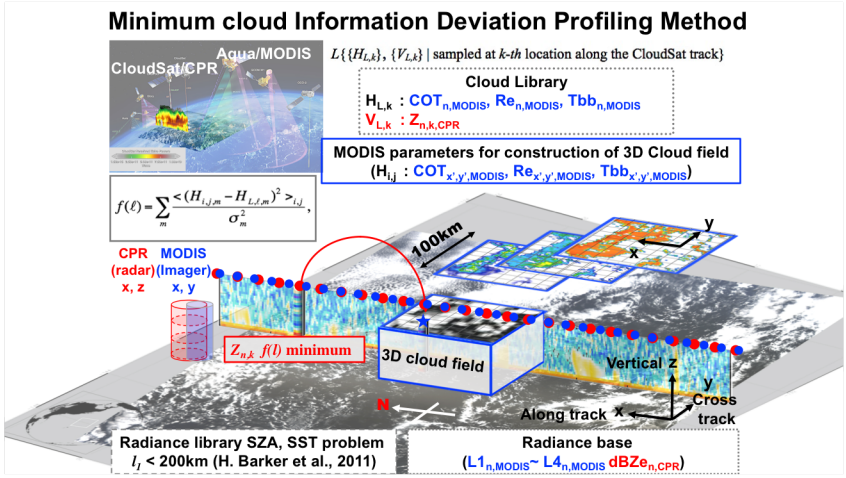

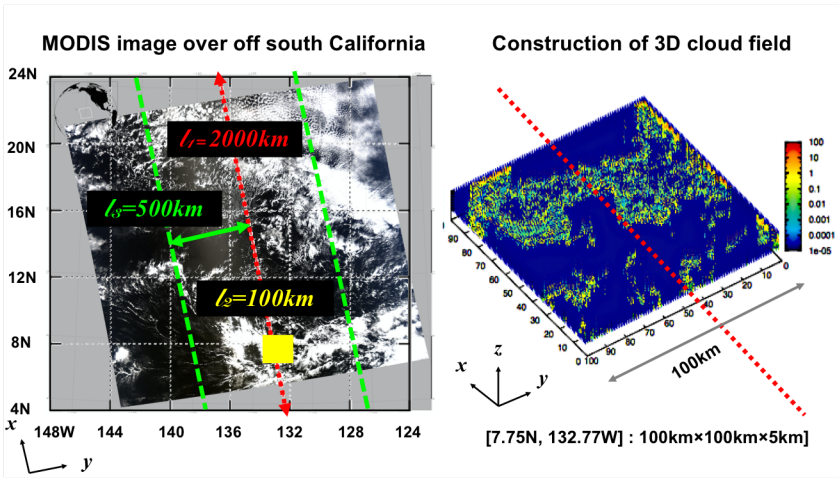

Figure 3.1. Illustration of the MIDPM algorithm of 3D cloud field construction from MODIS/Aqua and CPR/CLODUSAT with collocated orbits. The library for the pair of *H*-data and *V*-data (see texts for their definitions) is constructed by pixels along the orbital track of length l_1= 2000 km as indicated by a red broken line. A sampling area of 100km×100km for 3D field construction is selected as shown by a yellow box. The *H*-data consists of cloud optical thickness (τ), effective radius (r_e), and cloud top temperature (Tc) from MODIS. The *V*-data is defined by the reflectivity factor profile obtained from CPR.

3.2 Assumption for the cloud microphysical properties

For the 3D cloud field thus constructed to be used for RT computation, the radar reflectivity needs to be translated to the extinction coefficient. To simplify this procedure, this study assumes a fixed effective radius and size distribution function for all Monte Carlo boxes in the model domain. For this purpose, I investigate whether CloudSat and MODIS data are consistently characterized by an effective radius chosen for RT computation.

Let us assume the cloud particle size distribution to be a lognormal function as,

$$n_1(x) = \frac{N}{\sqrt{2\pi}\sigma}\exp[\frac{1}{2}(\frac{x - x_m}{\sigma})^2], \tag{3.9}$$

$$x = \ln(r), \quad x_m = \ln(r_m), \tag{3.10}$$

where r is the particle radius, r_m the mode radius, σ the lognormal standard deviation, and N is the total number of particles. The n-th moment of the lognormal size distribution is then given as,

$$r^n n_1(x) = \frac{C_n}{\sqrt{2\pi}\sigma}\exp\left[-\frac{1}{2}\left(\frac{x - x_{mn}}{\sigma}\right)^2\right], \tag{3.11}$$

where

$$C_n = N\exp(x_m n + \frac{1}{2}n^2\sigma^2), \quad x_{mn} = x_m + n\sigma^2, \tag{3.12}$$

$$< r^n > \equiv \int_{-\infty}^{\infty} r^n n_1(x)\,dx = C_n = N\exp(x_m n + \frac{1}{2}n^2\sigma^2). \tag{3.13}$$

These formulae relate the satellite cloud observables, τ, r_e and the liquid water path LWP, with the size distribution parameters, r_m and σ, as follows in case of a vertically-invariant homogeneous cloud layer,

$$\tau = H\int_{-\infty}^{\infty} Q_{ext}(\alpha)\pi r^2 n_1(x)\,dx \approx 2\pi NHexp(2x_m + 2\sigma^2), \tag{3.14}$$

$$LWP = \frac{4\pi\rho H}{3}\int_{-\infty}^{\infty} r^3 n_1(x)\,dx \approx \frac{4\pi\rho NH}{3}\exp(3x_m + \frac{9}{2}\sigma^2), \tag{3.15}$$

$$r_e = \frac{< r^3 >}{< r^2 >} = \frac{3LWP}{2\rho\tau}\exp(x_m + \frac{5}{2}\sigma^2), \tag{3.16}$$

where H is the cloud geometric thickness; Q_{ext} is the efficiency factor for light extinction which is approximated by 2 for the SW spectral region, and ρ is the water density. The effective radar reflectivity Z is expressed as,

$$Z = \int_{-\infty}^{\infty} (2r)^6 n_1(x)\,dx = 2^6 < r^6 >= 2^6 \times 10^{12} N\exp(6x_m + 18\sigma^2). \tag{3.17}$$

It follows from Eqs. (3.14) and (3.17) that

$$\frac{ZH}{\tau} = \frac{2^6 \times 10^{12}}{2\pi}\exp(4x_m + 16\sigma^2). \tag{3.18}$$

I rewrite Eq. (3.18) as follows,

$$\frac{ZH}{\tau} = X \cdot r_e, \tag{3.19a}$$

$$X = \frac{2^6 \times 10^{12}}{2\pi}\exp(3x_m + \frac{27}{2}\sigma^2). \tag{3.19b}$$

This relation Eq. (3.19a, b) enables us to retrieve the effective radius (r_e) from τ from MODIS and Z from CPR (Stephens et al., 1990) when assuming a homogeneous cloud layer. Given that the relation is a weak function of σ, I assume a tentative value of

σ = 0.35 in this study. This connects τ and ZH directly through x_m and thus through r_e. The scatter plot between τ and ZH is shown in panel (a) of Fig. 3.2 for various values of the layer-mean r_e as depicted in diagonal lines. The figure indicates that most data of MODIS visible radiance and CPR reflectivity are consistent with each other if the layer-mean r_e are between 7μm to 25μm. I also plot in panel (b) the layer-mean $r_{e\,\mathrm{CPR}}$ calculated by Eq. (3.19a, b) with those of the H-library, i.e. $r_{e\,\mathrm{MODIS}}$ retrieved from MODIS visible and near-infrared wavelengths by the solar reflectance method of Nakajima and Nakajima (1995). The panel (b) also shows that the two estimates of r_e also exist in the range of 7μm to 25μm with accuracy. This analysis concludes that a representative r_e for *MCstar* calculations should be r_e = 13μm as the logarithmic mean value for the scenes analyzed in this study. One future work should be an investigation the relation between $r_{e\,\mathrm{CPR}}$ and $r_{e\,\mathrm{MODIS}}$ in terms of vertical inhomogeneity of the cloud microphysical condition, because the former value is a layer mean value, while the latter corresponds to r_e near cloud top.

The cloud effective reflectivity is then converted to the extinction coefficient profile, i.e. $e_{i,j,k}$, for 3D-RT calculation as follows (Smith, 1984),

$$Z_{i,j,k} = 10^{dBZ_{i,j,k}/10}, \tag{3.20}$$

$$e_{i,j,k} = \frac{Z_{i,j,k}}{\sum_{k=1}^{n} Z_{i,j,k}} \cdot \frac{\tau_{i,j}}{\Delta z}, \tag{3.21}$$

where Δz is the CPR echo vertical resolution, i.e. 250m, τ_{ij} the total column optical thickness of the atmosphere retrieved from MODIS, and Z_{ijk} the effective radar reflectivity for a *k-th* layer of a pixel (*i,j*) in the model domain.

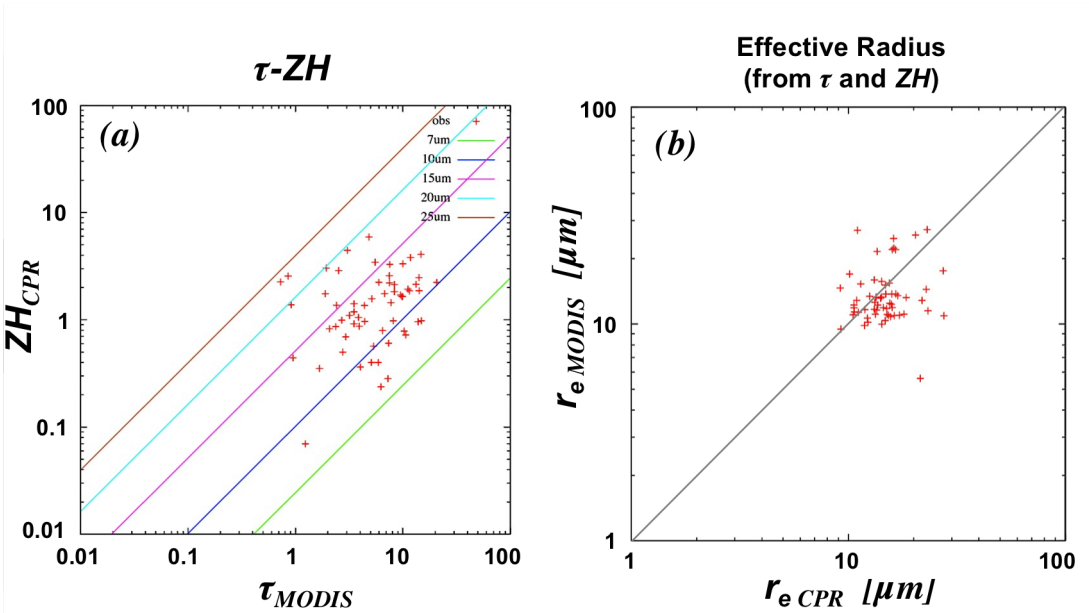

Figure 3.2. (a) Scatter plot between the column-integrated effective reflectivity, *ZH*, from CPR and τ from MODIS. Solid lines superimposed indicate the approximate relation given by Eq. (3.19a, b) for various r_e values. (b) Scatterplot between two r_e values derived from Eq. (3.14) and Eq. (3.17).

Chapter 4

Assessment of radiative effects in 3D idealized cloudy atmospheres

4. 1 Evaluation of plane parallel approximations to 3D radiative effects

Before analysis of the observed data, I compare the solar radiative flux simulated by the *MCstar* with those by several plane parallel approximations for idealized cloud systems to identify various 3D-CRE in this section. Such comparison for idealized clouds serve as a clue to understand plane parallel approximation errors characteristic to each of satellite-based 3D cloud cases shown in the next chapter. In this simple investigation, I perform monochromatic RT calculations at a wavelength of 550nm at which I can ignore light absorption by atmospheric constituents. In this non-absorptive condition, I can discuss only the reflectivity at TOA to evaluate the discrepancies of each approximation from the 3D simulation, because the error at BOA has the same magnitude but with opposite sign by the radiative energy conservation law.

In this study, I investigate three existing approximations, i.e. (i) Plane Parallel Approximation (PPA), (ii) Independent Column/Pixel Approximation (ICA/IPA) and (iii) Tilted Independent Pixel Approximation (TIPA) against 3D simulations. I show a schematic illustration of these approximations in Fig 4.1. The PPA is the simplest approximation in which the 3D extinction field is averaged over the model domain to make a vertically inhomogeneous 1D cloud column. RT calculations with a 1D-RT code are then applied to this 1D column to obtain the radiative flux f_{PPA},

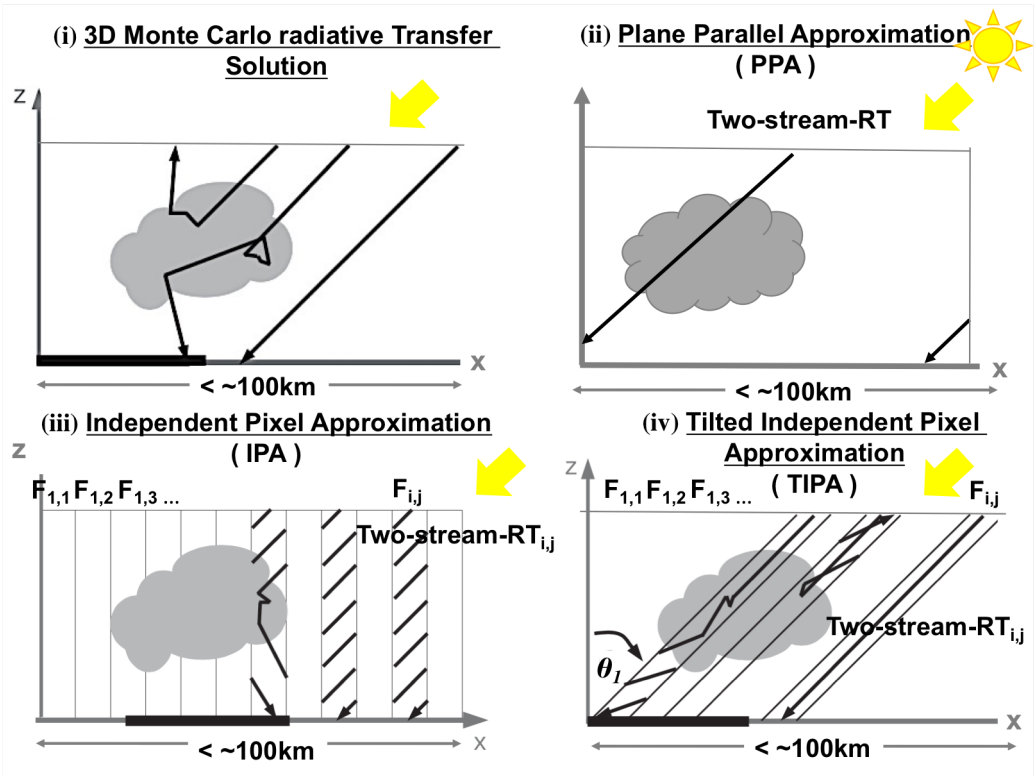

Figure 4.1. Schematic illustration of (i) 3D Monte Carlo radiative transfer simulation, (ii) Plane Parallel Approximation (PPA), (iii) Independent Column/Pixel Approximation (ICA/IPA) and (iv) Tilted Independent Pixel Approximation (TIPA)

$$F_{PPA} = f_{PPA}(<\tau_{i,j}>, \mu_0, \phi_0), \tag{4.1}$$

where $\mu_0 = \cos\theta_0$ and ϕ_0 are the cosine of solar zenith angle θ_0 and azimuthal angle; $\tau_{i,j}$ is the optical thickness of the atmosphere at the pixel (i,j). The azimuthal angle is measured from local east. The operation $<\tau_{i,j}>$ means horizontal averaging of optical thicknesses for all the pixels in the model domain. F_{PPA} stands for the 1D-RT operator, which is applied to the horizontally averaged field.

Another approximation, called the Independent Column/Pixel Approximation (ICA/IPA) (Stephens et al., 1991; Cahalan et al., 1994), assumes a plane parallel atmosphere at each pixel within the model domain. This approximation applies the 1D-RT operator to each column/pixel in the model domain to obtain the area mean radiative flux as,

$$F_{IPA} = <f_{PPA}(\tau_{i,j}, \mu_0, \phi_0)>_{i,j}. \tag{4.2}$$

In ICA/IPA approaches, the radiative transfer calculations are performed in single, vertical columns with a 1D-RT solver, assuming horizontally homogeneous, infinitely extended model layers. The ICA/IPA method does not account for typical three dimensional phenomena, however, thus leading to following errors (Marshak and Davis, 2005).

1) The misplacement of direct radiation error derived from that the shadow of the cloud erroneously falls under the cloud and is neither shifted nor elongated if the sun is not in the zenith.

2) The misplacement of diffuse radiation error derived from that there is no photon scattering into neighboring columns, thus ICA/IPA does not account for the inter-column photon transport that would lead to radiative smoothing or roughing.

3) A bias of direct radiation, that in cloud free columns, i.e. clear sky region, the direct radiation easily reaches the surface in the ICA/IPA approximation. ICA/IPA tends to overestimate direct radiation at the surface because the direct radiation for larger solar zenith angles is intercepted by clouds.

4) A bias of diffuse radiation derived by missing inter-column photon transport between cloudy and cloud free columns.

Through several case studies, I find that the error behavior of PPA and IPA as a function of Solar Zenith Angle (SZA) for the reflected SW flux is qualitatively understood by three simple cloud geometries, i.e. Types A, B, and C. Type-A assumes roll-bar type blocks of clouds with τ_c= 50, width W_1= 4km, and cloud top and bottom heights z_{t1}= 3km and z_{b1}= 0km, separated by clear sky areas with width W_2= 6km. The area-averaged cloud fraction (CF) is 0.4 and the area-mean $<\tau_c>$=20. In Type-B, the clear areas in Type-A are filled by low-clouds of τ_c=15 with cloud top and bottom heights of z_{t2}= 1km and z_{b2}= 0km. I show the cloud configuration of Type-B in Fig 4.2. In Type-C, those "filling" clouds are located to have the same cloud top height as adjacent clouds, i.e. z_{t2}= 3km and z_{b2}= 2km. I also assume the blocks of high-clouds with τ_c=50. The area mean COT is $< \tau_c >$=29 in Type-B and -C. The solar azimuth is set to be in the xz-plane in Fig. 4.3.

Figure 4.3 shows errors of the solar flux at 550 nm obtained from existing approximations relative to the 3D calculation as a function of SZA. Fig. 4.3(a) compares the errors for Type-A clouds. It is shown that PPA always overestimates the reflected solar flux because of stronger multiple scattering by one single plane parallel layer than that of finite clouds in the 3D case for the same $< \tau_c >$. On the other hand, IPA accurately simulates the 3D fluxes for normal incidence, θ_0= 0°, because Eq. (4.1) takes into account the small upward flux in the clear sky region. IPA, however, underestimates the flux compared to the 3D values in large SZA cases. This is because the clear sky areas become more obscured for the slant insolation in the 3D condition, whereas IPA always includes the small clear sky flux in computation through Eq. (4.1). IPA error is especially caused by above 3) and 4) biases in Type-A. IPA, nonetheless, does not break down significantly because the underestimation of the area-mean reflectivity due to the clear sky inclusion tends to be cancelled in part by the overestimation due to the plane parallel cloud reflectivity in the cloudy parts (Cahalan et al, 1994).

The clear sky obscuring effect, however, disappears when the clear sky area is replaced by low-height thin clouds as in the case of Type-B, or upper cloud-roughened type, as shown in Fig 4.3(b). I assume τ_c= 50 for geometrically thick (3km) clouds and

τ_c=15 for thin clouds (1km). In this case, PPA always overestimates for the reflected solar flux in a manner like the case of Type-A. Although much smaller than the PPA errors, IPA also tends to overestimate for the reflectivity over the entire SZA range as shown here including larger SZA cases where IPA underestimates for the reflectivity in Type-A (Fig. 4.3(a)). This persistent overestimation of IPA for Type-B, contrary to Type-A, can be understood as follows. IPA error is caused mainly by above 1) and 2) in Type-B. In the real 3D cloud case, the low-clouds reflect photons emerging from lateral sides of the adjacent high-clouds in addition to photons directly incident upon the low-clouds. The reflected photons by low-clouds, however, are difficult to emerge from TOA due to blocking by the high-clouds, because emerging angles of photons are widely distributed in the hemisphere because of multiple scattering by the cloud layer. Therefore, this high-cloud blocking effect makes the 3D flux smaller than those by IPA, which fails to represent this blocking effect. This effect becomes more significant for larger SZAs. IPA error dependency on SZA particularly occurs around θ_0=30° as a minimum error for Type-B under the condition of both the geometrical cloud height, i.e. z_{t1}-z_{b1}=3km, and the distance between two clouds, i.e. W_2=6km in this study. IPA error is especially affected by the distance between adjacent clouds. The high-cloud blocking effect appears under the condition that the distance between clouds, i.e. W_2, is enough as long as the high-cloud height, i.e. z_{t1}-z_{b1}. If the height of high-cloud, i.e. z_{t1}-z_{b1} is significantly tall against the distance between clouds, i.e. W_2, the cloud side illumination/shadowing effect more distinguishes than the high-cloud blocking effect in reality. IPA is, therefore, not so different against 3D-RT simulation under such condition. In this study, the IPA minimum error appears around θ_0=30° in Type-B because illumination, shadowing and high cloud blocking effects are almost canceled each other. The clarification of the high-cloud blocking effect is very important because it is one of a key error as an uncertainty of 3D-CRE in large cloud fraction filed.

This interpretation is supported by the fact that the effect becomes less dependent on SZA when the low-level clouds are elevated so as to have the same top height as adjacent high-clouds as in the case of Type-C, or lower cloud-roughened type (Fig. 4.3(c)). In this case, PPA again overestimates the reflectivity by the same reason as in Type-A and -B. In the 3D-RT simulation for Type-C, the incident solar radiation at the cloud top tends to be injected toward the BOA more effectively than the PPA case through the thick clouds extended below the bottom of the thin clouds. This penetrated

radiation at the BOA is difficult to emerge from TOA because of the blocking effect of high-clouds, which is similar mechanism in Type-B. This phenomenon, however, does not depend too much on the value of SZA because the cloud-top surface texture, felt by incoming solar ray in Type-C clouds, is more homogeneous, which is qualitatively different from the inhomogeneous texture in Type-B. These amounts of error depend on optical thickness and their variations. IPA error is caused by above 3) and 4) biases in Type-C. The 3D-RTE of Type-C is so call light guide effect. It is also one of a crucial effect for 3D-RTE, for example multilayer cloud including large uncertainties as both the high-cloud blocking and light guide effect.

In order to take into account for the evident clear sky obscuring effect of Type-A; an idea called the Tilted Independent Approximation (TIPA) has been proposed by Varnai and Davies (1998). This approximation assumes a slant path optical thickness for the *k*-th layer defined as,

$$\tau_{slant,i,j}(\mu_1,\phi_1) = \mu_1 \int_{z_{bottom}}^{z_{top}} e(x,y,z)\frac{dz}{\mu_1}, \quad \mu_1 = \cos\theta_1 \ , \tag{4.3}$$

$$x = x_i + (z - z_k)\sin\theta_1\cos\phi_1, \quad y = y_j + (z - z_k)\sin\theta_1\sin\phi_1, \tag{4.4}$$

where θ_1 and ϕ_1 are zenith and azimuthal angles for the insolation ray at pixel (i, j); (x_i, y_j) is the center coordinates of the pixel column. Then 1D-RT calculation is applied to all the pixels in the same manner as in IPA as

$$F_{slant} = < f_{PPA}(\tau_{slant,i,j}(\mu_1,\phi_1),\mu_0,\phi_0) >_{i,j} . \tag{4.5}$$

The idea of TIPA assumes the direct solar ray for insolation in Eq. (4.5), i.e. (μ_1, ϕ_1) = (μ_0, ϕ_0). In this formulation, the IPA is a special case of normal insolation, i.e. $\mu_1 = 1$. In the present study, I apply the "TIPA" to calculate the solar fluxes for varying SZAs to assess the error of TIPA against 3D-simulations, which is used as an index for the diffuse radiative transport effect between tilted neighboring columns.

The TIPA attempts to take into account the clear sky obscuring effect and illumination/shadowing effects of lateral sides of the cloud box. Figure 4.3 also shows the errors of TIPA against 3D-RT simulations, indicating that the TIPA constantly produces relatively small overcorrections regardless of the cloud type and SZA. This

indicates that TIPA successfully corrects the negative bias caused by IPA for the clear sky obscuring effect. It is, however, important to note that the error is positive in most cases, indicating that the effect is overcorrected in the case of Type-A as much as 20 Wm^{-2} (Fig. 4.3(a)). TIPA also tends to overcorrect particularly for large SZAs in Type-B (Fig. 4.3(b)). These phenomena suggest that the positive error is derived from the fact that the reflection is overestimated in the clear sky region that contains angular components different from that of the direct solar ray, as also pointed out by the series of past studies regarding TIPA and their derivatives. Although TIPA can eliminate the error made with ICA/IPA, it does not account for the diffuse radiation transport between the tilted columns since TIPA is still a 1D-RT approach. In this study, the minimum TIPA error occurs around θ_0=30° for Type-B under the condition of the high-cloud height z and the distance between clouds W because the diffuse radiation in each columns made from θ_1=30° can be canceled in Type-B. TIPA error, however, increase for large SZAs except for θ_0=30° since the light is more scattered in deep cloud area and affects neighboring columns as diffuse radiation for large SZAs. In Type-C, overcorrection of TIPA and its SZA dependence are smaller than Type-B case, but is still larger than IPA case (Fig. 4.3(c)). This means the fact that the reflectivity behavior at the cloud-top is more homogeneous with increasing SZA because cloud top is same for all columns in Type-C clouds.

The overall characteristics shown in Fig. 4.3 thus illustrate how key errors of PPA, IPA and TIPA change their magnitudes and dependences on SZA in a manner that systematically varies with cloud horizontal and vertical morphology.

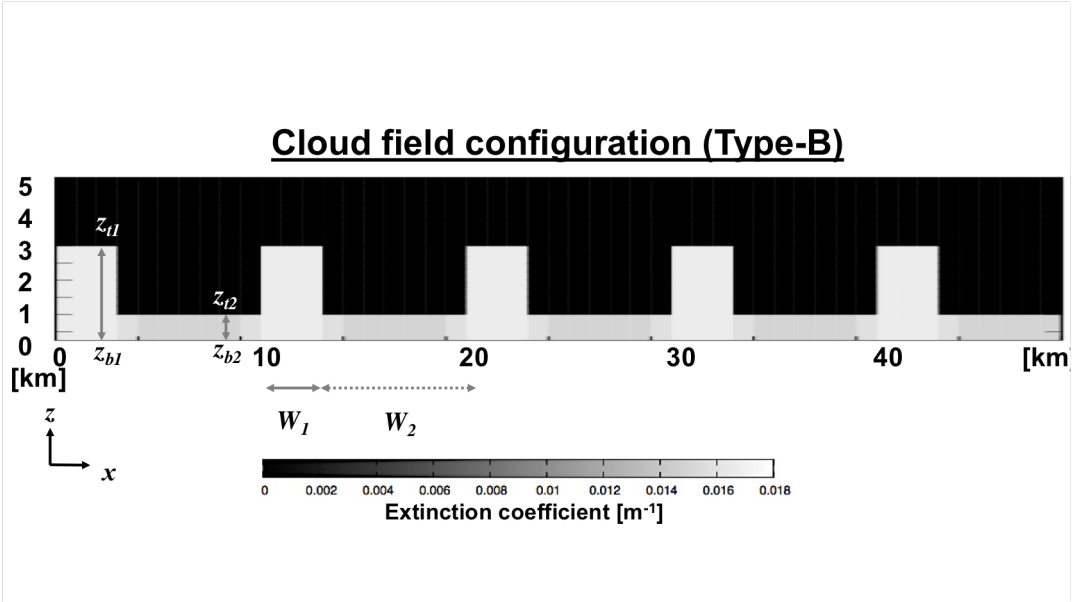

Figure 4.2. Cloud configuration in Type-B.

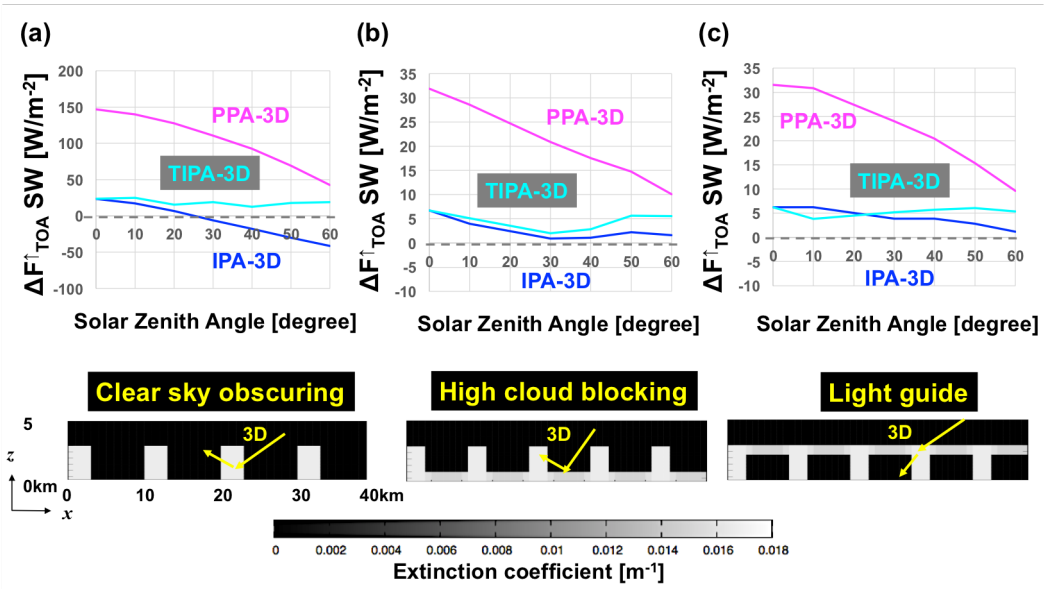

Figure 4.3. Error characteristics of various plane parallel approximations (PPA, IPA, TIPA) in reflected solar radiative fluxes at TOA relative to 3D Monte-Carlo computations illustrated for three different idealized cloud systems: Type-A, B and C in panels a, b and c, respectively. In each panel, vertical views of the cloud morphology are shown as xz-sections of the extinction coefficient in bottom columns. See text for details of assumptions and settings of three cloud types.

4.2 New approximation: Slant path Independent Pixel Approximation (SIPA)

Although the TIPA method can eliminate the error arising from IPA, they do not account for dominance of diffuse radiation with increasing optical depth in the tilted column construction, and also for effect of interaction with neighboring columns. As for inclusion of diffuse radiation effect, two different types of TIPA have been suggested. In the first TIPA approach that I call "TIPA-D", i.e. tilted independent pixel approximation for direct radiation, the direct radiation is calculated in the independent column that is slanted toward sun according to the solar zenith and azimuth angles (μ_0, ϕ_0), while the diffuse radiation is calculated in the vertical column having the direct radiation field as input. This method has been developed for two dimensions by Gabriel and Evans (1996), who called it "Independent Pixel Approximation Modified Source (IPAMS)". In the second approach, both the direct and the diffuse radiations are calculated in the tilted independent columns according to slanted solar zenith and azimuth angles (θ_0, ϕ_0). This method, called Tilted Independent Pixel Approximation for direct and diffuse radiation or I just call it "TIPA", was developed by Varnai and Davies (1999). As for inclusion of neighboring column effect, "Nonlocal Independent Column Approximation (NICA)" has been introduced by Marshak et al., (1995). NICA is based on the result of ICA and form a convolution product for each column. Marshak et al. (1995) used a gamma distribution as convolution kernel. Zuidema and Evans (1998) employed a Gaussian distribution and convolved the TICA reflectance, thus called "NTICA". However, these methods need to employ full 3D-simulations to determine the best convolution. Wissmeier et al. (2013) devised the parameterized NTICA, or "paNTICA", for surface irradiance. This is based on TICA with smoothing kernel as convolution including cosine of solar zenith angle and the distance between ground and the cloud base height without 3D-simulations.

Compared to these elaborated methods, I try a simpler method to mitigate the TIPA overcorrection using a concept of Virtual Solar Zenith Angle (VSZA) in the TIPA scheme. The error characteristics of "TIPA" found in Fig. 4.3, particularly in Type-A, imply that the overcorrection could be eliminated when the insolation zenith angle μ_1 in Eq. (4.5) is assumed to be somewhat different from the actual SZA so as to take into account the effect of diffuse lights. This "optimum" insolation zenith angle θ_1, which I refer to as VSZA, can be determined by trial and error based on 3D-RT simulations. I suggest a new TIPA-type approach that I call Slant path Independent Pixel Approximation (SIPA) to use the VSZA in Fig 4.4. The idea of SIPA assumes the insolation angle θ_1 for tilted column construction different from that of direct solar radiation in Eq. (4.5), i.e. $\theta_1 \neq \theta_0$. I call then θ_1 VSZA.

Figure 4.5 shows SIPA examination results with various VSZAs as θ_1= 10°, 20°, 30°, 40°, 50° for the case of Type-A, -B and -C clouds (Fig. 4.5(a), (b), (c)). It is found from the figure that SIPA with θ_1=10° provides too much under-correction with large SZA in the case of Type-A in Fig 4.5(a). On the other hand, SIPA is more accurate at around θ_0=20° with θ_1=10°. All VSZA cases are also accurate when the VSZA is smaller than SZA, i.e. $\theta_1 < \theta_0$ in Type-A. For Type-B, SIPA tends to produce similar reflectivity between θ_1=10°~50°. All VSZA values tend to mitigate the overcorrection of TIPA when $\theta_1 < \theta_0$. This mitigation also occurs in Type-C, suggesting that SIPA has an effect of reducing errors of TIPA when $\theta_1 < \theta_0$. As a result, it is concluded that SIPA gets an optimum flux if VSZA is about 10° smaller than SZA, i.e.

$$\theta_1 = \theta_0\text{-}10° \text{ for } \theta_0 \geq 10° \text{ and } \theta_1 = 0° \text{ for } \theta_0 < 10°, \qquad (4.6)$$

although this is just a semi-empirical rule. Fig 4.5 shows that the magnitude of the SIPA error with this selection of θ_1 becomes smaller than those of IPA and TIPA in the case of Type-A cloud because this correction simultaneously reduces the IPA error associated with clear sky obscuring effect and the TIPA error associated with horizontal diffusion effect in each pixel. SIPA is most accurate assuming $\theta_1 = \theta_0$-10° under the condition that the distance of clear sky region, i.e. W_2, is enough as long as the isolated cloud height, i.e. z_{t1}-z_{b1} in Type-A in Fig 4.5 (a) with red line in this study. IPA and TIPA are similar to 3D-RT simulation as the distance between clouds, i.e. W_2, becomes narrow because the cloud field, felt by incoming solar radiation, is more homogeneous.

In case of Type-B and -C, the results are more similar to those of IPA and TIPA because the clear sky obscuring effect does not exist, although there is a slight error reduction for large SZAs. SIPA also remains the error as the diffuse radiation in neighboring column in Type-B and C in Fig 4.5 (b, c). These types are implicated to adjust VSZA because it would be necessary to use more factors related to cloud optical parameter like Wissmeier et al. (2013) devised the "paNTICA" by using the distance between ground surface and cloud base to estimate surface solar irradiance.

A simple assumption of θ_1 =30° works within our test cases if I do not need a high accuracy. The SIPA might be a convenient solution for large volume data analysis because it is difficult for analyzer to select the optimal 1D approximation for each cloud case, though it might not be so superior as compared to other existing TIPA derivatives. It is also worth noting that these optimal VSZA values is smaller than the value of 54.7°, corresponding to $\mu_1 = 1/\sqrt{3}$ suggested by the traditional two stream Gaussian approximation for the completely diffuse case.

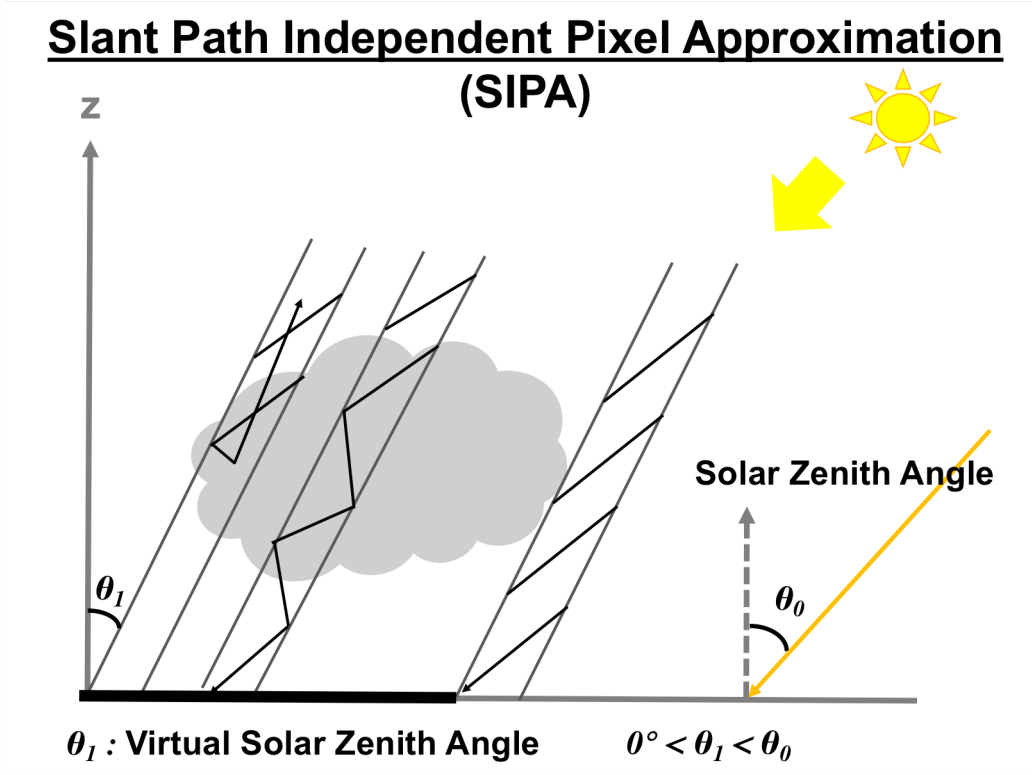

Figure 4.4. Schematic illustration of Slant path Independent Pixel Approximation (SIPA).

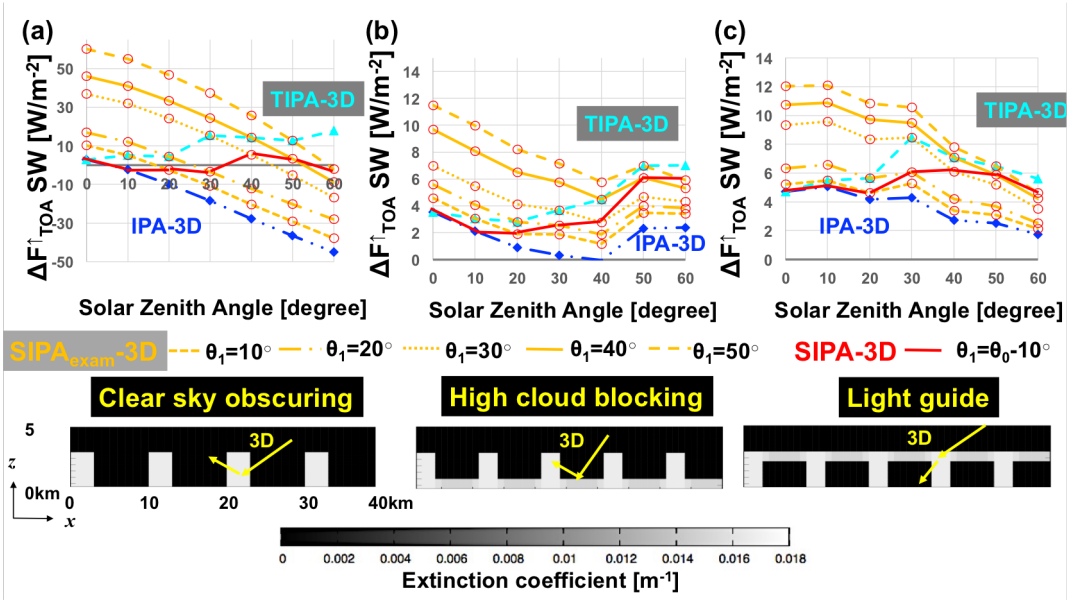

Figure 4.5. Error characteristics of various plane parallel approximations (IPA, TIPA and SIPA) in the reflected solar radiative flux at TOA relative to 3D Monte-Carlo computations for three idealized cloud systems, Type-A, B and C, and for various VSZA values, i.e. θ_1= 10°, 20°, 30°, 40°, and 50° for the SIPA solution Eq. (4.5).

Chapter 5

Assessment of radiative effects in 3D observed "real" cloudy atmospheres

In this chapter, I construct 3D cloud fields by the MIDPM introduced in Chapter 3 using the actual satellite data, i.e. CloudSat/CPR and Aqua/MODIS data. I intend a study only for water clouds in summer season off the coast of California. Further I simulate 3D radiative transfer in the constructed model domains using the *MCstar* developed in Chapter 2, and study the cloud radiative effects (CRE) in SW and LW upward and downward fluxes at TOA and BOA.

5.1 Simulation and validation of 3D radiation fields constructed by MIDPM and *MCstar*

Before detailed investigation of the realistic 3D-CRE, I perform a validation study to see whether the MIDPM clouds suitably reflect the key features of the observed cloud structure by a comparison between the broadband solar (SW) flux obtained from CERES and the flux simulated by *MCstar* in MIDPM domain. For this purpose, I choose a 20km×20km area of a footprint of CERES as a sampling area in Fig 5.1. I decide an altitude of 30 km as TOA and calculate the TOA radiative flux. I construct the 3D cloud field by MIDPM. Surface albedo are prepared from the CERES/CCCM product. Profiles of temperature, pressure, water vapor content, and ozone amount of each vertical atmospheric layer are also given from the CCCM data. I use other gas parameters of the US standard atmosphere in the *Rstar* code database. I sampled 23 cases from July 2, 2007 through July 1, 2009 in ocean are off Californian coast. Aerosols are neglected.

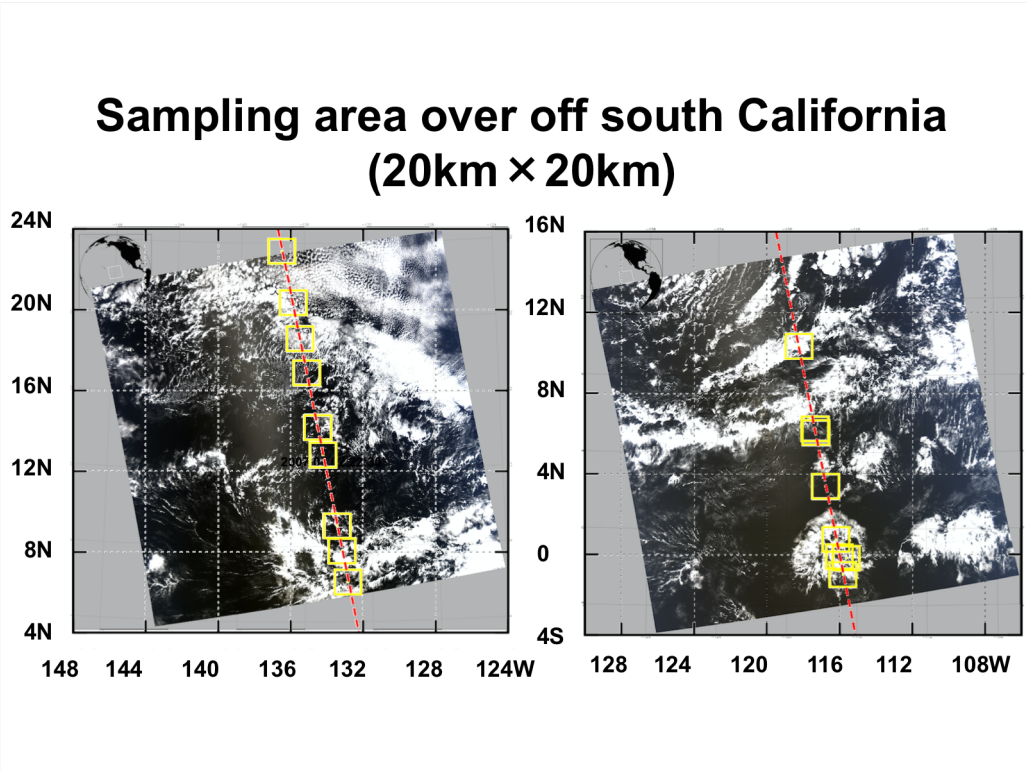

Figure 5.1. Sampling areas for constructing 3D cloud fields within a MODIS imagery for validation with CERES data on July 2 22:30, 2007 in left panel and on July 1 21:30, 2009 in right panel, respectively.

Figure 5.2 shows cases of minimum and maximum differences of the simulated flux from CERES-observed flux. It is found from the figure that our estimates of the SW flux agree with CERES values within less than 8 ~ 50 $Wm^{-2.}$ The large bias, however, arises primarily from large cloud fraction field case including a lot of thin cloudiness. One of this reason is inferred the issue of 1D retrieval error. The cloud optical thickness could be overestimated, for example, because the 1D retrieval data, i.e. cloud optical thickness (τ), is affected by heterogeneity under the thin optical thickness (Zhang and Platnick. 2011).

The instantaneous error of the TOA flux of CERES itself has been reported about $9Wm^{-2}$ (Su et al., 2015), therefore, I think the errors shown in Fig. 5.2 does not suggest the MIDPM is not suitable as a 3D construction method, though I need a future study of validation with more data in various conditions. What is considered as an error factor of MIDPM are 1) the error of cloud radar and imager retrievals and 2) the error in the cloning process by MIDPM as follows. First, the footprint is different between CloudSat/CPR and Aqua/MODIS, i.e. 2km and 1km respectively; hence it is possible to exist several matching pairs in the library. I also should have a future study of the method of the library construction. In this study, I selected simply the closest library member when I compare the data of MODIS at off-nadir pixel and cloud library, but in fact there is possibility that I can choose several other library members depending on setting the distance of l_1, l_2, and l_3 as shown in Fig 3.1. I like to find out their impact in the future. The algorithm of 3D cloud construction by Barker (2011, 2012) adopts radiances as *H*-data in MIDPM, which is, as indicated in their papers, affected by difference in the solar zenith angle; therefore, the construction of libraries area is limited to ℓ_1 < ~200km. However, in this study, the construction method with cloud microphysical parameters (τ, r_e and *Tc*) allow us to increase the ℓ_1 , but I need to study in future to find a suitable length for making the library. In this study, I select water clouds by *Tc* > 273K as a reference, but ice clouds must be handled for validation of the global cloud.

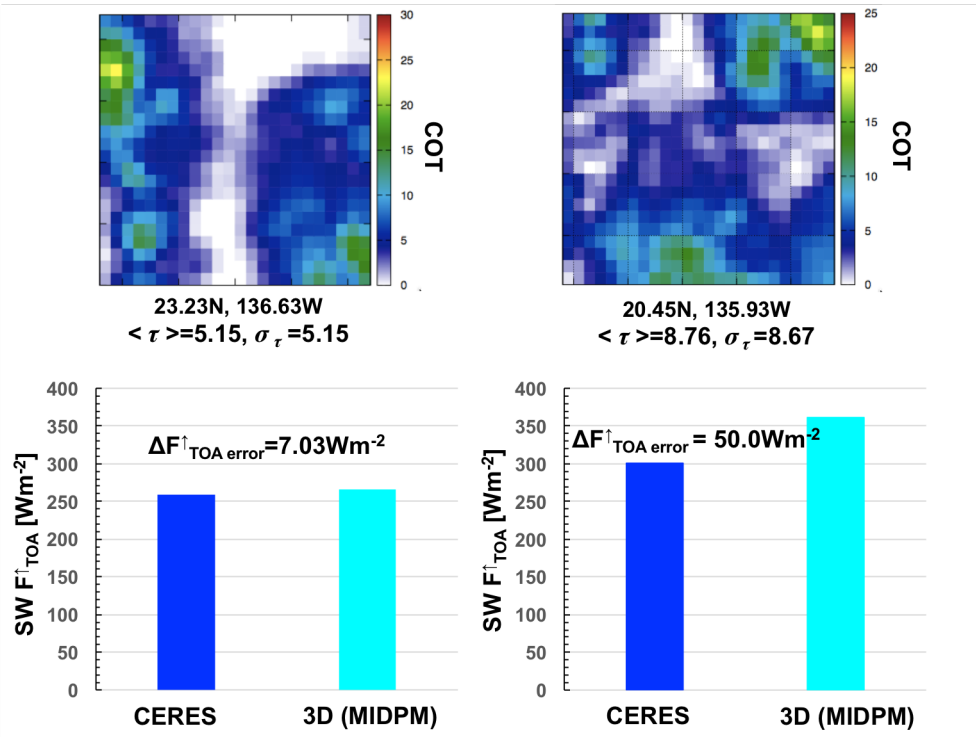

Figure 5.2. Comparison of *MCstar* simulated and CERES-observed broadband SW fluxes for a 20km×20km area of a footprint of CERES. The lower left panel shows the case of the minimum difference 7.03Wm^{-2} for the cloud field shown in the upper left panel with $<\tau>$= 5.15 and σ_τ= 5.15. The lower right panel shows the case of the maximum error 50Wm^{-2} with $<\tau>$= 8.76 and σ_τ=8.67.

5.2 Analysis of 3D cloud radiative effects by the broad-band fluxes.

In this section, I study the 3D-CRE for 15 cloud systems constructed by MIDPM using CLOUDSAT/CPR and AQUA/MODIS data. Sampling areas are taken from the ocean area off Californian coast on July 2, 2007 and on July 1, 2009 as shown in Fig. 5.3. Tables 2 and 3 list the sampling data information of these two cloud scenes, respectively. I select these sampling areas with domain size of 100km×100km from regions of not only the A-Train nadir including CERES FOV but also off-nadir areas distant within 500km from the A-Train track. For this analysis, the MIDPM library is constructed from the MODIS imagery extending 2000km in length. Broad-band SW and LW RT calculations are performed by the *MCstar* and *Rstar*. I pick up three characteristic results for detailed study.

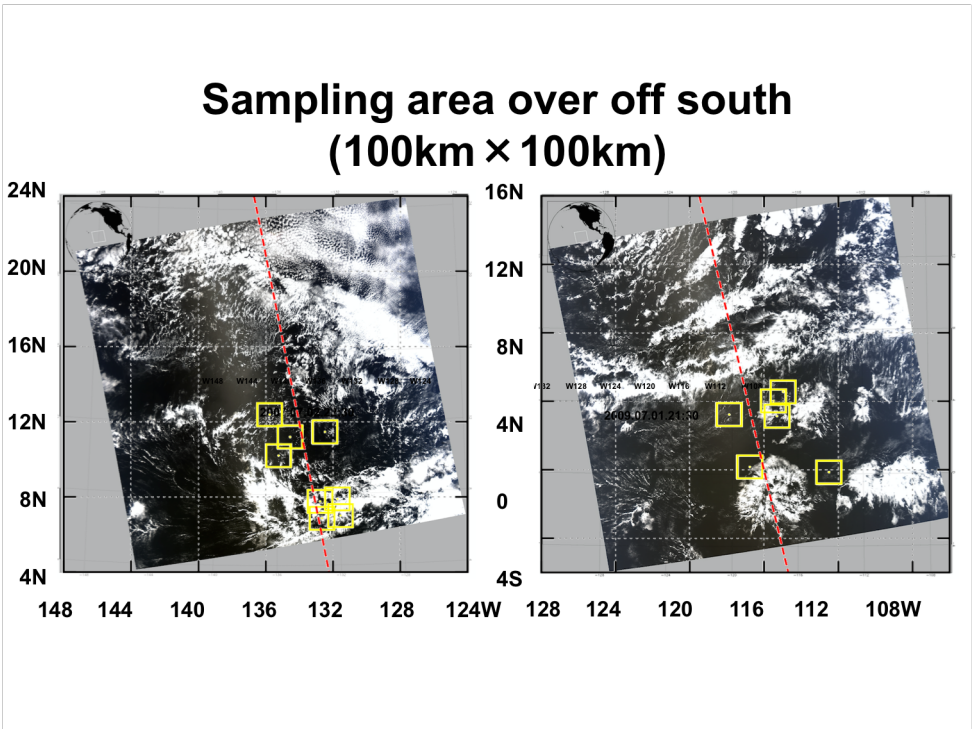

Figure 5.3. Sampling areas for constructing 3D cloud fields within a MODIS imagery on July 2 22:30, 2007 in left panel and on July 1 21:30, 2009 in right panel, respectively.

5.2.1 Analysis Case-No.1

Figure 5.4 shows a case of an optically thin cloud system, cloud-Case No.1 of 2 July 2007 at 7.00N, 131.55W in Table 2. The sampling area consists of 100x100 pixels (100kmx 100km) of the MODIS imagery along x-axis in the direction of the satellite track and y-axis in the cross-tracking direction. Figure 5.4 (a) shows the distance-height cross section (xz-section) of the averaged radar reflectivity factor profile along the y-axis. Panel (b) shows 2D distributions (xy-section) of the cloud parameters, τ, r_e, and *Tc*. Figure 5.4 (c) gives the constructed 3D fields (xyz-section) of the extinction coefficient. The cloud system has a mean τ as small as $<\tau> = 6.05$, but the horizontal standard deviation of τ is as large as $<\sigma_\tau>= 11.64$ with relatively thick cloud boxes (τ>30; show left figure in Fig 5.4 (b)) surrounded by clear sky area.

Figure 5.5a, b, c, d show differences of the area-averaged broadband solar radiative fluxes calculated by PPA, IPA, TIPA, and SIPA from those obtained by 3D RT computations. It is found that the PPA overestimates the reflected solar radiative flux by about 150 Wm^{-2}, like the idealized case of Type-A discussed in Chapter 4. The IPA slightly overestimates the reflected flux, but the error is less than about 15 Wm^{-2}. The error decreases with increasing SZA and becomes a small negative at θ_0=60°. This error behavior is similar that of Type-A clouds in Fig. 4.3a. The TIPA error is also as large as about 15 Wm^{-2}, while Fig. 5.5d shows that the magnitude of error of SIPA is less than 10 Wm^{-2} for all the SZA other than θ_0= 30°. In this case, I determined VSZA to be less 10° than SZA in SIPA through comparisons to 3D-RT simulations.

Figure 5.5e shows the error of the thermal radiative fluxes at TOA and BOA, illustrating that the IPA is more accurate than the PPA with errors less than 30Wm^{-2} for PPA and 10Wm^{-2} for IPA. It would be interesting to investigate a slant path approximation assuming an effective slant path direction for thermal radiative fluxes as well in future studies. Such an analysis should be useful to evaluate the infrared diffusivity factor of 1.66, which is often used for thermal radiation.

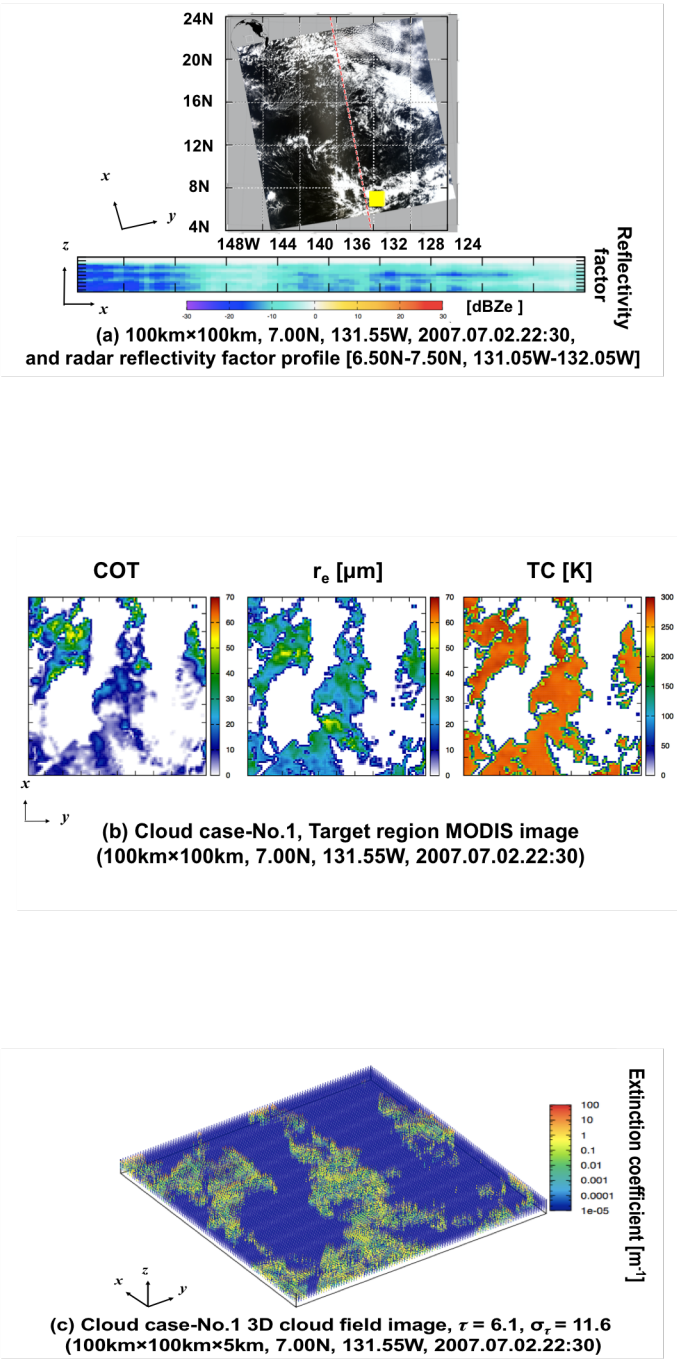

Figure 5.4. The structure of cloud system No.1, (a) The xz-section of the radar reflectivity factor profile averaged along y-axis. (b) Horizontal distributions (xy-section) of τ, r_e and *Tc* in the sampling area consisting of 100x100 pixels of MODIS imagery. (c) 3D field (xyz-section) of the extinction coefficient.

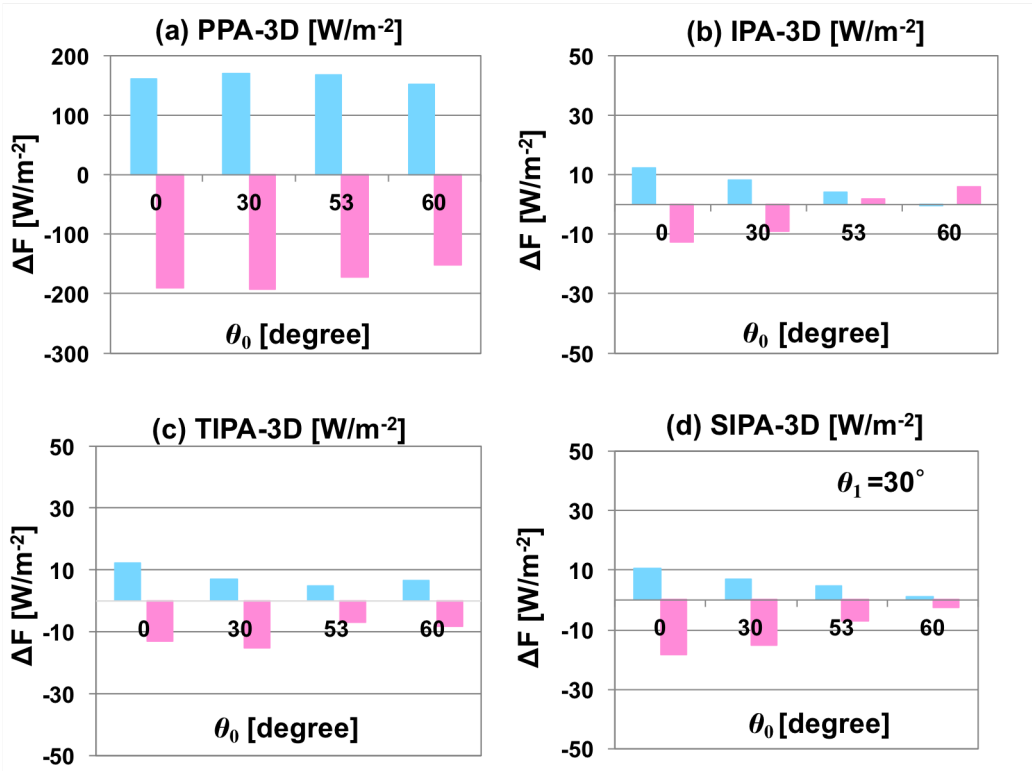

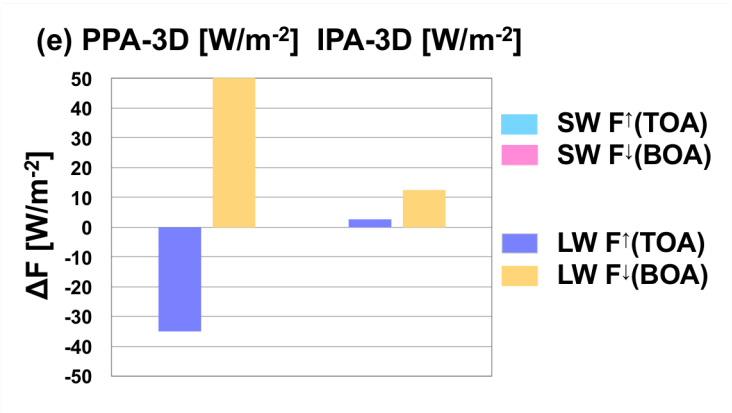

Figure 5.5. Errors of various plane parallel approximations relative to 3D computations for No.1 cloud case. (a) PPA-3D, (b) IPA-3D, (c) TIPA-3D, and (d) SIPA-3D for the broadband solar upward flux; (e) PPA-3D and IPA-3D for the broadband thermal radiative flux. Virtual solar insolation angles for SIPA is assumed to be $\theta_1=\theta_0-10°$ ($\theta_0 \neq 0°$), $\theta_0=\theta_1=0°$ and $\varphi_1=\varphi_0$.

5.2.2 Analysis Case-No.5

Figures 5.6 and 5.7 show the results for cloud-Case No.5 of 2 July 2007 at 7.61N, 133.79W in Table 2. This cloud system is optically thicker than the Case-No.1 with $<\tau>$ = 14.33 and $<\sigma_\tau>$ = 11.48. Figure 5.7 shows that the PPA error in the reflected solar flux is smaller than 100 Wm^{-2}, because the cloud system consists of relatively large decks adjacent to each other similar to Type-B and -C in Fig. 4.3(b) and Fig. 4.3(c). The IPA overestimates the 3D upward flux for all SZAs, and the error is more than 20 Wm^{-2}, which is significantly larger than that of Case-No.1. In this cloud case, the cloud field has an area with large cloud optical thickness reaching to 50, which is continuous to area with small cloud optical thickness. Throughout the domain, different heights of clouds are distributed. The TIPA and SIPA have errors less than 15Wm^{-2}. This error behavior is similar Type-B and -C in Chapter 4. The Case No.5 is relevant with Type-C as the error tendency of SZA.

The PPA error in the upward thermal radiative flux is similar to that of Case-No.1, whereas the BOA flux has an error as small as 14Wm^{-2} in Case-No.5. This is because the contrast of SST and temperature around the cloud bottom is similar to each other for the thick clouds. On the other hand, the IPA error is 10 Wm^{-2} and is like Case-1.

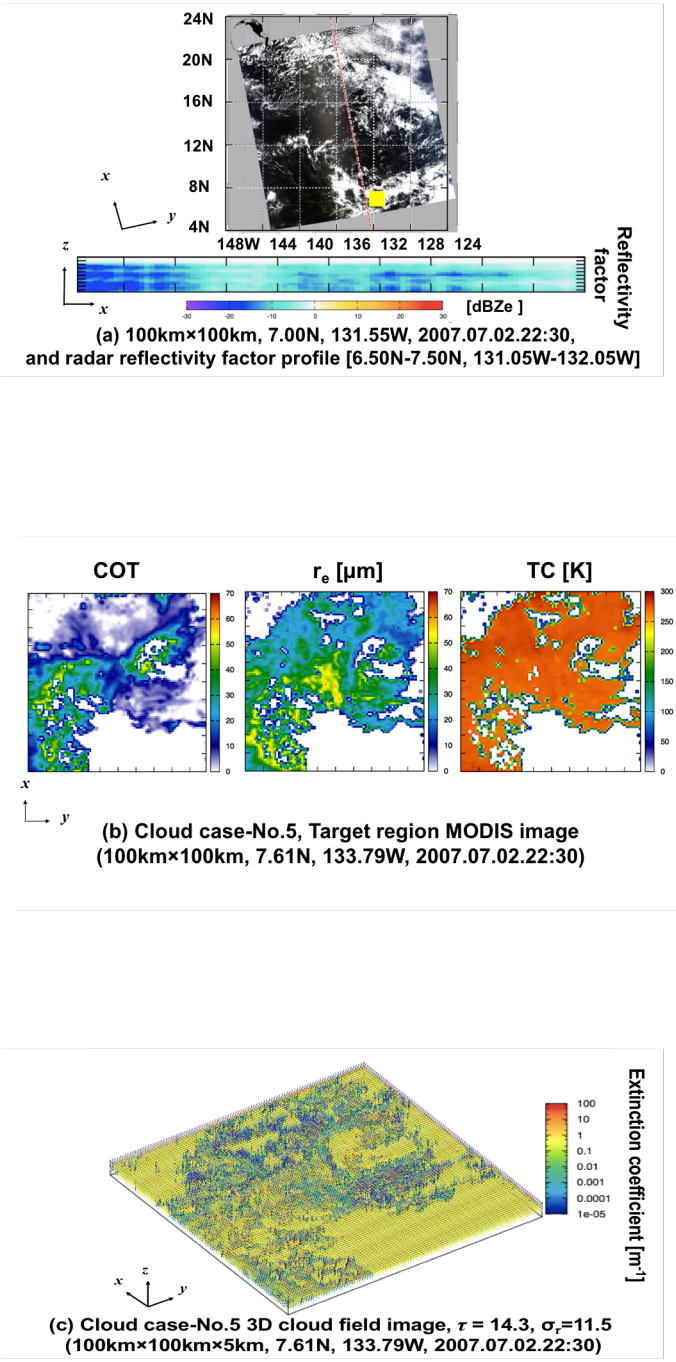

Figure 5.6. The structure of cloud system No.5, (a) The xz-section of the radar reflectivity factor profile averaged along y-axis. (b) Horizontal distributions (xy-section) of τ, r_e and *Tc* in the sampling area consisting of 100x100 pixels of MODIS imagery. (c) 3D field (xyz-section) of the extinction coefficient.

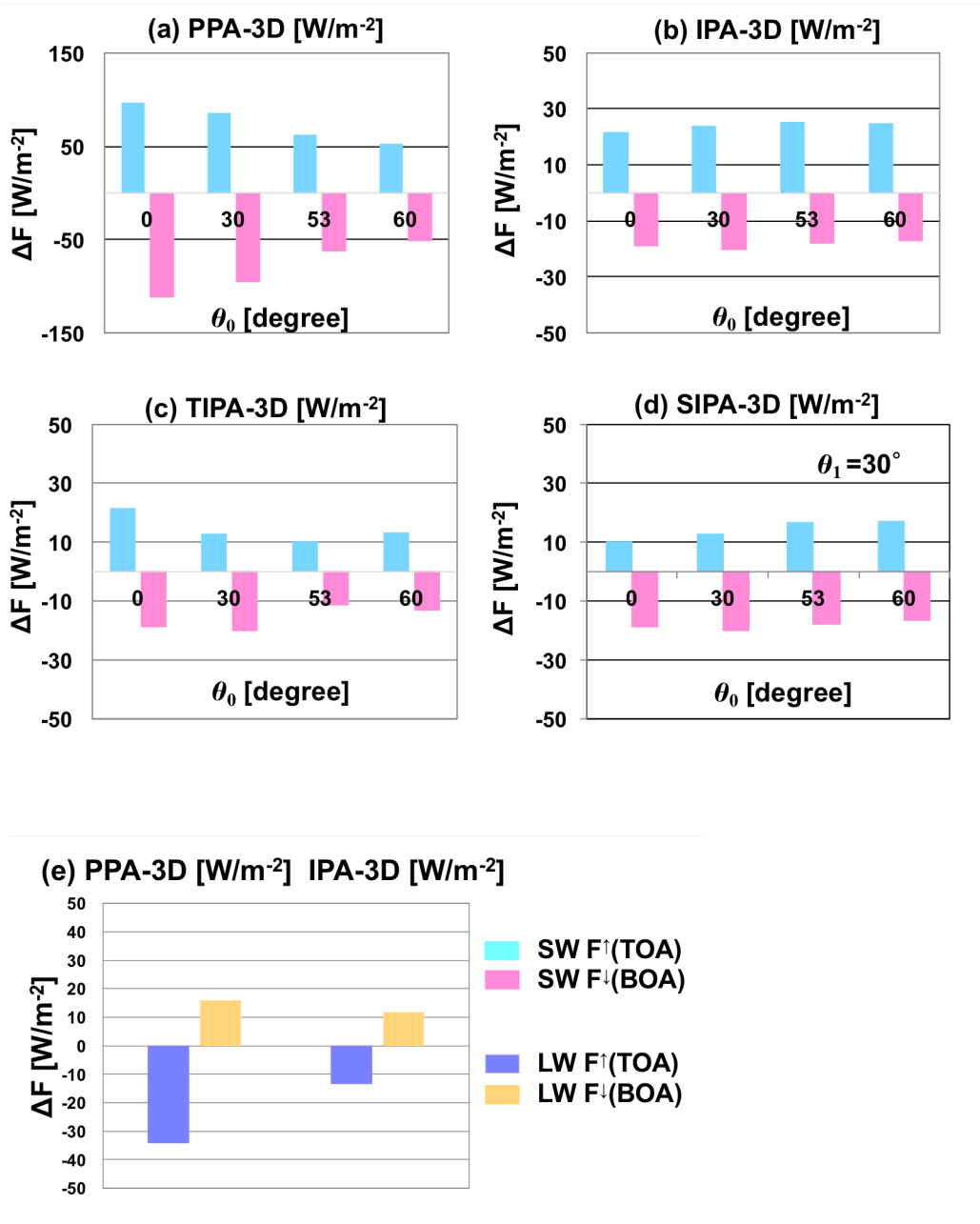

Figure 5.7. Errors of various plane parallel approximations relative to 3D computations for No.5 cloud case. (a) PPA-3D, (b) IPA-3D, (c) TIPA-3D, and (d) SIPA-3D for the broadband solar upward flux; (e) PPA-3D and IPA-3D for the broadband thermal radiative flux. Virtual solar insolation angles for SIPA is assumed to be $\theta_1=\theta_0-10°$ ($\theta_0 \neq 0°$), $\theta_0=\theta_1=0°$ and $\varphi_1=\varphi_0$.

5.2.3 Analysis Case-No.7

Figures 5.8 and 5.9 show the results for a very thin cloud-Case No.7 at 11.18N, 134.55W with $<\tau>$=0.32 and $<\sigma_{COT}>$= 1.30 in Table 2. In this case, there exist optically thin isolated cloud boxes of τ less than 10 in the model domain. The PPA error is less than 10 Wm^{-2} and increases with increasing SZA, contrary to other two cases. In this cloud case, the transmitted solar flux becomes large with increasing SZA for 3D-CRE because cloud is extremely thin ($<\tau> < 1.0$) and cloud amount is small (CF < 0.3) in contrast to PPA, especially. The IPA slightly overestimates the reflected flux, but the error is less than about 2 Wm^{-2}. The error decreases with large SZA and becomes small negative at θ_0=60°. The TIPA error is also as large as about 2 Wm^{-2}, while Fig. 5.9(d) shows that the magnitude of error of SIPA is less than 2 Wm^{-2} for all the SZA and decreases with large SZA. In this case, I also determined VSZA to be less 10° than SZA in SIPA through comparisons to 3D-RT simulations. These errors behaviors, except for the error behavior of PPA, are also similar the Type-A clouds in Fig. 4.3(a) and these approximations include small errors less than 5Wm^{-2}. Especially the SIPA is successful to reduce the errors at large SZAs.

Figure 5.9(e) shows that the 3D cloud effect is larger for the thermal radiation than those of two other cases, in relative sense in comparison with the shortwave cases (Fig.5.9(a)-(d)), especially for the downward thermal radiative flux.

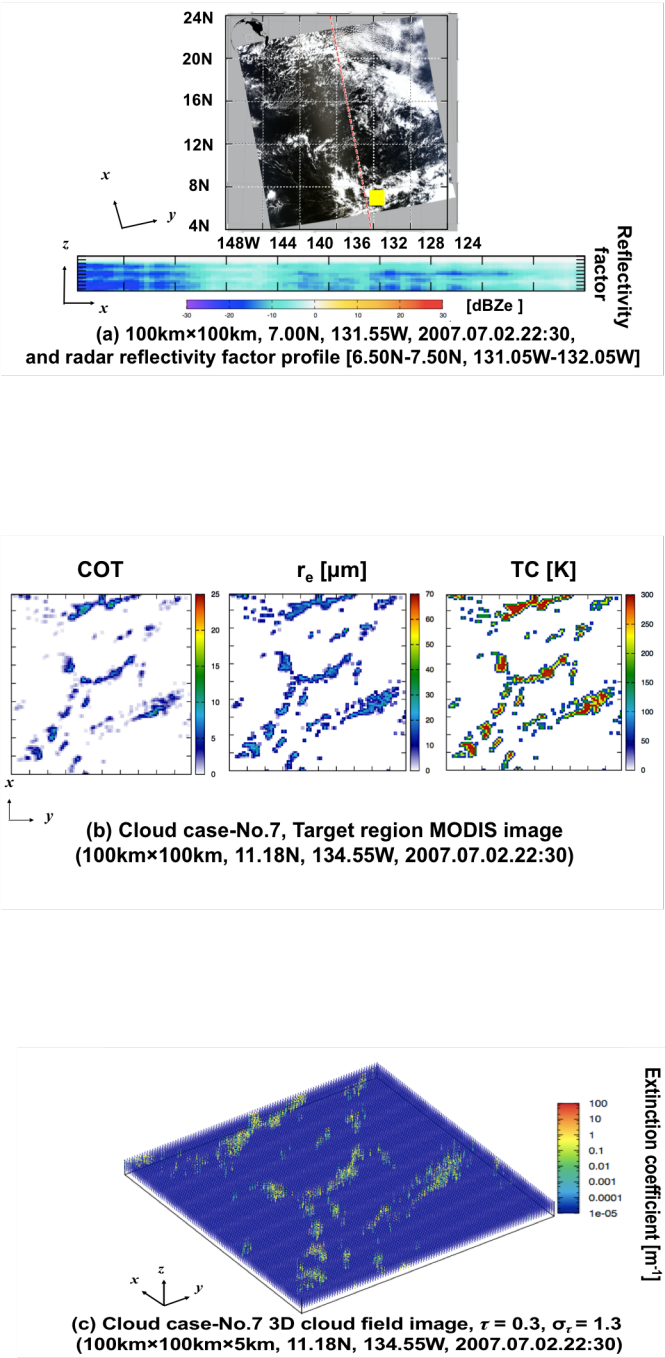

Figure 5.8. The structure of cloud system No.7, (a) The xz-section of the radar reflectivity factor profile averaged along y-axis. (b) Horizontal distributions (xy-section) of τ, r_e and *Tc* in the sampling area consisting of 100x100 pixels of MODIS imagery. (c) 3D field (xyz-section) of the extinction coefficient.

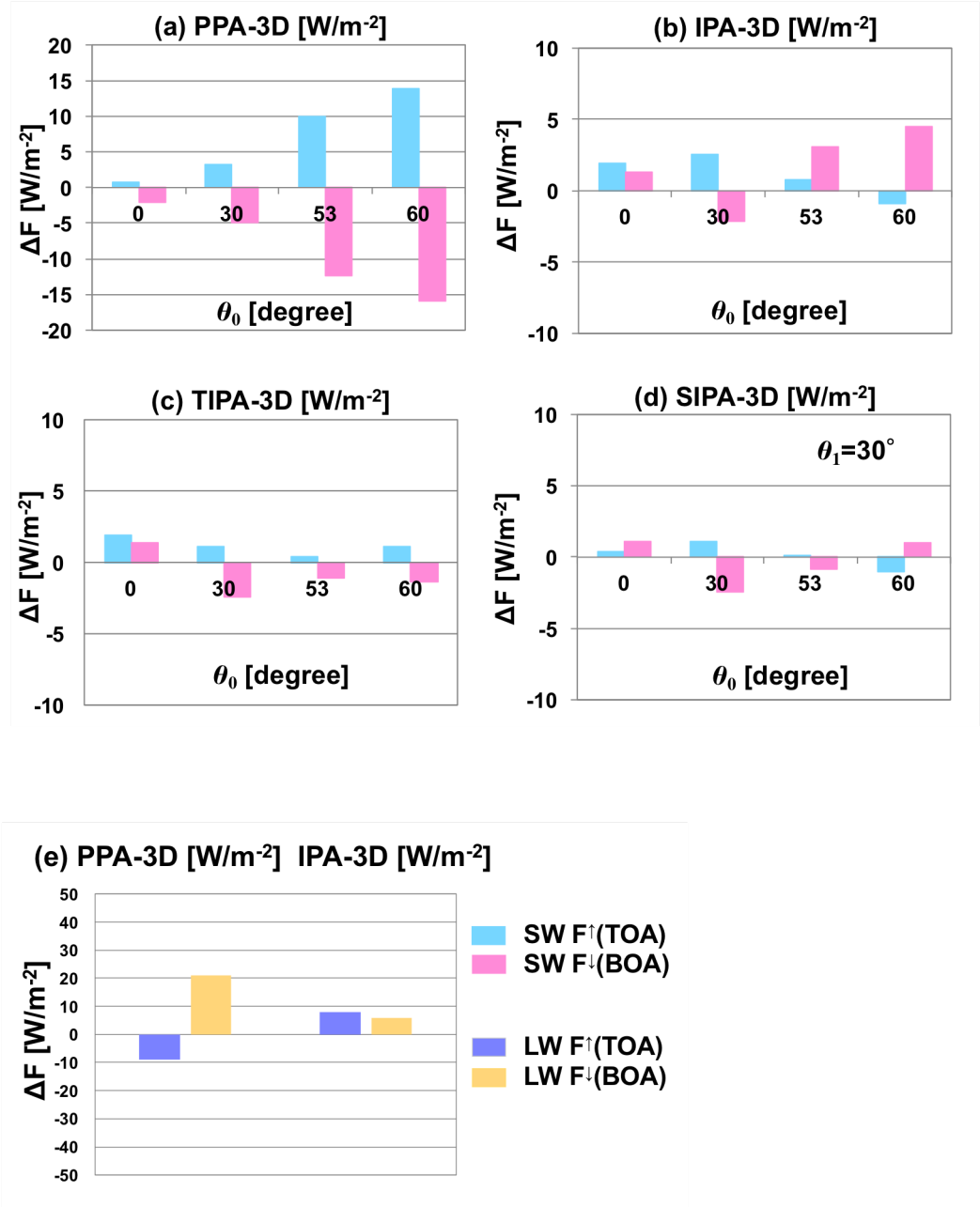

Figure 5.9. Errors of various plane parallel approximations relative to 3D computations for No.7 cloud case. (a) PPA-3D, (b) IPA-3D, (c) TIPA-3D, and (d) SIPA-3D for the broadband solar upward flux; (e) PPA-3D and IPA-3D for the broadband thermal radiative flux. Virtual solar insolation angles for SIPA is assumed to be $\theta_1=\theta_0-10°$ ($\theta_0 \neq 0°$), $\theta_0=\theta_1=0°$ and $\varphi_1=\varphi_0$.

The comparisons between approximations and 3D-RT simulations for all the 15 cases listed in Tables 2 and 3 are summarized in this subsection. Figure 5.10 shows scatter plots of reflected solar fluxes obtained from approximations against those from 3D computations for SZAs of θ_0= 0, 30, 53, and 60°. The figure shows that PPA largely overestimates the reflected fluxes for all the SZAs when the flux exceeds 150 Wm^{-2}. The largest error is about 164 Wm^{-2} with SZA 60° for cloud-Case No.3 in Table 2 for medially large fluxes ranging in 150-400 Wm^{-2}. The errors are much smaller for more homogeneous cloud-Case No.7 in Table 2, indicating that the 3D-CRE has a large dispersion in the present cloud ensemble including a variety of spatial inhomogeneity.

The IPA has small errors for all the cases. It is interesting to find that the underestimation of the reflected solar flux, which is found in an idealized cloud case (Type-A) over large SZAs in Chapter 4, is not significant in the present ensemble. Rather, there are obviously slight overestimations in Fig 5.10. This is because the high-cloud blocking effect overcomes the clear-sky obscuring effect in the 3D cloud structure of these observed cases. The IPA error is less than 10Wm^{-2} for fluxes less than 300Wm^{-2}, whereas the error exceeds 50 Wm^{-2} for fluxes larger than 300Wm^{-2}. Figures 5.10 also indicates that the TIPA works better than the IPA: the TIPA error is less than 5Wm^{-2} for fluxes less than 300Wm^{-2}, though the error exceeds 12 Wm^{-2} for fluxes larger than 300Wm^{-2} and for large SZAs.

2007.07.02. 22:30 Case number	Lat Lon	<τ>	σ_{COT}	CF ($COT_{i,j}$ > 0.1)	SZA θ_0 [degree]	Error $_{PPA}$ [Wm^{-2}] SW F↑ (TOA)	Error $_{IPA}$ [Wm^{-2}] SW F↑ (TOA)	Error $_{TIPA}$ [Wm^{-2}] SW F↑ (TOA)	Error $_{SIPA}$ [Wm^{-2}] SW F↑ (TOA)
1	7.00N, 131.55W	6.1	11.6	0.38	60°	151.96	-0.38	11.41	1.05
2	6.85N, 132.64W	4.3	7.8	0.36	60°	126.16	-2.44	8.48	3.02
3	7.75N, 132.77W	6.8	12.4	0.38	60°	164.75	-2.59	10.18	3.72
4	7.89N, 131.74W	10.3	9.9	0.42	60°	46.71	13.53	8.81	11.59
5	7.61N, 133.79W	14.3	11.5	0.58	60°	52.15	24.53	13.37	17.27
6	10.19N, 135.23W	1.3	3.1	0.31	60°	53.39	2.26	4.64	0.91
7	11.18N, 134.55W	0.3	1.3	0.086	60°	13.79	-0.88	1.11	-1.06
8	11.45N, 132.47W	0.6	2.0	0.13	60°	28.13	-1.49	1.26	-1.36
9	12.37N, 135.76W	4.1	3.8	0.51	60°	37.28	14.47	8.37	10.48

Table 2. Sampling data information for cloud cases of 2 July 2007, i.e. latitude, longitude, mean and standard deviation of the τ field; Cloud Fraction is the area fraction of the optical thickness larger than 0.1 (τ>0.1); solar zenith angles (SZAs) for calculations; errors of broadband solar upward fluxes at TOA (Wm^{-2}) calculated by various plane parallel approximations (PPA-3D, IPA-3D, TIPA-3D, and SIPA-3D). Shown errors assume the same θ_0= 60° .

2009.07.01. 21:30 Case number	Lat Lon	<τ>	σ_{COT}	CF ($COT_{i,j}$ > 0.1)	SZA θ_0 [degree]	Error $_{PPA}$ [Wm^{-2}] SW F↑ (TOA)	Error $_{IPA}$ [Wm^{-2}] SW F↑ (TOA)	Error $_{TIPA}$ [Wm^{-2}] SW F↑ (TOA)	Error $_{SIPA}$ [Wm^{-2}] SW F↑ (TOA)
10	4.55N, 114.97W	5.6	5.8	0.60	60°	43.71	43.15	9.56	6.68
11	4.02N, 115.49W	13.2	11.3	0.62	60°	69.66	47.79	18.58	19.72
12	3.13N, 115.30W	10.8	9.6	0.78	60°	58.67	16.95	12.84	9.73
13	0.17N, 116.77W	9.8	9.8	0.69	60°	56.01	13.07	7.91	4.84
14	3.22N, 117.88W	7.0	7.0	0.67	60°	30.44	42.27	0.434	-1.14
15	0.14N, 112.50W	5.8	10.9	0.38	60°	141.59	-4.71	13.27	-1.14

Table 3. Sampling data information for cloud cases of 1 July 2009, i.e. latitude, longitude, mean and standard deviation of the τ field; Cloud Fraction is the area fraction of the optical thickness larger than 0.1 (τ>0.1); solar zenith angles (SZAs) for calculations; errors of broadband solar upward fluxes at TOA (Wm^{-2}) calculated by various plane parallel approximations (PPA-3D, IPA-3D, TIPA-3D, and SIPA-3D). Shown errors assume the same θ_0= 60° .

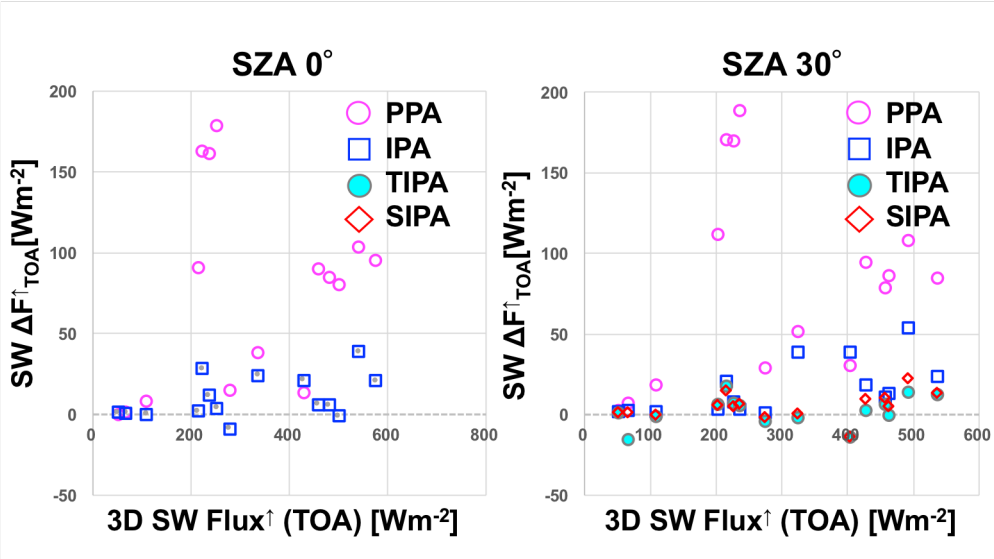

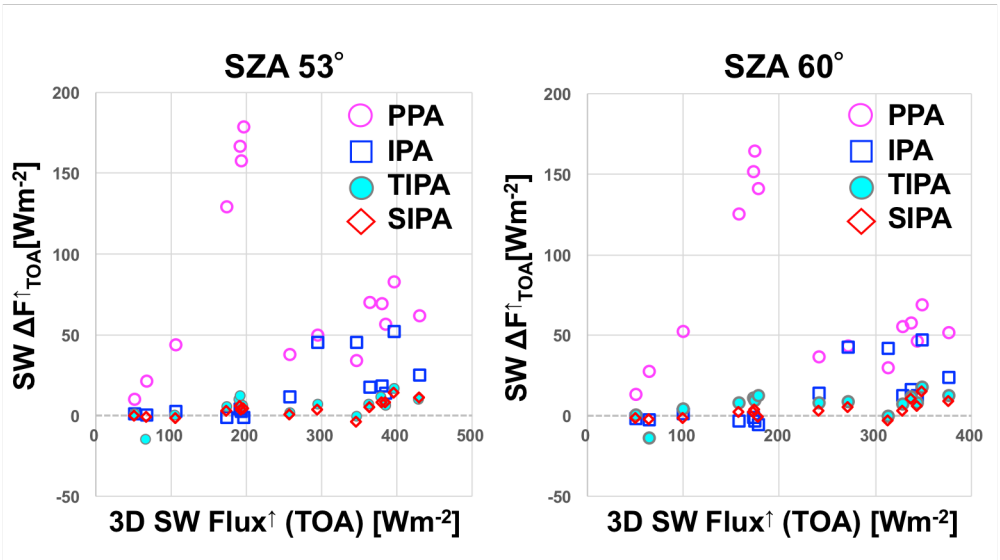

Figure 5.10. Scatterplot of the error of the reflected solar radiative fluxes at TOA between various plane parallel approximations (PPA, IPA, TIPA) in y-axis and the reflected solar radiative fluxes at TOA of 3D-RT simulations in x-axis for all the observed cloud systems listed in Table 2 and 3. Solar zenith angles are assumed to be 0, 30, 53 and 60°.

Figure 5.10 also shows the error of TIPA and SIPA for reflected solar radiative fluxes relative to 3D-RT simulations for all the observed cloud cases. TIPA is known as an effective approximation to improve underestimate of IPA around θ_0=60° (Varnai et al ., 1998). It is a key to find effective VSZA (in Chapter 4) to reduce the error around large SZA. The figure indicates that TIPA and SIPA work well with error less than 20 Wm^{-2} for all the cloud cases. More detailed investigation of the plot, however, reveals that the SIPA error is less than that of TIPA for cloud-1, 2, 3, 6, 7, 10, 12, 13 and 15, whereas vice versa for cloud-4, 5, 7, 8, 9 11 and 14. This implies that the former group of the present real cloud cases are more and/or less similar to Type-A clouds, for which SIPA works better than IPA and TIPA; the latter group is similar to the Type-B and/or -C.

The thermal infrared radiative fluxes from PPA and IPA are also compared in Figure 5.11 for upward flux at TOA and downward flux at BOA. It is found from the figure that both the PPA and IPA have larger errors than those for solar flux cases. The PPA largely underestimates the upward flux by 40Wm^{-2} and largely overestimates the downward flux by 70Wm^{-2}. These errors arise from underestimation of the upward thermal radiation by blocking clear sky from which the warm surface radiation escapes to space. These errors become smaller for small and large fluxes to make the error profile an arch-type shape, which supports the usefulness of the split window techniques for obtaining cloud fraction from space (Inoue et al., 2002; Oakley et al., 1982). The IPA error is less than 40Wm^{-2}, but looks randomly spread in the plot. This random error characteristic indicates the difficulty in finding a suitable correction method for the thermal radiative fluxes. This suggests that the effect of temperature profiles should be suitably taken into account appropriate corrections for approximations of thermal radiative transfer. This is however beyond the scope of this study and should be addressed in future studies.

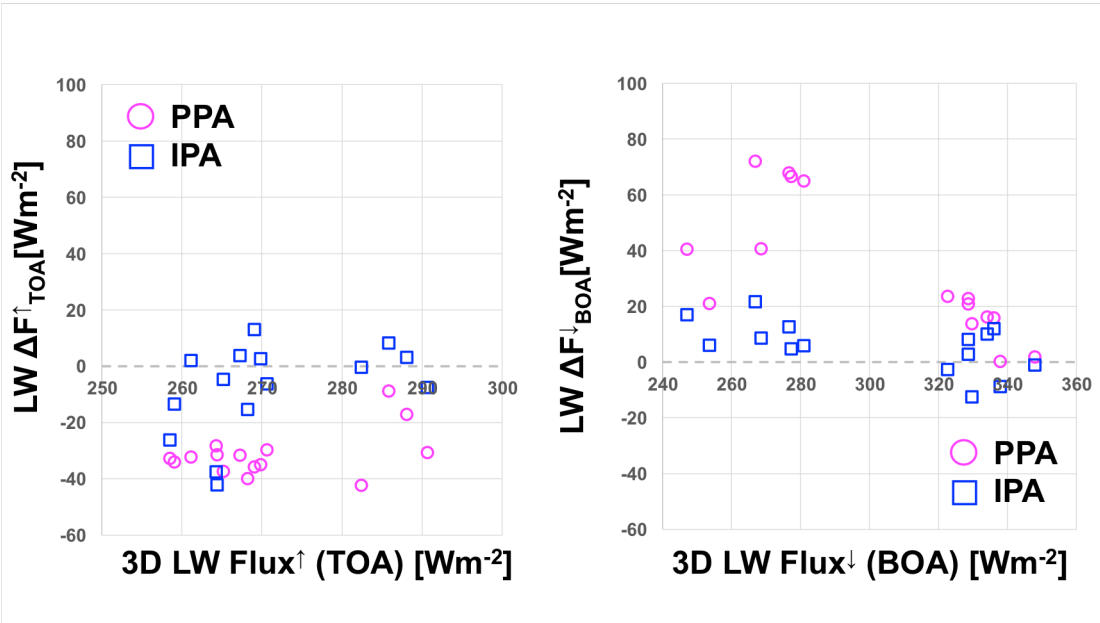

Figure 5.11. Comparison of broadband thermal infrared radiative fluxes by PPA and IPA with those by 3D-RT calculation. Upward (TOA) and downward (BOA) fluxes are shown. Scatterplot of the error of the thermal infrared radiative fluxes between various plane parallel approximations (PPA, IPA) in y-axis and the thermal infrared radiative fluxes of 3D-RT simulations in x-axis for all the observed cloud systems listed in Table 2 and 3.

5.3 Classification of 3D cloud radiative effect in observed "real" cloudy atmosphere with broad-band flux

The correspondence in error characteristics between the real observed cases and the idealized cloud types hinted in Fig. 4.3 can further be understood more clearly as following. The error characteristics of approximations for the three idealized cloud types (Type-A, B and C) are well described by dependence of the error (relative to 3D-RT) on SZA in the form of Fig. 4.4 as discussed in Chapter 4. A remarkable characteristic distinguishing the Type-A and the Type-B, C is that the IPA error changes its sign from positive to negative with increasing SZA in Type-A (Fig. 4.4(a)) whereas the IPA error is always positive regardless of SZA in Type-B and C (Figs. 4.4(b) and 4.4(c)). This means that the IPA-3D error at θ_0=60° relative to 0° is always negative when the cloud system morphology that is effective to incoming solar radiation is similar to Type-A. However, the IPA-3D error becomes positive for cloud systems in all SZA when the cloud morphologies are similar to Type-B or C. It is therefore suggested to employ the sign of the IPA error difference between the two SZAs as a criterion distinguishing which I defined as an index G, the cloud system into those more like either Type-A or Type-B, C.

$$G \equiv [\Delta F_{IPA}(60°) - \Delta F_{IPA}(0°)], \tag{5.1a}$$

where

$$\Delta F_{IPA}(\theta_0) \equiv < f_{IPA}(\tau_{i,j}, \mu_0, \phi_0) - f_{3D}(\tau_{i,j}, \mu_0, \phi_0) >_{i,j} . \tag{5.1b}$$

According to this criterion, the observed cloud cases of 1, 2, 3, 7, 8 and 15 are classified as similar to Type-A and the cases 4, 5, 6, 9, 10, 11, 12, 13 and 14 are classified to more like Type-B or C. According to Tables 2 and 3, the two groups

obtained from this classification are also found to have another characteristic of COT. The mean value of COT is larger than the standard deviation for the former group and vice versa for the latter group. This implies that our morphology-based error classification according to the IPA error behavior also corresponds to a difference in statistical properties of cloud systems.

This classification leads to a similar result to that obtained using TIPA/SIPA error behaviors of Fig. 4.4 discussed above, suggesting a robustness of our classification method. Type-B and -C could further be distinguished by another key characteristic shown in Figs. 4.4(b) and 4.4(c), i.e. different behaviors of the TIPA error as a function of SZA between Type-B and C. It is found in Fig. 4.4b that the TIPA error for Type-B clouds has a saddle point around θ_0=30° beyond which TIPA overcorrects the slant path for large SZAs as discussed in Chapter 4. On the other hand, the Type-C cloud shown in Fig. 4.4(c) has the TIPA error less dependent on SZA because of the high cloud effects as also discussed in Chapter 4. These characteristics of the TIPA error suggest a use of the second order derivative using four points (θ_{01}, θ_{02}, θ_{03}, θ_{04}) around the saddle point θ_{03} as defined below as an index for distinguishing between Type-B and C:

$$H \equiv [\Delta F_{TIPA}(\theta_{04}) - \Delta F_{TIPA}(\theta_{03})] - [\Delta F_{TIPA}(\theta_{02}) - \Delta F_{TIPA}(\theta_{01})], \quad (5.2a)$$

where

$$\Delta F_{TIPA}(\theta_0) \equiv < f_{TIPA}(\tau_{slant}(\mu_1, \phi_1), \mu_0, \phi_0) - f_{3D}(\tau_{i,j}, \mu_0, \phi_0) >_{i,j} . \quad (5.2b)$$

For our target clouds, I found θ_{01}=0°, θ_{02}=30°, θ_{03}=30° and θ_{04}=60° are useful for the classification. According to discussion above, the Type-B is expected to have a large value of *H*-index, whereas the *H*-index should take a small value for Type-C. I find that an *H*-threshold around 25 Wm^{-2} could separate classes B and C in this study. Based on this criterion, the observed cloud cases of 10, 11 and 14 are classified as Type-B and the cases of 4, 5, 6, 9, 12 and 13 as Type-C. Figure 5.12 shows the overall classification of all the observed cases into Type-A, B and C according to the two criteria defined above in the form of the two-dimensional representation based on the two indices. It is illustrated in Fig. 5.12 how the real observed clouds can be classified in the context of error characteristics of existing approximations for different structures of clouds. This

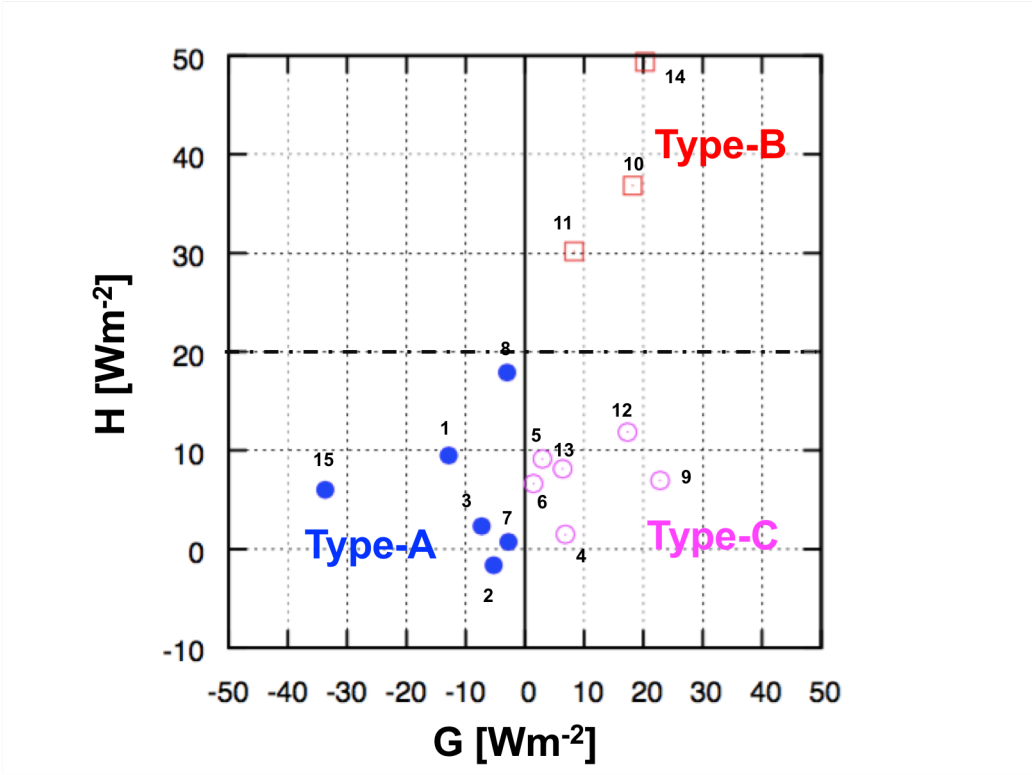

Figure 5.12. Scatterplot between the two error indices defined according to error characteristics of IPA and TIPA relative to 3D computations for all the observed cloud cases (see text for definitions of the indices). Different colors/symbols denote different values of the two indices corresponding to different cloud types, i.e. Type-A, B and C (see also text for details).

classification provides a novel way to link the error of approximations to specific cloud morphology effective to solar radiative transfer.

The above classification is derived from 3D-RT full simulations. However, I inspect the observed cloud morphology types classified as Type-A, B and C in Chapter 4 from the two perspectives, i.e. 1) to plot Cloud Fraction (CF) and effective Cloud Fraction (CF_e) profiles in altitude, 2) to make the RGB composite maps form MODIS 3 channels (0.6, 2.1 and 11 μ m). Cloud Fraction means a general cloud coverage which I count a "cloud" when cloud optical thickness in grid box is larger than 0.1 in this study. I define CF_e that considers horizontal homogeneity of cloud optical thickness using regional average cloud optical thickness $<\tau>$ and the standard deviation σ_τ in this study. The formula is described as follow,

$$CF_e = \frac{1}{1+(\sigma_{\tau_c}/<\tau_c>)^2} \quad . \tag{5.3}$$

Large CF_e means more homogeneous cloud field, and vice versa. The RGB composite map provides a information of the characteristic cloud top, i.e. Red (11μm), Green (0.6μm) and Blue (2.1μm) show low and thin cloud, high and thick cloud and high and thin cloud, respectively. I show 1) CF and CFe profiles in altitude of observed 15 cloud cases classified as Type-A, B and C in Chapter 4 in Fig 5.13, 5.14 and 5.15, respectively and 2) representative RGB composite maps of each type in Fig 5.16.

In case of observed cloud classified as Type-A, both the CF and the CFe profiles in altitude are less than 0.5 in Fig 5.13 and RGB composite map shows the isolated clouds exist in clear sky region in Fig 5.16(a). These clouds correspond to Type-A cloud in Chapter 4. The CFe profiles in altitude of Type-B are large in low altitude especially and Type-C vice versa, nevertheless the CF profile in altitude in case of Type-B and C are large all over the altitude in Fig 5.14 and Fig 5.15. The cloud field of Type-B is, therefore, characteristic as more inhomogeneous at cloud base. Conversely, the cloud field of Type-C is more homogeneous at cloud top. These RGB composite maps characteristics also correspond to Type-B and C, respectively. The RGB composite map in case of Type-B indicates inhomogeneity at cloud top because high and low cloud are mixed in Fig 5.16(b). Conversely, the RGB composite map of Type-C shows more homogeneous at cloud top field in Fig 5.16(c). These

characteristics using CF and CF_e profiles in altitude and RGB composite map without 3D-RT simulation are consistent to the classifications using two index with 3D-RT full simulations. This classification provides an original way to link CF and CF_e profiles and RGB composite map to specific cloud morphology effective to solar radiative transfer.

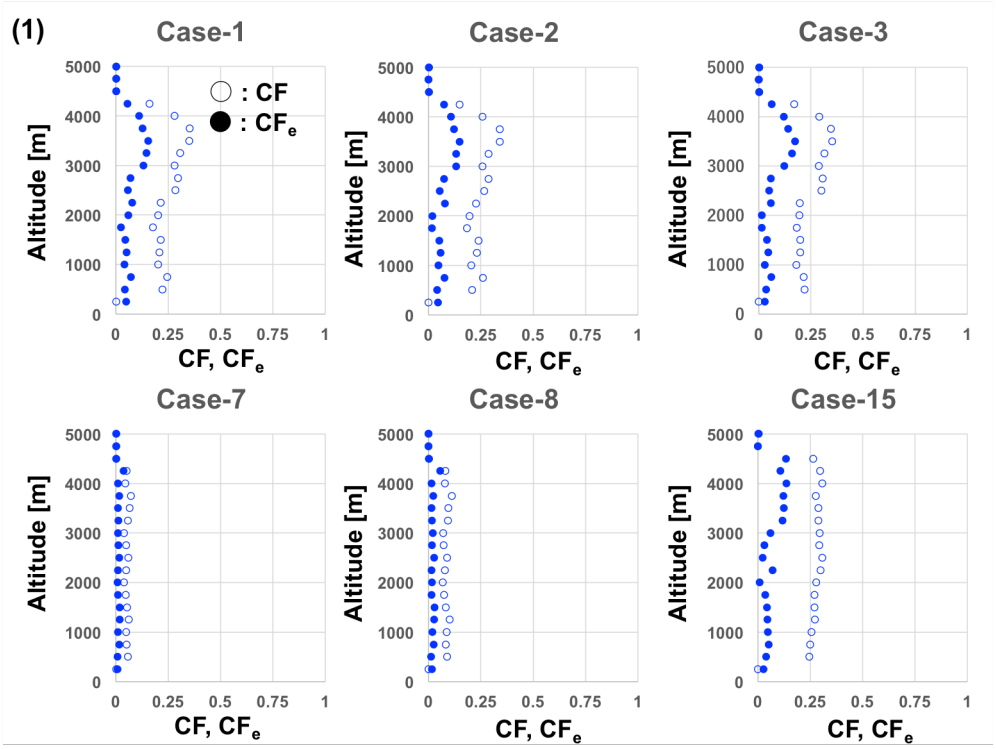

Figure 5.13. Cloud Fraction (CF) and Effective Cloud Fraction (CFe) profiles in altitude classified as Type-A.

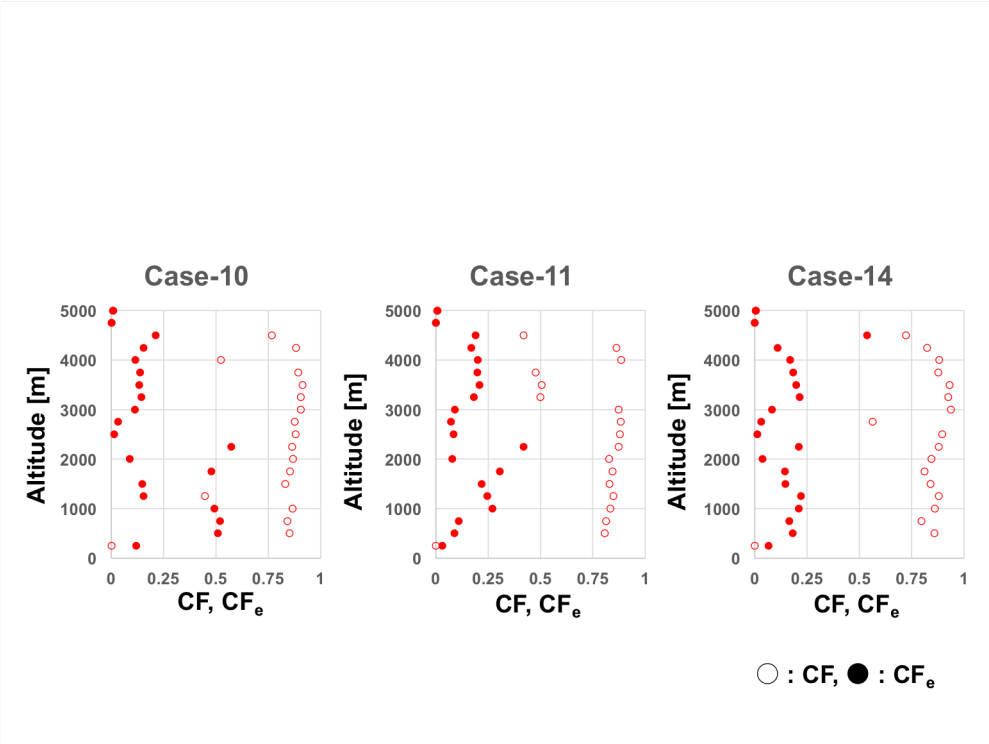

Figure 5.14. Cloud Fraction (CF) and Effective Cloud Fraction (CFe) profiles in altitude classified as Type-B.

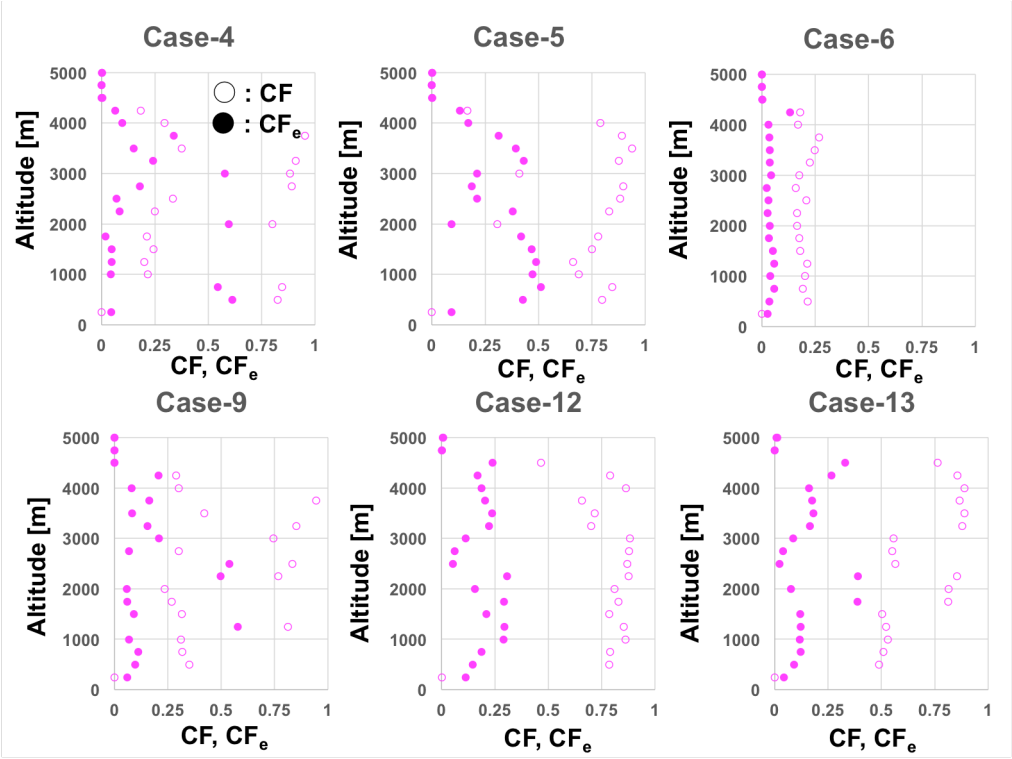

Figure 5.15. Cloud Fraction (CF) and Effective Cloud Fraction (CFe) profiles in altitude classified as Type-C.

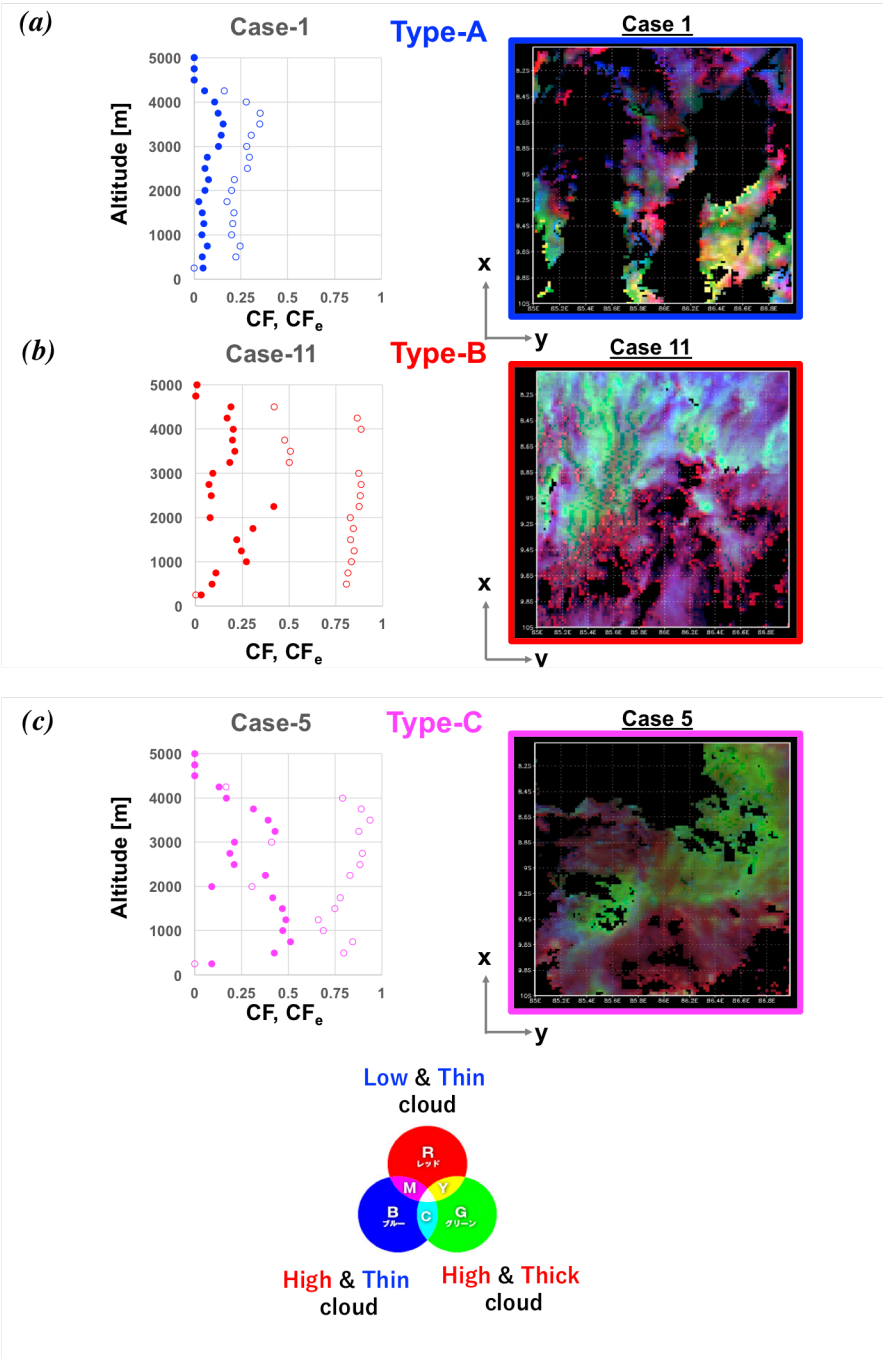

Figure 5.16. The right figures show the RGB composite map form MODIS 3 channels (0.6, 2.1 and 11 μ m) of Type-A,B and C. The RGB composite map can provide the characteristic cloud top information, i.e. Red (11μm), Green (0.6μm) and Blue (2.1μm) shows low and thin cloud, high and thick cloud and high and thin cloud, respectively. The left figures show each CF and CF_e profiles in altitude.

Chapter 6

Conclusions

This study investigates broadband radiative fluxes in the 3D cloud-laden atmospheres using a 3D radiative transfer model and satellite-observed cloud data. The 3D extinction coefficient fields are constructed by a newly devised Minimum cloud Information Deviation Profiling Method (MIDPM) that extrapolates CPR radar profiles at nadir into off-nadir regions within MODIS swath based on match-up information of MODIS-derived cloud properties and radar reflectivity profiles. The method is then applied to low level maritime water clouds off California. I use a pair of the MODIS/Aqua and CPR/CloudSat data as a "cloud library". The consistency between these two cloud data is validated by comparisons of effective particle radii (r_e) obtained from two independent measurements, i.e. MODIS-observed effective radius ($r_{e,\,\mathrm{MODIS}}$) and CPR-derived effective radius ($r_{e,\,\mathrm{CPR}}$), assuming vertically invariant homogeneous cloud layer conditions. The two effective radii are found to be consistent within 7-25μm with accuracy for the cloud scenes adopted in this study, where the cloud library includes about 500~600 sampling data from the 2000km length of the A-Train track. Given this consistency of the two independent cloud data, I use cloud microphysical parameters, i.e. cloud optical thickness (τ), effective particle radius (r_e) and cloud top temperature (Tc) from MODIS cloud information, which are collocated with CloudSat radar profiles, for construction of 3D cloud fields.

This method is notably different from a previous method based on radiances (Barker et al., 2011), and makes more sense physically in constructing 3D cloud fields without large dependence on the illumination condition that significantly influences the radiance-based method. Given this advantage of our new method, we may extend our sampling area far from the CPR orbit compared to the radiance-based method.

Some works, however, are left for elaboration of the methods developed by the present study. First of all, our choice of using the cloud microphysical properties needs to be assessed in terms of the effects of 1D retrieval error and information contents of

the retrieval. Secondly, it is important to investigate how the radiative fluxes obtained from the 3D-RT computation depend on the methods of sampling and 3D field construction. Our result should be compared with the radiance-based algorithm of Barker et al (2011, 2012) in this context. As for our assumption of a fixed effective particle radius (r_e) at 13 μm, I should further validate the r_es obtained from MODIS and CPR described in Chapter 3. Thirdly, the resulting 3D cloud fields can be different depending on the sampling distances l_1, l_2 and l_3 defined in Section 3.1. Barker et al. (2011, 2012) set their model domain so as to allocate the CPR track at the center of the domain, i.e., l_3= 0 km, but I select model domains from a wider area distant within l_3= 500 km from the CPR track for 3D-CRE assessment. Then, there is an issue of how to select an optimum member from the library. In the present method, I select a member for which the cost function f in Eq. (3.8) takes the minimum value. However, there is an ambiguity in the allowance to determine the minima. A kind of a closeness index could be defined and constructed with a simultaneous use of f-value and the geometrical distance between the sampling pixel and the library-member pixel. Future studies should be devoted to investigation of these issues to further validate the reliability of the 3D cloud construction method.

The PPA approximation is found to overestimate the broadband reflected solar flux in the range of 150-400Wm^{-2} for optically medium thick clouds. The IPA approximation significantly improves this large PPA error by taking account for the radiation effects of each pixels which tends to have a cancellation effect of transverse photon transfer between atmospheric columns of different optical thickness (Marshak et al.,1998). It is, however, found that the IPA has a small but non-negligible errors of about 20Wm^{-2} for thick and large SZA cases caused by clear sky obscuring effect and tall-cloud blocking effect, i.e. effect of cloud holes being less illuminated by the direct solar ray when SZA becomes large and effect of tall clouds blocking radiation reflected by low height clouds, respectively. Most of the IPA errors is positive, indicating that the latter effect dominates the former in the present 15 cloud ensemble. The TIPA seems to correct these effects by setting a slant path optical thickness for the direct solar insolation i.e. $\theta_1 = \theta_0$ in Eq. (4.5). Our simulation shows, however, this correction tends to be overestimated for large SZA due to dominance of diffuse radiation. In attempt to mitigate this overcorrection, I develop a SIPA approximation that modifies the idea of TIPA with a less slant path at around $\theta_1=\theta_0$-10° (θ_0>10°) to take into account the diffuse

radiation effects. The result shows a reduction of error in SIPA for large optical thickness and SZA cases to within 5 Wm^{-2}. A critical issue in SIPA is how to find the optimum value of Virtual Solar Zenith Angle (VSZA), i.e. $\theta_1=\theta_0$-10° as determined in this study, for the slant path calculation. This is particularly the case for occasions where solar incidence is close to the normal. A key element that influences the optimum value of VSZA is the distance between adjacent clouds. Although SIPA accuracy varies in cloud types like Type-A, B and C in Chapter 4, it is most accurate approximation assuming $\theta_1 = \theta_0$-10° in observed cloud field in Chapter 5. It is necessary in future studies to examine how the optimum VSZA can vary depending on different distances between adjacent clouds to use more factors related to cloud optical parameters like Wissmeier et al. (2013) . Another interesting problem is to develop a SIPA for thermal radiation as well. One possible idea is to use diffusivity factor of 1.66 (Liou, 1974) for 1/cos (θ_1). Such a study should shed a new light on the traditional value of the diffusivity factor in the context of 3D radiative transfer.

To our knowledge there are very few studies of 3D cloud effects on the broadband radiative fluxes using real satellite-observed data, other than Barker et al. (2011, 2012), so that our analysis of 15 observed cloud systems would be a useful addition to state-of-the-art knowledge for understanding 3D cloud effects on Earth's radiation budget. Another novel aspect of this study is the development of LW broadband 3D-RT computation for cloudy atmosphere. This is also a significant addition to the radiative transfer study where there exists only a few 3D-RT models for broad-band LW calculation.

Using these broad-band error behaviors as a function of SZA, I further classify our observed 15 cloud cases into three simple, idealized cloud types, i.e. isolated cloud type (Type-A), upper cloud-roughened type (Type-B) and lower cloud-roughened type (Type-C) based on two indices (*G* and *H*) introduced using the SZA-dependence of the flux error of IPA and TIPA. Such classifications are also associated with quantitative indices of cloud morphology defined by the cloud fraction (CF) and effective cloud fraction (CFe) profiles. The classification can also be visualized in the form of the RGB composite map derived from MODIS 3 channels without 3D-RT full simulations. There exist a number of studies for 3D-RT for cloudy atmosphere that just analyze 3D-RTE using idealized fractal or statistical cloud models to theoretically evaluate the error of existing 1D approximations to 3D-RT simulations. However, there are few quantitative

assessments of these error tendencies. Our classification method developed by this study is an effective way to quantitatively investigate the characteristics of three-dimensional nature of CRE and their relation to cloud morphology.

It will effective and practical methods such as SIPA and the classification of 3D-CRE using global cloud observation data to contribute to deal with large volume data such as global satellite observation data or to simulate for numerical model, i.e. LES, CRM and GCM. In addition, our results will contribute as more realistic 3D-RT parameterization for the radiative flux estimated by 1D-RT code implemented in LES, CRM and GCM, it can, therefore, reduce an uncertainty of cloud radiative effects.

Space-borne CPR and lidar will be carried by the EarthCARE satellite (Illingworth et al., 2015). A combined analysis of space-borne CPR and lidar is a promising extension of the present method to study of aerosol and cloud effects on the earth radiation budget (Kato et al., 2011; Oikawa et al., 2013).

Our analysis is limited to only 15 cloud systems, so that a future work should be performed for more comprehensive case studies covering various clouds across the whole globe, by which I need to understand relation between the cloud parameters, such as $<\tau_c>$, $\sigma_{\tau c}$, cloud height and other statistical parameters. Especially the present cloud classification method should be validated and extended to the global cloud cases.

References

Aida, M. (1977). Scattering of solar radiation as a function of cloud dimensions and orientation. Journal of Quantitative Spectroscopy and Radiative Transfer, 17(3), 303-310. doi:10.1016/0022-4073(77)90109-1

Barker, H. W., & Davies, J. A. (1992). Solar radiative fluxes for broken cloud fields above reflecting surfaces. Journal of the Atmospheric Sciences, 49(9), 749-761. doi:10.1175/1520-0469(1992)049<0749:SRFFBC>2.0.CO;2

Barker, H. W., Jerg, M. P., Wehr, T., Kato, S., Donovan, D. P., & Hogan, R. J. (2011). A 3D cloud-construction algorithm for the EarthCARE satellite mission. Quarterly Journal of the Royal Meteorological Society, 137(657), 1042-1058. doi:10.1002/qj.824

Barker, H. W., Kato, S., & Wehr, T. (2012;2011;). Computation of solar radiative fluxes by 1D and 3D methods using cloudy atmospheres inferred from A-train satellite data. Surveys in Geophysics, 33(3), 657-676. doi:10.1007/s10712-011-9164-9

Cahalan, R. F., Gollmer, S., Wiscombe, W. J., Ridgway, W., & HARSHVARDHAN. (1994). Independent pixel and monte carlo estimates of stratocumulus albedo. Journal of the Atmospheric Sciences, 51(24), 3776-3790. doi:10.1175/1520-0469(1994)051<3776:IPAMCE>2.0.CO;2

Cahalan, R. F., Oreopoulos, L., Marshak, A., & Evans, K. F. (2005). the i3rc. Bulletin of the American Meteorological Society, 86(9), 1275.

Coakley, J. A., & Bretherton, F. P. (1982). Cloud cover from high-resolution scanner data: Detecting and allowing for partially filled fields of view. Journal of Geophysical Research,87(C7), 4917-4932. doi:10.1029/JC087iC07p04917

Davies, R. (1978). The effect of finite geometry on the three-dimensional transfer of solar irradiance in clouds. Journal of the Atmospheric Sciences, 35(9), 1712-1725. doi:10.1175/1520-0469(1978)035<1712:TEOFGO>2.0.CO;2

Evans, K. F. (1998). The spherical harmonics discrete ordinate method for three-dimensional atmospheric radiative transfer. Journal of the Atmospheric Sciences, 55(3), 429.

Gabriel, P. M., & Evans, K. F. (1996). Simple radiative transfer methods for calculating domain-averaged solar fluxes in inhomogeneous clouds. Journal of the Atmospheric Sciences, 53(6), 858-877. doi:10.1175/1520-0469(1996)053<0858:SRTMFC>2.0.CO;2

Ham, S., Kato, S., Barker, H. W., Rose, F. G., & Sun-Mack, S. (2014). Effects of 3-D clouds on atmospheric transmission of solar radiation: Cloud type dependencies inferred from A-train satellite data: Cloud-type dependent 3D effects. Journal of Geophysical Research: Atmospheres, 119(2), 943-963. doi:10.1002/2013JD020683

Illingworth, A. J., Barker, H. W., Beljaars, A., Ceccaldi, M., Chepfer, H., Clerbaux, N., . . . Zadelhoff, G. v. (2015;2014;). THE EARTHCARE SATELLITE: The next step forward in global measurements of clouds, aerosols, precipitation, and radiation. Bulletin of the American Meteorological Society, 96(8), 1311. doi:10.1175/BAMS-D-12-00227.1

INOUE, T., & ACKERMAN, S. A. (2002). Radiative effects of various cloud types as classified by the split window technique over the eastern sub-tropical pacific derived from collocated ERBE and AVHRR data. Journal of the Meteorological Society of Japan, 80(6), 1383-1394. doi:10.2151/jmsj.80.1383

Ishida, H. (2014). Application of the multigrid method in a deterministic solution scheme for the three-dimensional radiative transfer equation. Journal of Quantitative Spectroscopy and Radiative Transfer, 133, 396-411. doi:10.1016/j.jqsrt.2013.09.003

Jakub, F., & Mayer, B. (2015). 3-D radiative transfer in large-eddy simulations – experiences coupling the TenStream solver to the UCLA–LES. *Geoscientific Model Development Discussions, 8*(10), 9021-9043. doi:10.5194/gmdd-8-9021-2015

Kato, S., Rose, F. G., Sun-Mack, S., Miller, W. F., Chen, Y., Rutan, D. A., . . . Collins, W. D. (2011). Improvements of top-of-atmosphere and surface irradiance computations with CALIPSO-, CloudSat-, and MODIS-derived cloud and aerosol properties. Journal of Geophysical Research, 116(D19) doi:10.1029/2011JD016050

Kawamoto, K., Nakajima, T., & Nakajima, T. Y. (2001). A global determination of cloud microphysics with AVHRR remote sensing. Journal of Climate, 14(9), 2054.

Klinger, C., & Mayer, B. (2016). The neighboring column approximation (NCA) – A fast approach for the calculation of 3D thermal heating rates in cloud resolving

models. Journal of Quantitative Spectroscopy and Radiative Transfer, 168, 17-28. doi:10.1016/j.jqsrt.2015.08.020

Kobayashi, T. (1989). Radiative properties of finite cloud fields over a reflecting surface.Journal of the Atmospheric Sciences, 46(14), 2208-2214. doi:10.1175/1520-0469(1989)046<2208:RPOFCF>2.0.CO;2

Liou, K. (1974). Analytic two-stream and four-stream solutions for radiative transfer. Journal of the Atmospheric Sciences, 31(5), 1473-1475. doi:10.1175/1520-0469(1974)031<1473:ATSAFS>2.0.CO;2

L'Ecuyer, T. S., Wood, N. B., Haladay, T., Stephens, G. L., & Paul W. Stackhouse Jr. (2008). Impact of clouds on atmospheric heating based on the R04 CloudSat fluxes and heating rates data set. Journal of Geophysical Research - Atmospheres, 113, D00A15. doi:10.1029/2008JD009951

Marquis, J., & Harrington, J. Y. (2005). Radiative influences on drop and cloud condensation nuclei equilibrium in stratocumulus. *Journal of Geophysical Research - Atmospheres,110*(D10), D10205. doi:10.1029/2004JD005401

Marchand, R., Mace, G. G., Ackerman, T., & Stephens, G. (2008). Hydrometeor detection using cloudsat-an earth-orbiting 94-GHz cloud radar. Journal of Atmospheric and Oceanic Technology, 25(4), 519.

Marshak, A., Davis, A., Wiscombe, W., & Cahalan, R. (1995). Radiative smoothing in fractal clouds. Journal of Geophysical Research, 100(D12), 26247. doi:10.1029/95JD02895

Marshak, A., Davis, A., Wiscombe, W., Ridgway, W., & Cahalan, R. (1998). Biases in shortwave column absorption in the presence of fractal clouds. Journal of Climate, 11(3), 431-446. doi:10.1175/1520-0442(1998)011<0431:BISCAI>2.0.CO;2

Marshak, A., & Davis, A. (2005). 3D radiative transfer in cloudy atmospheres. Berlin: Springer.

Marshak, A., Platnick, S., Várnai, T., Wen, G., & Cahalan, R. F. (2006). Impact of three-dimensional radiative effects on satellite retrievals of cloud droplet sizes. Journal of Geophysical Research - Atmospheres, 111(D9), D09207. doi:10.1029/2005JD006686

Matsumoto, M., & Nishimura, T. (1998). Mersenne twister: A 623-dimensionally equidistributed uniform pseudo-random number generator. *ACM Transactions on Modeling and Computer Simulation (TOMACS), 8*(1), 3-30. doi:10.1145/272991.272995

McKee, T. B., & Cox, S. K. (1974). Scattering of visible radiation by finite clouds. Journal of the Atmospheric Sciences, 31(7), 1885-1892. doi:10.1175/1520-0469(1974)031<1885:SOVRBF>2.0.CO;2

Meador, W. E., & Weaver, W. R. (1980). Two-stream approximations to radiative transfer in planetary atmospheres: A unified description of existing methods and a new improvement.Journal of the Atmospheric Sciences, 37(3), 630-643. doi:10.1175/1520-0469(1980)037<0630:TSATRT>2.0.CO;2

Nakajima, T., & Tanaka, M. (1983). Effect of wind-generated waves on the transfer of solar radiation in the atmosphere-ocean system. Journal of Quantitative Spectroscopy and Radiative Transfer, 29(6), 521-537. doi:10.1016/0022-4073(83)90129-2

Nakajima, T., & Tanaka, M. (1986). Matrix formulations for the transfer of solar radiation in a plane-parallel scattering atmosphere. Journal of Quantitative Spectroscopy and Radiative Transfer, 35(1), 13-21. doi:10.1016/0022-4073(86)90088-9

Nakajima, T., & Tanaka, M. (1988). Algorithms for radiative intensity calculations in moderately thick atmospheres using a truncation approximation. Journal of Quantitative Spectroscopy and Radiative Transfer, 40(1), 51-69. doi:10.1016/0022-4073(88)90031-3

Nakajima, T., Tsukamoto, M., Tsushima, Y., Numaguti, A., & Kimura, T. (2000). Modeling of the radiative process in an atmospheric general circulation model. Applied Optics, 39(27), 4869. doi:10.1364/AO.39.004869

Nakajima, T., & King, M. D. (1990). Determination of the optical thickness and effective particle radius of clouds from reflected solar radiation measurements. part I: Theory. Journal of the Atmospheric Sciences, 47(15), 1878-1893. doi:10.1175/1520-0469(1990)047<1878:DOTOTA>2.0.CO;2

Nakajima, T. Y., & Nakajima, T. (1995). Wide-area determination of cloud microphysical properties from NOAA AVHRR measurements of FIRE and ASTEX regions. Journal of the Atmospheric Sciences, 52(23), 4043.

Oikawa, E., Nakajima, T., Inoue, T., & Winker, D. (2013). A study of the shortwave direct aerosol forcing using ESSP/CALIPSO observation and GCM simulation: DARF USING CALIPSO AND GCM. Journal of Geophysical Research: Atmospheres, 118(9), 3687-3708. doi:10.1002/jgrd.50227

Oinas, V., & Lacis, A. A. (1991). A description of the correlated k distributed method for modeling nongray gaseous absorption, thermal emission, and multiple scattering in vertically inhomogeneous atmospheres., 9027.

Petty, Grant W. (Grant William), 1958. (2006). *A first course in atmospheric radiation* (2nd ed.). Madison, Wis: Sundog Pub.

Rothman, L. S., Jacquemart, D., Barbe, A., Chris Benner, D., Birk, M., Brown, L. R., . . . Wagner, G. (2005). The HITRAN 2004 molecular spectroscopic database. *Journal of Quantitative Spectroscopy and Radiative Transfer, 96*(2), 139-204. doi:10.1016/j.jqsrt.2004.10.008

Sekiguchi, M., & Nakajima, T. (2008). A k-distribution-based radiation code and its computational optimization for an atmospheric general circulation model. Journal of Quantitative Spectroscopy and Radiative Transfer, 109(17), 2779-2793. doi:10.1016/j.jqsrt.2008.07.013

Smith, P. L. (1984). Equivalent radar reflectivity factors for snow and ice particles. Journal of Climate and Applied Meteorology, 23(8), 1258-1260. doi:10.1175/1520-0450(1984)023<1258:ERRFFS>2.0.CO;2

Stamnes, K., Tsay, S. C., Wiscombe, W., & Jayaweera, K. (1988). Numerically stable algorithm for discrete-ordinate-method radiative transfer in multiple scattering and emitting layered media. *Applied Optics, 27*(12), 2502.

Stephens, G. L. (1988). Radiative transfer through arbitrarily shaped optical media. part II. group theory and simple closures. Journal of the Atmospheric Sciences, 45(12), 1837-1849. doi:10.1175/1520-0469(1988)045<1837:RTTASO>2.0.CO;2

STEPHENS, G., TSAY, S., STACKHOUSE, P., & FLATAU, P. (1990). the relevance of the microphysical and radiative properties of cirrus clouds to climate and climatic feedback.*Journal of the Atmospheric Sciences, 47*(14), 1742-1753.

Stephens, G., Gabriel, P., & Tsay, S. (1991). Statistical radiative transport in one-dimensional media and its application to the terrestrial atmosphere. Transport Theory and Statistical Physics, 20(2), 139-175.

Su, W., Corbett, J., Eitzen, Z., & Liang, L. (2015). Next-generation angular distribution models for top-of-atmosphere radiative flux calculation from CERES instruments: Validation.*Atmospheric Measurement Techniques, 8*(8), 3297-3313. doi:10.5194/amt-8-3297-2015

Varnai, T., & Davies, R. (1999). Effects of cloud heterogeneities on shortwave radiation: Comparison of cloud-top variability and internal heterogeneity. Journal of the Atmospheric Sciences, 56(24), 4206.

Varnai, T., & Marshak, A. (2002). Observations of three-dimensional radiative effects that influence MODIS cloud optical thickness retrievals. Journal of the Atmospheric Sciences,59(9), 1607.

Wielicki, B. A., & Welch, R. M. (1985). A radiative parameterization of stratocumulus cloud fields. Journal of the Atmospheric Sciences, 42(24), 2888-2897. doi:10.1175/1520-0469(1985)042<2888:ARPOSC>2.0.CO;2

Wissmeier, U., Buras, R., & Mayer, B. (2013). paNTICA: A fast 3D radiative transfer scheme to calculate surface solar irradiance for NWP and LES models. Journal of Applied Meteorology and Climatology, 52(8), 1698.

Zhang, Z., & Platnick, S. (2011). An assessment of differences between cloud effective particle radius retrievals for marine water clouds from three MODIS spectral bands. Journal of Geophysical Research, 116(D20) doi:10.1029/2011JD016216

Zuidema, P., & Evans, K. F. (1998). On the validity of the independent pixel approximation for boundary layer clouds observed during ASTEX. Journal of Geophysical Research: Atmospheres, 103(D6), 6059-6074. doi:10.1029/98JD00080